The Hashemite Kingdom of Jordan
Scientific Research Support Fund
The Hashemite University

JJEES

Jordan Journal of Earth and Environmental Sciences

Volume (11) Number (1)

Cover photo © Yarmouk University Applied Geoinformatics Research Group

JJEES is an International Peer-Reviewed Research Journal

ISSN 1995-6681 jjees.hu.edu.jo March 2020

Jordan Journal of Earth and Environmental Sciences (JJEES)

JJEES is an International Peer-Reviewed Research Journal, Issued by Deanship of Scientific Research, The Hashemite University, in corporation with, the Jordanian Scientific Research Support Fund, the Ministry of Higher Education and Scientific Research.

Submission address:

Manuscripts should be submitted electronically to the following e-mail:

jjees@hu.edu.jo

For more information and previous issues:

www.jjees.hu.edu.jo

Hashemite Kingdom of Jordan

Scientific Research Support Fund

Hashemite University

Jordan Journal of Earth and Environmental Sciences

JJEES

An International Peer-Reviewed Scientific Journal

Financed by the Scientific Research Support Fund

Volume 11 Number (1)

http:// jjees.hu.edu.jo/

ISSN 1995-6681

Cover page photo: "The Umm Ishrin Sandstone Formation in Petra taken by Low Altitude Unmanned Aerial Vehicle (UAV)"
Photo by Yarmouk University Applied Geoinformatics Research Group

JJEES
Jordan Journal of Earth and Environmental Sciences

JJEES

JJEES (2020) 11 (1): 1-11
ISSN 1995-6681

Jordan Journal of Earth and Environmental Sciences

Soft-Sediment Deformation in the Campanian-Maastrichtian Deltaic Deposits of the Afikpo Sub-basin, South-eastern Nigeria: Recognition of Endogenic Trigger

Ogechi Ekwenye*, Ayonma Mode, Ifeanyi Oha, Fidelis Onah

University of Nigeria, Department of Geology, Nigeria

Received 13th June 2019, Accepted 15 August 2019

Abstract

In this research, soft-sediment deformation structures are studied and analyzed from the Cretaceous deltaic deposits of the Afikpo Sandstone Member of the Nkporo Formation in Afikpo Sub-basin. These deformation structures are grouped into three morphological and deformational styles which include load structures (load casts, ball-and pillow-structures, flame structures, and pseudonodules), ductile disturbed structures (loop bedding, recumbent folding, and deformed lamination), and brittle deformation (synsedimentary fractures). The facies analysis revealed sedimentary structures that are indicative of storm and wave processes and rapid sedimentation. Though the trace fossils have a low to moderate diversity and abundance, the *Skolithos* ichnofacies, particularly the *Diplocraterion* and *Skolithos* burrows, are relatively frequent. These ichnofossils are indicative of high-energy conditions and rapid sedimentation. The recognition of the deformation processes and their triggers suggests that the soft sediment deformation structures in the study area are not tectonic in origin as they are associated with storm-generated sedimentary structures and structures formed due to rapid sedimentation. Furthermore, the deformational structures are restricted to a single stratigraphic layer, and are not laterally extensive suggesting an endogenic or non-seismic trigger mechanisms such as storm events, overloading, and rapid sedimentation.

Keywords: Cretaceous deltaic deposit, soft sediment deformation, deformation processes, non-seismic trigger.

1. Introduction

Soft sediment deformation structures (SSDS) occur in unconsolidated water-saturated sediments during or shortly after deposition, and before significant diagenesis (Owen et al., 2011). Interest in the study of soft sediment deformation structures and their triggering mechanisms have progressively developed considerably over the past decades (Kuenen, 1958; Sanders, 1960; Dott and Howard, 1962; Lowe, 1975; Allen, 1982; Mills, 1983; Owen, 1987; Moretti, 2000; Rodríguez-Pascua et al., 2000; van Loon, 2009; Oliveira et al., 2011; Owen and Moretti, 2011; Owen et al., 2011; Sarkar, et al., 2014; Shanmugam, 2017). Many authors have associated soft-sediment deformation structures with seismically-induced triggering mechanisms (Mohindra and Bagati 1996; Moretti, 2000; Rodríguez-Pascua et al., 2000; Ettensohn et al., 2002; Samaila et al., 2006; Bhattacharya and Bhattacharya, 2010; Martín-Chivelet et al., 2011; Lunina and Gladkov, 2016), whereas limited works refer such deformational structures to non-seismically-induced triggering mechanisms such as storms, waves, tidal surge, floods, overloading, rapid sedimentation, and groundwater movements (Allen, 1982; Owen, 1987; Kerr and Eyles 1991; Molina et al., 1998; Alfaro et al., 2002; Owen and Moretti, 2011; Põldsaar and Ainsaar, 2014). Furthermore, some soft-sediment deformation structures, such as loop bedding, seem to be specifically related with seismic trigger mechanisms (Calvo et al., 1998; Rodríguez-Pascua et al., 2000; Martín-Chivelet et al., 2011).

Detailed description and interpretation of the soft-sediment deformation structures (SSDS) in the Afikpo Sandstone Member, particularly in the Itigidi region, is not yet reported in any published work. This paper records for the first time the genesis and implication of soft-sediment deformation in the Afikpo Sub-basin. Published reports of detailed soft-sediment deformation structures in Nigerian sedimentary basins are mostly limited to the Bima Formation of the Northern Benue Trough (Jones, 1962; Benkhelil, 1980, 1989; Braide, 1992; Guirand and Plaziat, 1993; Samaila et al., 2006), the Ajali Formation of the Anambra Basin (Ladipo, 1988; Obi and Okogbue, 2004; Olabode, 2014), the Central and the Southern Benue Trough (Hoque, 1984; Benkhelil, 1986, 1987; Dim et al., 2016). Detailed facies analysis and ichnology of the Campanian-Maastrichtian deposits of the Afikpo Sandstone Member in the Itigidi region is discussed in Mode et al. (2018). This research concentrates on the recognition of the soft-sediment deformation structures (SSDS) in the Itigidi area.

In this study, sedimentology and a detailed description of the SSDS help establish some genetic relationships between ordinary sedimentary processes (endogenic triggering mechanisms) and the occurrence of deformed beds. Furthermore, from a regional point of view, this study describes and interprets the occurrence of soft-sediment deformation structures in the Afikpo Sandstone deposits of the Afikpo Sub-basin.

* Corresponding author e-mail: ogechi.ekwenye@unn.edu.ng

2. Geological Setting

The Afikpo sub-basin commonly referred to as Afikpo Syncline is located in south-eastern Nigeria, and its origin is linked to the formation of the Benue Trough. The Benue Trough originated from the break-up of the Gondwana supercontinent which resulted in the separation of the African plate and South-American plate during the Late Cretaceous (Reyment, 1965; Murat, 1972; Nwachukwu, 1972; Olade, 1975; Kogbe, 1976; Petters, 1978; Wright, 1981; Benkhelil, 1982, 1989; Hoque and Nwajide, 1984; Maurin et al., 1986). The trough is part of a large West and Central African Rift System (WCARS) (Genik, 1992) which resulted from the crustal stretching of the African plate consequent upon the break-up of the Afro-American plate (Figure 1). The rift structure is generated by sinistral displacements along a pre-existing zone of northeast-southwest trending transcurrent fault (Benkhelil, 1982, 1989; Maurin et al., 1986; Popoff et al., 1986). The Benue Trough occurred as an elongate intracratonic structure over 1,000 km long and up to 250 km at its widest part. Olade (1979); Popoff et al., (1982); Benkhelil (1989) suggested a magmatic activity during the opening and filling of the Benue Trough which led to the deposition of the Abakaliki pyroclastics. However, Hoque (1984) argued that the pyroclastics are post-Santonian in age. Sedimentation in the Southern Benue Trough (Abakaliki Basin) commenced in the Aptian-Albian times, and was halted due to the Santonian thermo-tectonism (Figure 2). This Santonian compressional phase resulted in the folding, faulting and uplifting of the Abakaliki Basin to form an anticlinorium; displacing depocentres westward and eastward to form the Anambra Basin and Afikpo Sub-basin (Simpson, 1954; Benkhelil, 1986, 1989; Okoro et al., 2012a). Sedimentation commenced in the Afikpo Sub-basin during the Campanian to Early Maastrichtian with the Nkporo Shale and Afikpo Sandstone Members (Simpson, 1954; Reyment, 1965) which formed the Nkporo Formation; this is followed by the Maastrichtian Coal Measures which include the Mamu, Ajali, and Nsukka formations, with the Nsukka Formation terminating sedimentation in the basin (Nwajide, 2005).

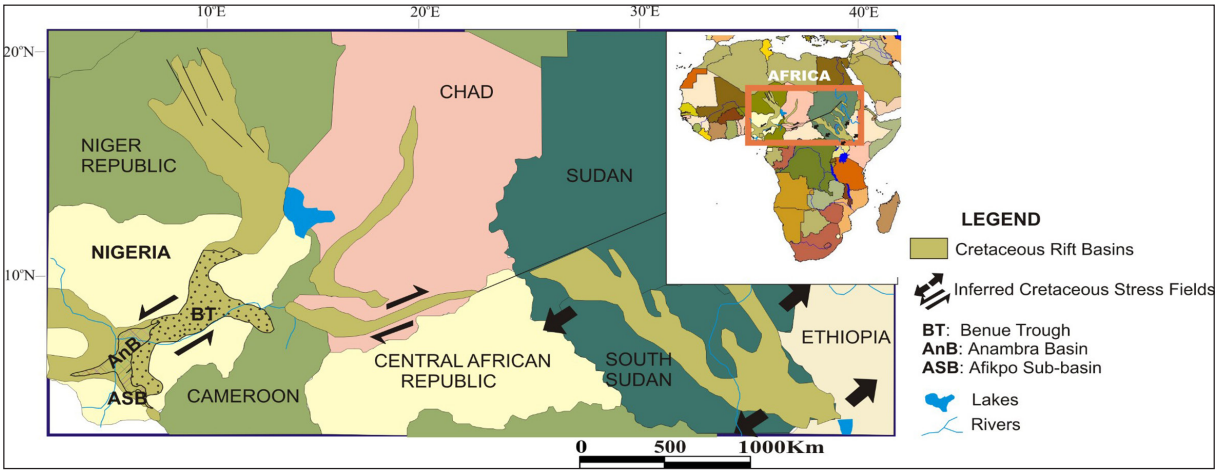

Figure 1. Tectonic map of the West and Central African Rift Systems (WCARS), showing the Benue Trough, the Anambra Basin, and the Afikpo Sub-basin (modified after Oha et al., 2016; Mode et al., 2018).

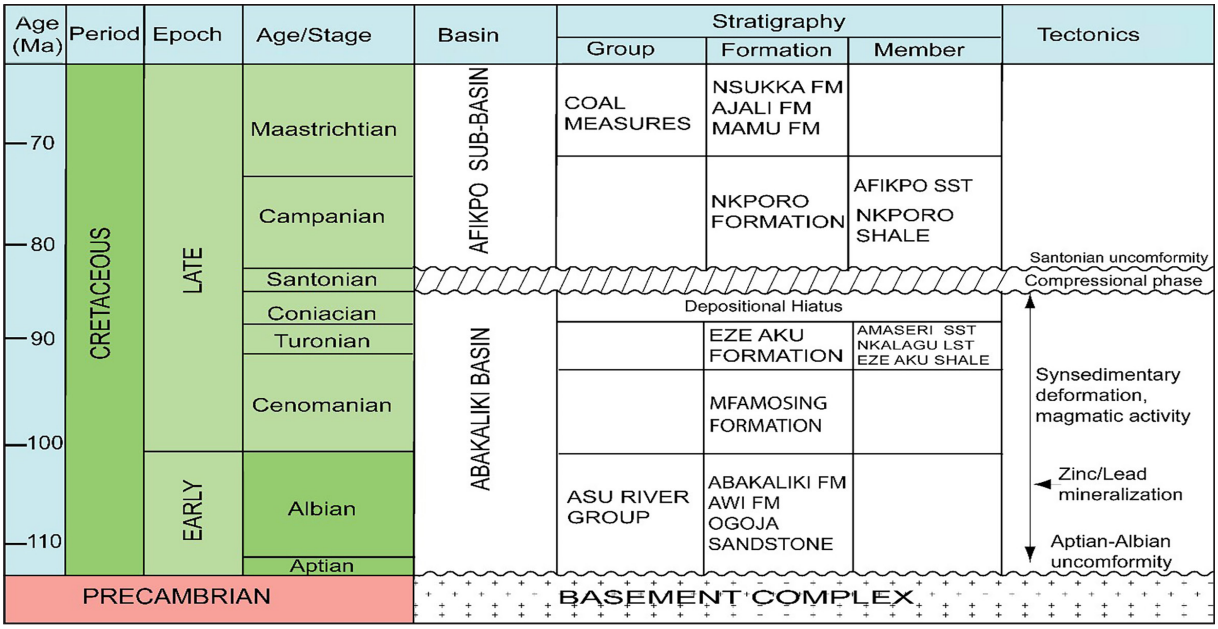

Figure 2. Tectonostratigraphy of the Abakiliki-Benue Trough and the Afikpo Sub-basin (Modified and redrawn from Okoro et al., 2012a; Nwajide, 2013; Ekwenye et al., 2015).

Note: SST stands for Sandstone; FM stands for Formation

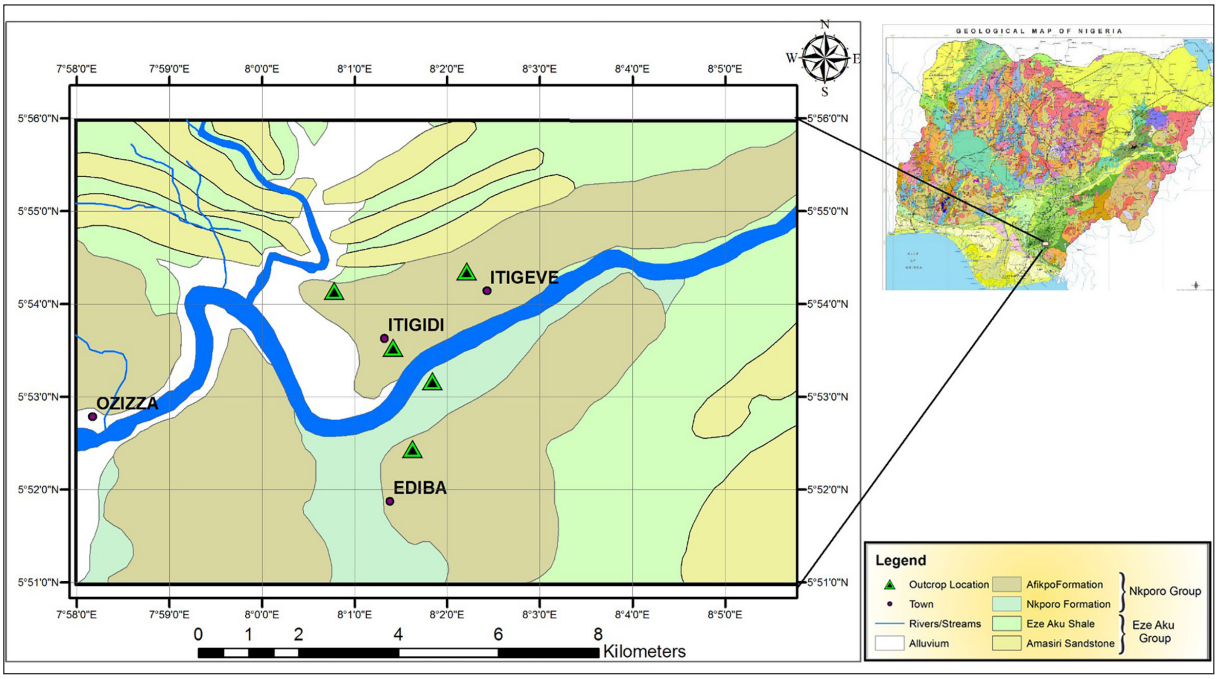

Figure 3. Geologic map of study area showing the major outcrop locations within Itigidi and environs.

3. Sedimentology

Several works have been carried out to investigate the depositional environments of the Nkporo Formation in the Afikpo Sub-basin, most of the studies are done on a regional scale (Simpson, 1954; Reyment, 1965; Banerjee, 1981; Benkhelil, 1986; Mode, 1991; Petters and Edet, 1996; Odigi, 2011; Okoro et al., 2012a, b), and there are limited data on the Itigidi-Ediba regions (Benkhelil, 1986; Mode et al., 2018). The study area is underlain by the Afikpo Sandstone Member of the Nkporo Formation (Figure 3). Mode et al., 2018 described the sedimentary units in the Itigidi region and grouped them into six facies associations (FA 1–6) depicting a prograding deltaic strata deposited on the shelf, prodelta, distal delta front, proximal delta front, distributary mouth bar, and bay-fill sub-environments. Abridged sedimentology of the study area is integrated with the SSDS to suite the purpose of this study.

The basal unit of the study area is a well-exposed fossiliferous shale and well-sorted fine to very fine grained sandstone with micro-hummocky cross-stratification (which has an average length of 5 cm and width of 2 cm), interpreted as shelf (FA 1) and the prodelta (FA 2) deposits (Mode et al., 2018) record no soft sediment deformation structures (Figures 4). Sets of coarsening-upward beds of structureless sandstone, siltstone, sandy heterolithic, current rippled laminated sandstone, thin muddy heterolithic, and bioturbated sandstone units, considered as distal delta front, and also known as distal bar (FA 3) (Mode et al., 2018), exhibit a number soft-sediment defomation structures. Load cast, ball-and-pillow structures, flame-like structures, pseudonodules were observed within the sandy heterolithic facies and sandstones which are underlain by muddy heterolithic facies and carbonaceous mudstone. Loop bedding occurs within the muddy heterolithic unit. Suite of trace fossils found within sandy units includes *Palaeophycus*, *Diplocraterion, Skolithos* and *Teichichnus*. The bioturbated sandstone facies which tops the distal prodeltaic deposits is intensely bioturbated consisting of *Skolithos, Cruziana,* and *Zoophycus* ichnofacies.

A coarsening upward succession of sandy and muddy heteroliths, followed by stacks of cross-bedded and horizontally-bedded coarsening upward sandstone and hummocky cross-stratified sandstone, dominates the proximal delta front (FA 4). FA 4 exhibits relatively fewer soft sediment deformation structures such as load casts and flame structures which occur locally within the sandy heterolithic and muddy heterolithic units. The load casts show low-diversity ichnofossils consisting of *Skolithos, Trichichnus* burrows.

The bioturbation intensity is low to moderate. Cruziana and Skolithos ichnofacies such as *Diplocraterion, Macaronichnus, Chondrites, Planolites, Rosselia, Conichnus, Skolithos? Cylindrichichnus* and *Trichichnus* were observed within the hummocky cross-stratified sandstone. *Diplocraterion parallelum* and *Conichnus* burrows are dominant at the basal part of the current rippled laminated sandstone facies.

The study are is capped by hummocky cross-bedded sandstone at the base; overlain by parallel to low-angle laminated sandstone and swaley cross-bedded sandstone facies referred to as a distributary mouth-bar deposits (FA 5). Here, the soft-sediment deformation structures, such as the load casts, ball and pillow structures, pseudonodules, flame structures, and recumbent fold, occur within the sandy mouth-bar deposits on top and the muddy heterolithic interpreted as bay-fill deposits at the base (FA 6). The degree of bioturbation is low within the mouth-bar and bay-fill deposits. *Diplocraterion, Skolithos, Conichnus* ichnofossils are common within the mouth-bar deposits.

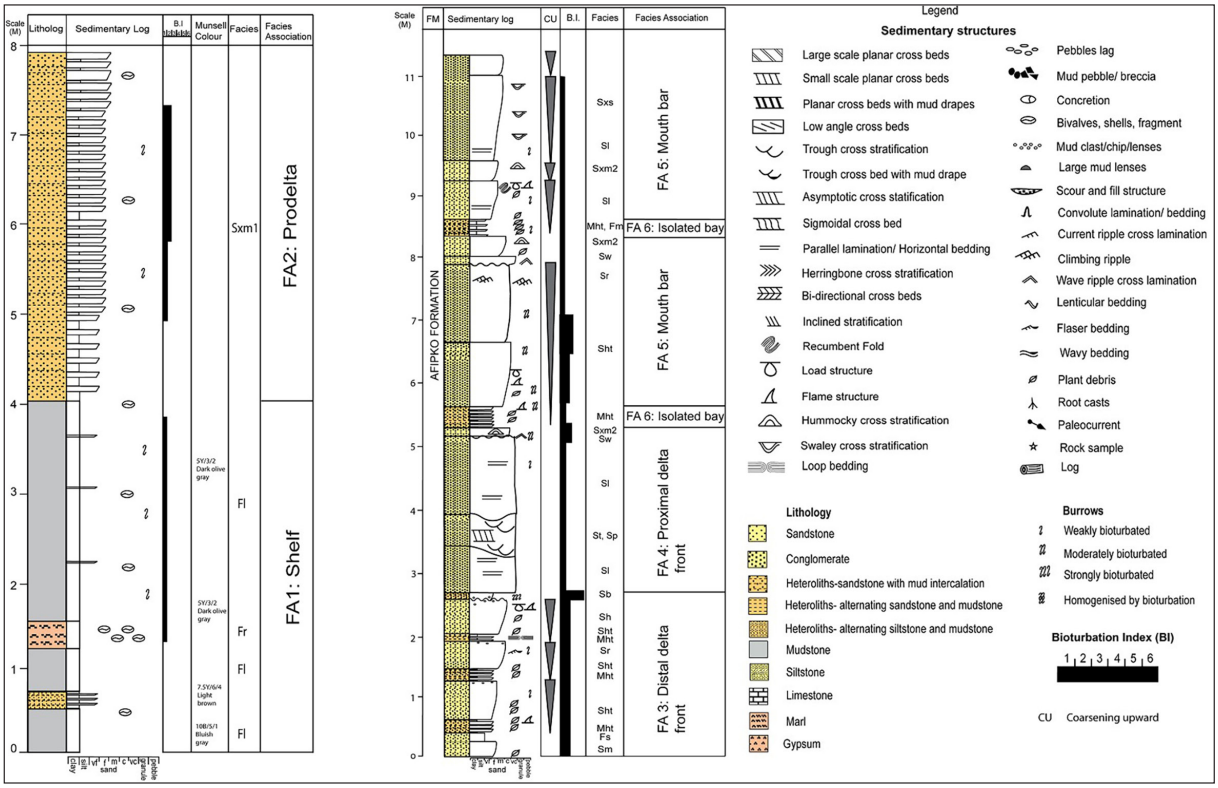

Figure 4. Representative lithostratigraphic log profiles of Ediba (a) and Itigidi (b) areas.

4. Results and Interpretation

4.1 Soft-Sediment Deformation Structure: Classification and Driving Forces

The soft-sediment deformation structures observed in the study area are dominant in the delta front, mouth-bar and bay-fill deposits. The deformation structures are contemporaneous with deposition or post-deposition, and they are common in medium to fine-grained sandstone, siltstone, heterolithic deposits, and carbonaceous mudstone in the study area. However, syndepositional fractures occur in coarse-grained sandstone. The deformational structures, especially the load structures, are commonly observed in the proximal and distal delta front deposits, where more competent materials (sandstone, sandy heterolithic sediment) overlie less competent materials (mudstone/shale, siltstone or muddy heterolithic sediment). These deformational structures are less common in sandy areas or units with less muddy sediments.

The soft-sediment deformation structures in the study area are classified into three groups based on morphological and deformational styles (Lowe, 1975; Mills, 1983; Owen, 1987, 2003; Moretti, 2000; Alfaro et al., 2002; Owen et al., 2011) as follows: 1) load structures which include load casts, pseudonodules, ball-and-pillow structures and flame structures 2) ductile disturbed structures such as recumbent folds, loop beddings, and deformed lamination, 3) brittle deformed structures which consist of syndepositional fractures. These morphological trends depend on the driving forces which acted on the sediments during deformation. The major driving forces that initiated these deformations include gravitational instability and shear stress by current (Figure 5).

Load Structures

The load structures encountered in the study area include load casts, ball-and-pillow structures, flame structures and pseudonodules (Figures 5 and 6). Most of the load structures occurred within the same horizon, and they are mostly formed by gravitational (vertical) forces associated with reversed density mechanism (Owen et al., 2011), or reduction in shear stress as in the case of flame structures (Mills, 1983). Some of the load structures are associated with or occur as deformed parts of climbing ripples, wave ripples, and hummocky cross-stratification.

Load casts are the commonest load structures and soft-deformation structures in the study area. Their maximum size is about 1.3–1.5 m in width and 50–80 cm in height, and they occurred in the medium to fine-grained sandstone and sandy heterolithic deposits (Figure 6a). Their internal structures are well-preserved. The load casts are large, undulating, with a bulbous protrusion; they slightly sink into the underlying muddy substrate, showing a concave profile (Figures 6a, c-e). Some load casts occur at the bottom of larger pillows (Figure 6e). The load casts are associated with water-escape structures formed between adjacent the load casts (see Figures 6c, f). The characteristics of these large-scale load casts are similar to those described by Alfaro et al. (2002) and Moretti and Sabato (2007).

Driving force: Load casts are characterized by the deposition of competent (denser) sandy sediment over less competent (less dense) muddy substrate, which results in gravitational instabilities due to a reversed density gradient (Mills, 1983; Moretti and Sabato, 2007; Owen et al., 2011). Reversed density deformation may also be produced by rapid deposition of weakly compacted mud, overlain by rapidly deposited medium-grained sands.

Soft sediment deformation structures	Driving Force	Depositional mechanism	Trigger mechanism
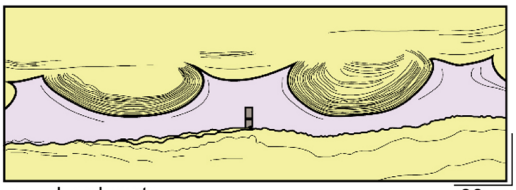 a. Load casts	Gravitational instability due to reversed density gradient	Liquefaction and fluidization	Rapid sedimentation
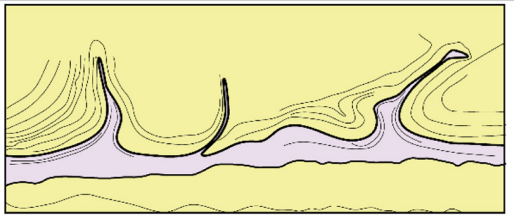 b. Flame structures	Vertical shear stress due to gravitational readjustment	Liquefaction and fluidization	Rapid sedimentation and storm
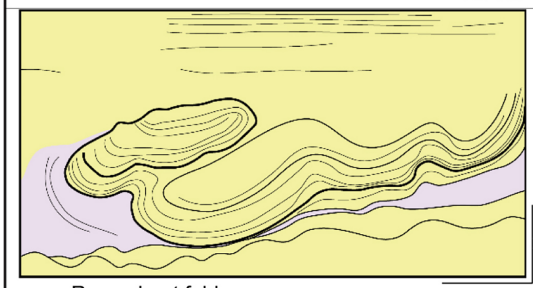 c. Recumbent folds	Current shear or lateral drag of flowing fluid	Liquefaction	Rapid sedimentation and storm
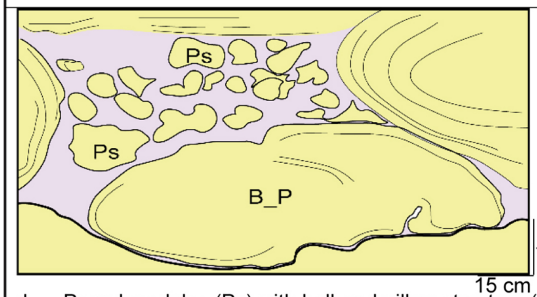 d. Pseudonodules (Ps) with ball-and-pillow structure (B_P)	Gravitational instability due to reversed density loading	Liquefaction	Rapid sedimentation and storm
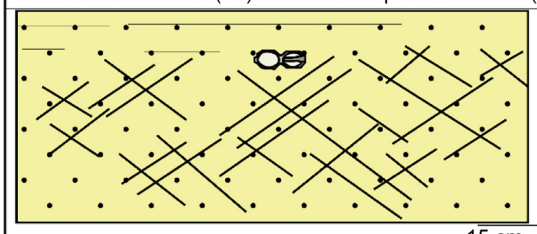 e. Syndepositional joints	Increase in pore pressure in cohesive material results to tensional stress	Liquefaction and intergranular shear	Rapid sedimentation or storm
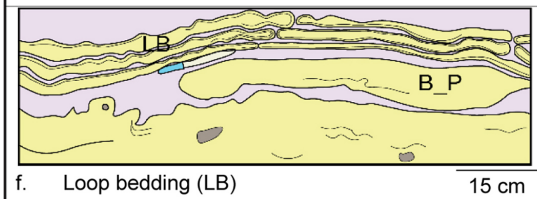 f. Loop bedding (LB)	Increase pore pressure results to tensional stress	Liquefaction and intergranular shear	Rapid sedimentation

Figure 5. A catalogue of the soft sediment deformation structures encountered in Itigidi, their driving forces, deformation mechanism and triggers.

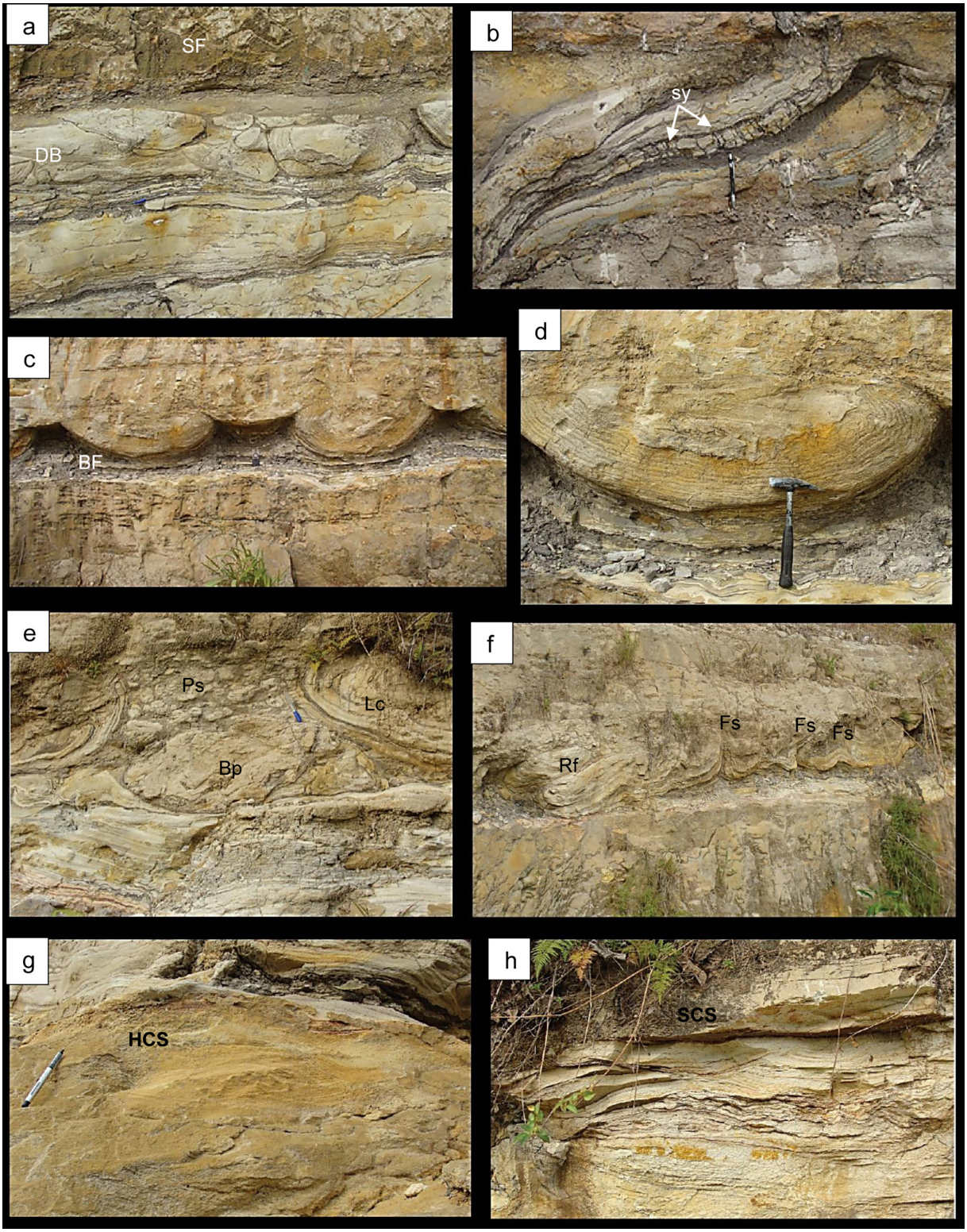

Figure 6. Occurrences and types of soft sediment deformation structures in the prograding deltaic deposits. **(a).** Large- and small-sized ball and pillow structures at the sandy heterolith of the distal delta front or distal bar (DB) whereas loop bedding is observed within the muddy heterolithic deposit. Syndepositional fractures (SF) occur in the horizontally bedded sandstone facies of the proximal delta front. **(b).** The flame-like structure shows syneresis cracks which may indicate changes in salinity. **(c).** Typical load cast structures with bulbous protuberances and water escape structures with upward directed crests formed within the bay-fill (BF) (muddy interval) and proximal delta front (sandy bed) deposits. **(d).** A close-up of the isolated load cast with deformed internal laminae forming a crescent shape that aligned with the morphology of the load cast. The interval is poorly burrowed, exhibiting low diversity, diminutive *Skolithos, Trichichnus* and *Planolites* ichnofossils. **(e).** Load structures consisting of load casts (Lc), ball and pillow structure (Bp) and pseudonodules (Ps) occurred within a mouth bar deposit. **(f).** Recumbent folds (Rf) in association with flame structures (Fs) are observed within the mouth bar deposit. The deformation displaced the muddy sediments of the bay-fill vertically or laterally. **(g).** Hummocky cross-stratified sandstone (HSC). **(h).** Swaley cross-stratified sandstone (SCS).

Flame structures commonly occur with load casts as upward-directed crests or tongue-like hydroplastic intrusions (Bhattacharya and Bhattacharya, 2010) of underlying muddy sediments into the load casts (Figures 6b-c, f). They are commonly referred to as water (fluid)-escape structures (Lowe, 1975; Alfaro et al., 2002). Flame structures are also formed in sandy units; they form large-scale isolated sandy flame-like structures with syneresis cracks as shown in figure 6b. Some poorly-developed flame structures are observed as convex-upward shaped flat crests (see Figure 6f). The flame structures consist of carbonaceous shale and alternating carbonaceous shale and siltstone. Internal lamination is observed in the muddy heterolithic layer. The well-developed flame structures are represented by vertical conduit, adapting to the external contour of the load casts (Alfaro et al., 2002). The flame structures have a maximum height of 80 cm and a width of 60 cm. They are similar to those described by Alfaro et al. (2002); Collinson et al. (2006).

Driving force: Flame structures are commonly associated with load casts. The reversed density loading which acts on a competent sediment creates a downward vertical force that controlled the formation of the load casts and simultaneously, an upward flow structure is formed by reduction in shear stress as the less competent substrate intrudes into the overlying layer (Mills, 1983; Oliveira et al., 2011) due to gravitational readjustment (Alfaro et al., 2002). Bhattacharya and Bhattacharya, 2010 suggested that the inclined nature of the flames (as observed in figure 6f), may indicate deposition along a gentle slope and/or subsequent modification of the flame structures by current (Brodzikowski and Haluszczak, 1987). The isolated sandy flame-like structure is formed from vertical displacement; the deformation is localized, and may have resulted from vertical shear (Owen, 1995).

Ball-and-pillow structures are very common in the study area, and are dominated by large-scale, isolated sandy structures with relatively undisturbed flat-tops and bulbous bases as described by Mills (1983). Small-scale ball-and-pillow structures are also observed (Figure 6a). The large-scale pillows have maximum width and height of about 80 and 40 cm, respectively, while the small-scale pillows have maximum width and height of about 30 and 16 cm, respectively. The pillows are embedded in silty sands, but are notably underlain by thin silty sands, unlike the pseudonodules. Most of the pillows have well-preserved internal structures and the laminations may be parallel, curved to concentric resembling the shape of pillows.

Driving force: Ball-and-pillow structures similar to other load structures resulted from the formation of reverse density mechanisms. Though, they are thought to be genetically different from pseudonodules and other load structures (Mills, 1983). Ball-and-pillow structures are distinguished from pseudonodules by the minor amount of finer sediments required in their formation (Blatt et al., 1980).

Pseudonodules are observed within the same bed layer with the other load structures. They occur as isolated masses of irregularly-shaped and fine-grained sand, embedded in an underlying deposit of contrasting density (Kuenen, 1958; Allen, 1982), which is of the finer matrix such as mudstone or siltstone (Figures 6k,l). Some of the sand nodules retain lamination; concentric and deformed laminations are observed. They are mostly small, but vary in sizes from 1–8 cm in height and 2–10 cm in width. (Mills, 1983).

Driving force: The formation of pseudonodules is similar to that of the loaded cast, but an advanced stage of it (Topal and Özkul, 2014). Here, the underlying fine- grained sediment is more viscous (Mills, 1983) or water-saturated (Kuenen, 1958) than that of the load cast. A reversed density loading is also postulated for the formation of pseudonodules (Blatt et al., 1980; Mills, 1983).

Ductile Disturbed Structures

Loop beddings are deformational structures characterized by bundles of laminae that are sharply constricted at intervals having shapes like loops or links of a chain (Cole and Picard, 1975; Gibling et al., 1985; Calvo et al., 1998). The loop bedding structure is commonly observed in finely-laminated sediments (Cole and Picard, 1975; Gibling et al., 1985; Trewin, 1986) and laminites (which consist of packages of diatomite laminae; see Rodríguez-Pascua et al., 2000) of lacustrine depositional environments, as well as carbonate microbialites (Martín-Chivelet et al., 2011).

In the study area, the loop bedding is observed in the muddy heterolithic units consisting of carbonaceous shale, siltstone, and a very fine-grained sandstone. This loop bedding is fairly exposed in about a 20 cm thick heterolithic unit (Figures 4, 5f); the length of the loops varies from 20 cm to 35 cm, and the thickness of the loop-bedded layer is about 5 mm thick. The loop bedding exhibits a boudinage-like morphology (which Martin-Chivelet et al., 2011 referred to as boudinage structures) and is not associated with any joints, faults, or microfaults.

Driving force: The loop bedding is formed as a result of ductile deformation (Rodríguez-Pascua et al., 2000) or reflects a plastic or hydroplastic deformation of partially lithified sediments (Martín-Chivelet et al., 2011). The loop bedding may be formed as a result of the stretching of unlithified or laminae bundles with low contrast incompetence, which is said to occur in response to seismic shocks due to the slow movement of extensional faults (Calvo et al., 1998; Rodríguez-Pascua et al., 2000; Martín-Chivelet et al., 2011). It can also occur because of the increase in the pore pressure of the unlithified sandy layers resulting in tension stress.

Recumbent folds occur in association with pseudonodules, load casts, and flame structures (Figure 6f). The folded sediments are developed in laminated sandy heterolithic units, and are characterized by isoclinal limbs and multiple circular hinges in a nearly horizontal axial state, exhibiting an antiformal and synformal geometries. The folds are not associated with faults or micro-faults. The height of the recumbent folds is between 30–60 cm thick, and the width is about 25 cm thick.

Driving force: Recumbent folds may be formed as a result of current (tangential) shear in semi-consolidated or liquefied sediments (Mills, 1983; Owen, 1996) or because of the lateral drag of a flowing sediment-rich fluid mass over water-saturated sands (McKee et al., 1962). The presence of

alternating antiformal and synformal shapes, according to Owen (1995) suggests an interaction between a convection pattern of pore-water movement and upward movement of pore water that liquidized the bed.

Deformed laminations as explained by Moretti and Sabato (2007) include those deformed structures that are not categorized as load structures, loop beddings, recumbent folds, or brittle deformed structures in the study area. These structures are common in the sandy heterolithic units and exhibit varying morphologies. The deformed features may be folded, crumped, or stretched sediments. They occur in association with other soft-sediment deformation structures, either at the base or top of the bed unit.

Driving force: the deformed lamination may have been formed as a result of the current drag on partially-liquefied sand (Bhattacharya and Bhattacharya, 2010).

Brittle Deformed Structures

Syndepositional fractures occur at the lower and upper part of the very coarse to coarse-grained trough cross-stratified and massive sandstones. The highly dipping (>80°) joint sets display cross-cutting relationship; the major joints trend in a northwest direction (averaging 350°), whereas the minor joints indicate a westward direction (averaging 270°). No displacement is observed in the fractures (see Figures 5, 6a).

Driving force: Syndepositional fractures are the only soft-sediment deformation observed in the coarse-grained sandstone. No syndepositional faults, microfaults, or folds were observed. The cohesionless sandstone unit experienced only brittle deformation which suggests that the sediment was unsaturated with water during deformation (Mohindra and Bagati, 1996; Moretti, 2000). Brittle deformation arises from the cohesive behaviour of the sandstone when an increase in pore pressure is not strong enough to liquefy the sediment (Vanneste et al., 1999).

5. Discussion

5.1 Soft-Sediment Deformation Processes

A number of depositional environments such as shoreline, fluvial as well as the deep marine settings are commonly associated with soft-sediment deformation structures because of the slope gradient, high fluid discharge and rapid sedimentation (Pulham, 1989, Bhattacharya and Walker, 1991; Coleman, et al., 1983; Martinsen, 1989; Moretti et al., 2001; Oliveira et al., 2011). Figure 7 is a conceptual model (cross-section) showing the occurrence and distribution of soft-sediment deformation structures in a deltaic body (Nichols, 2009).

Soft-sediment deformation processes which include driving forces, deformation mechanisms and triggering mechanisms allow deformation to occur in a substrate (Oliveira et al., 2011; Owen et al., 2011). The driving forces are established for the various deformational structures discussed; they comprise reversed density gradient and shear stress. The shear stress may result in the current drag, increased pore pressure and pore-water movement in sediments. Liquefaction and fluidization are the main mechanisms of deformation in the study area; another mechanism is intergranular shear.

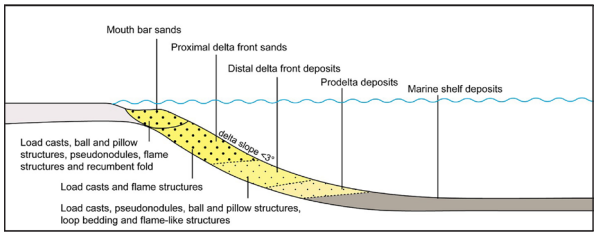

Figure 7. A cross-section across a delta lobe showing the occurrence and distribution of soft sediment deformation structures as observed in the study area (redrawn and modified after Nichols, 2009).

5.2 Deformation Mechanisms

Liquefaction and fluidization are the main deformation mechanisms in the study area. They are known to be the most common deformation mechanisms in unconsolidated, water-saturated sediments (Lowe, 1975; Allen, 1982; Owen, 1996; Moretti, 2000; Owen and Moretti, 2011). Liquefaction is known to occur when the grains are temporally suspended in a pore fluid either due to grain instability or excess pore water pressure (Lowe, 1975; Mills, 1983; Oliveira et al., 2011). Fluidization refers to the upward movement (i.e. fluid drag) of sediments' particles which results in dewatering or water-escape structures (Mills, 1983).

The load structures which include load casts, ball-and-pillow structures and pseudonodules are driven by gravitational forces, and are deformed mainly by liquefaction or reduction in shear stress of the sediments which make the sediments act as a viscous fluid. Flame structures are products of both liquefaction and fluidization. Fluidization occurs after liquefaction when the suspended grains have re-deposited, with a net movement of sediment particles downward. Subsequently, an upward flow of fluid through the fluidized sediments could result in the destruction of the original sediment fabric. Fluidization requires an external supply of fluid in an upward motion. The formation of recumbent folds is attributed to liquefaction (Mills, 1983) when the current shear (or lateral drag according to McKee et al., 1962) of a flowing fluid acts on the liquefied sand beds. Deformed laminations may be induced by liquefaction and loop beddings are probably induced by liquefaction and intergranular shear that occurred in cohesive, partially lithified, laminated sediments. Intergranular shear is a common deformation mechanism that results in brittle failure (such as syndepositional fractures) in cohesionless sediments (Owen, 1987) such as the coarse-grained sediments of the proximal delta front. Owen, 1995 suggested that the brittle failure occurs during a late stage in deformation when the deformation in the liquefied sediments is replaced by deformation through intergranular shear. Brittle failure is also common in partially liquefied sediment or sediment that was adjacent to liquefied sediment during deformation, such as sediment that was above a water table when liquefaction occurred (Bryant and Miall, 2010; Owen and Moretti, 2011).

5.3 Triggering Mechanisms

The triggering mechanisms for the deformation in the study are considered to be non-seismic or endogenic triggers (sensu Owen et al., 2011) based on the interpreted environment of deposition (EOD) and the relationship between sedimentary facies and the occurrence of soft-sediment deformation structures. The strata of the study

area are interpreted as prograding river-dominated and wave-influenced deltaic deposits. Generally, deltaic systems are typically associated with soft- sediment deformation structures due to slope instability, rapid sedimentation, storm waves, and/or overloading mainly in the proximal region with a high-flow discharge (Pulham, 1989, Bhattacharya and Walker, 1991 and 1992; Coleman, et al., 1983; Martinsen, 1989; Bann and Fielding, 2004; Oliveira et al., 2011). The Itigidi and Ediba outcrops have a low palaeoslope gradient (<3^{o}), so slope instability may not be an appropriate trigger for the deformation, and there is no evidence of slump structures in the outcrops. Overloading may be a triggering mechanism; it is induced by the rapid deposition of sands on a soft-substrate (Owen et al., 2011).

Although loop beddings have been considered as seismites by some authors (Calvo et al., 1998; Rodríguez-Pascua et al., 2000; Martín-Chivelet et al., 2011), for this research, the study area lacks evidence of tectonic signatures based on previous studies. Fractures are limited to joints; no structural displacements or folds occurred, neither is the basin known to be tectonically active. The soft-sediment deformation structures are not laterally extensive, and the deformed beds are not completely bounded above and below by undeformed units. The SSDS are only limited to the stratigraphic section at Itigidi.

6. Conclusions

This paper further reveals comprehensive soft-sediment deformation structures that are formed by endogenic triggers in a deltaic system. The encountered deformation structures are classified into three groups: i. load structure, which includes load casts, pseudonodules, ball-and-pillow structures and flame structures; ii. a ductile disturbed structure such as loop beddings, recumbent folds and deformed laminations; and iii. brittle deformed structure, which consists of syndepositional fractures. These deformations are formed mainly as a result of gravitational instabilities due to reversed density gradient and shear stress on liquefied or fluidized sediments. Non-seismic triggers such as rapid sedimentation, storm waves, and/or overloading are the major triggering mechanisms in the study area. The morphological, sedimentological, and stratigraphic characteristics of these soft-sediment deformations strongly indicate non-seismic or endogenic triggers. The presence of the ductile deformation structure – a loop bedding which has been regarded as a seismite (Calvo et al., 1998; Rodríguez-Pascua et al., 2000; Martín-Chivelet et al., 2011), occurs within an exclusively non-seismic triggered zone suggesting that the loop bedding is not exclusive to seismic trigger.

Acknowledgement

The authors are grateful to the community leaders of Itigidi and Ediba for their hospitality and assistance during the course of field work. The authors thank the undergraduate students of the Department of Geology, University of Nigeria, Nsukka who provided field assistance during the field mapping exercise as well as appreciate Mr Ikenna Okonkwo's useful information on the structural trend of the study area.

References

Alfaro, P., Delgado, J., Estévez, A., Molina, J., Moretti, M.,Soria, J. (2002). Liquefaction and fluidization structures in Messinian storm deposits (Bajo Segura Basin, Betic Cordillera, southern Spain. International Journal of Earth Sciences 91, 505–513.

Allen, J.R.L. (1982). Sedimentary Structures, their character and physical basis. Development in sedimentology 30B. Volume II, Amsterdam, Elsevier Scientific Publishing Company, 663 pp.

Bann, K. L. and Fielding, C. R. (2004). An integrated ichnological and sedimentological comparison of non-deltaic shoreface and subaqueous delta deposits in Permian reservoir units of Australia. [In:] McIlroy, D. (Eds.). The application of ichnology to palaeoenvironmental and stratigraphic analysis. Geological Society, London, Special Publications 228, 273–310.

Banerjee, I. (1981). Storm lag and related facies of the bioclastic limestones of the Eze Aku Formation (Turonian), Nigeria. Sedimentary Geology 26, 133–147.

Benkhelil, M.J. (1980). On deformations of the Cretaceous rocks in the lower Gongola area. J. Mining and Geol., 17, p. 163 – 169.

Benkhelil, J. (1982). Benue Trough and Benue chain. Geological Magazine 119, 155–168.

Benkhelil, J. (1986). Structure and geodynamic evolution of the intracontinental Benue Trough (Nigeria). Unpublished Thesis, Nice et Elf Nigeria SNEA (P), 202 pp.

Benkhelil, J. (1987). Structural frame and deformations in the Benue Trough of Nigeria. Bull. Centres Rech. Explor – Prod. Elf – Aquitaine, 11, 160 – 161.

Benkhelil, J. (1989). The origin and evolution of the Cretaceous Benue Trough (Nigeria). Journal of African Earth Sciences (and the Middle East) 8, 251–282.

Bhattacharya, H.N. and Bhattacharya, B. (2010). Soft-sediment deformation structures from an ice-marginal storm–tide interactive system, Permo-Carboniferous Talchir Formation, Talchir Coalbasin, India. Sedimentary Geology 223, 380–389.

Bhattacharya J. and Walker, R. G. (1991). Allostratigraphic subdivision of the Upper Cretaceous Dunvegan, Shaftesbury and Kaskapau formations, northwestern Alberta subsurface. Bulletin of Canadian Petroleum Geology 39, 145–164.

Bhattacharya, J.P. and Walker, R.G. (1992). Deltas. [In:] Walker, R.G., James, N.P. (Eds.), Facies Models: Response to Sea Level Change. Geological Association of Canada, St Johns, Newfoundland pp.157–178.

Blatt, H., Middleton, G.V., Murray, R.C. (1980). Origin of Sedimentary Rocks, second ed. Prentice-Hall, Englewood Cliffs, New Jersey.

Braide, S.P. (1992). Tectonic origin of preconsolidation deformation in Bima Sandstone, Yola Arm, Benue Trough. Nigerian Association of Petroleum Explorationist Bulletin 7, 40–45.

Brodzikowski, K. and Haluszczak, A. (1987). Flame structures and associated deformations in Quaternary glaciolacustrine and glaciodeltaic deposits: examples from central Poland. [In:] Jones, M.E., Preston, R.M.F. (Eds.), Deformation of sediments and sedimentary rocks. Geological Society Special Publication 29, 279–286.

Bryant, G. and Miall, A.D. (2010). Diverse products of near-surface sediment mobilization in an ancient eolianite: outcrop features of the early Jurassic Navajo Sandstone. Basin Research 22, 578–590.

Calvo, J.P., Rodriguez-Pascua, M., Martin Velasquez, S., Jimenez, S., de Vicente, G. (1998). Microdeformation of lacustrine laminate sequences from Late Miocene formations

of SE Spain: an interpretation of loop bedding. Sedimentology 45, 279–292.

Cole, R.D. and Picard, M.D. (1975). Primary and secondary structures in oil shale and other fine grained rocks, Green River Formation (Eocene), Utah and Colorado, Utah. Geology 2, 49–67.

Coleman, J. M., Prior, D. B., Lindsay, J. F. (1983). Deltaic influences on shelf edge instability processes. [In:] Stanly, D. J., Moore, G. T. (Eds.). The shelfbreak: critical interface on continental margins. Society of Economic Paleontologists and Mineralogists, Special Publication 33, 121-137.

Collinson, J., Mountney, N., Thompson, D. (2006). Sedimentary Structures. Hertfordshire, England, Terra Publishing, 292 pp.

Dim, C.I.P., Okwara, I.C., Mode, A.W., Onuoha, K.M. (2016). Lithofacies and environments of deposition within the Middle-Upper Cretaceous successions of Southeastern Nigeria. Arabian Journal of Geosciences 9, 1–17.

Dott, R.H. and Howard, J.K. (1962). Convolute laminations in non-graded sequences. Journal of Geology 70, 114-121.

Ekwenye, O.C., Nichols, G., Mode, A.W. (2015). Sedimentary petrology and provenance interpretation of the sandstone lithofacies of the Paleogene strata, south-eastern Nigeria. Journal of African Earth Sciences 109, 239–262.

Ettensohn, F.R., Rast, N., Brett, C.E. (2002). Ancient Seismites: Geological Society of America, Special Paper, 359.

Genik, G.J. (1992). Regional framework, structural and petroleum aspects of rift basins in Niger, Chad and the Central African Republic (CAR). Tectonophysics 213, 169 – 185.

Gibling, M.R., Tantisukrit, C., Uttamo, W., Thanasuthipitak, T., Haraluk, M. (1985). Oil shale sedimentology and geochemistry in Cenozoic Mae Sot Basin, Thailand. American Association of Petroleum Geologists Bulletin 69, 767–780.

Guiraud, M. and Plaziat, J.C. (1993). Seismites in the fluviatile Bima sandstones: identification of pameoseism and discussion of their magnitudes in a Cretaceous synsedimentary strike–slip basin (Upper Benue, Nigeria). Tectonophysics 225, 493–522.

Hoque, M. (1984). Pyroclastics from the lower Benue Trough of Nigeria and their tectonic implications. Journal of African Earth Sciences 2, 351 – 358.

Hoque, M. and Nwajide, C.S. (1984). Tectono-sedimentological evolution of an elongate Intracratonic basin (Aulacogen): the case of the Benue Trough of Nigeria. Nigerian Journal of Mining and Geology 21, 19–26.

Jones, G.P. (1962). Deformed cross-stratification in Cretaceous Bima Sandstone, Nigeria. Journal of Sedimentary Petrology 32, 231–239.

Kerr, M. and Eyles, N. (1991). Storm-deposited sandstones (tempestites) and related ichnofossils of the Late-Ordovician Georgian Bay Formation, southern Ontario, Canada. Canadian Journal of Earth Sciences 28, 266–282.

Kogbe, C.A. (1976). The Cretaceous and Paleogene sediments of Southern Nigeria. [In:] Kogbe, C. A., (Eds.), Geology of Nigeria. Elizabethan Publishing Company, Lagos, pp. 273–282.

Kuenen, P.H. (1958). Experiments in geology. Transactions of the Geological Society of Glasgow 23, 1–28.

Ladipo, K.O. (1988). Paleogeography, sedimentation and tectonics of the upper cretaceous Anambra basin, southeastern Nigeria. Journal of African Earth Sciences (and the Middle East) 7, 865-871.

Lowe, D. R. (1975). Water escape structures in coarse grained sediments. Sedimentology 22, 57–204.

Lunina, O. and Gladkov, A. S. (2016). Soft-sediment deformation structures induced by strong earthquakes in southern Siberia and their paleoseimsic significance. Sedimentary Geology 344, 5-19. DOI: 10.1016/j.sedgeo.2016.02.014

Martín-Chivelet, J., Palma, R.M., López-Gómez, J., Kietzmann, D.A. (2011). Earthquake-induced soft-sediment deformation structures in Upper Jurassic open-marine microbialites (Neuquén Basin, Argentina). Sedimentary Geology 235, 210-221.

Martinsen, O.J. (1989). Styles of soft-deformation on a Namurian (Carboniferous) delta slope, Western Irish Namurian Basin, Ireland. [In:] Whateley, M.K.G., Pickering, K.T. (Eds.), Deltas: Sites and Traps for Fossil Fuels: Geological Society, London, Special Publications, 41, 167–177.

McKee, E.D., Reynolds, M.A., Baker, C.H. (1962). Experiments on intraformational recumbent folds in cross-bedded sand. U.S. Geological Survey Professional Paper, 450-D, 155-160.

Mills, P.C. (1983). Genesis and diagnostic value of soft-sediment deformation structures--a review. Sedimentary Geology 35, 83–104.

Mode, A. W. (1991). Assemblage zones, age and paleoenvironment of the Nkporo Shale, Akanu area, Ohafia, southeastern Nigeria. Journal of Mining and Geology 27, (1), 107 – 114.

Mode A.W., Ekwenye, O.C., Oha, I.A., Onah, F.C. (2018). Facies analysis and ichnology of a prograding river-dominated and wave-influenced deltaic deposit: the Nkporo Formation in the Itigidi-Ediba region of the Afikpo Sub-basin, south-eastern Nigeria. Journal of African Earth Sciences. 10.1016/j.jafrearsci.2018.06.002.

Moretti, M. (2000). Soft-sediment deformation structures interpreted as seismites in middle–late Pleistocene aeolian deposits (Apulian foreland, southern Italy). Sedimentary Geology 135, 167–179.

Moretti, M., Soria, J. M. Alfaro, P., Walsh, N. (2001). Asymmetrical soft-sediment deformation structures triggered by rapid sedimentation in turbiditic deposits (Late Miocene, Guadix Basin, Southern Spain). Facies 44(1), 283-294, DOI: 10.1007/BF02668179.

Moretti, M. and Sabato, L. (2007). Recognition of trigger mechanisms for soft-sediment deformation in the Pleistocene lacustrine deposits of the Sant'Arcangelo Basin (Southern Italy): Seismic shock vs. overloading. Sedimentary Geology 196, 31–45.

Mohindra, R. and Bagati, T.N. (1996). Seismically induced soft-sediment deformation structures (seismites) around Sumdo in the lower Spiti valley (Tethys Himalaya). Sedimentary Geology 101, 69-83.

Molina, J. M., Alfaro, P., Moretti, M., Soria, J. M. (1998). Soft-sediment deformation structures induced by cyclic stress of storm waves in tempestites (Miocene, Guadalquivir Basin, Spain), Terra Nova 10, 145–150.

Maurin, J.C., Benkhelil, J., Robineau, B. (1986). Fault rocks of the Kaltungo lineament, northeastern Nigeria and their relationship with Benue Trough tectonics. Journal of Geological Society of London 143, 587 – 599.

Murat, R.C. (1972). Stratigraphy and palaeogeography of the Cretaceous and Lower Tertiary in southern Nigeria. [In:] Dessauvagie, T.F.J., Whiteman, A.J. (Eds.), African Geology. University of Ibadan Press, Nigeria pp. 251–266.

Nichols, G. (2009). Sedimentology and Stratigraphy, second ed. Blackwell Publishing Oxford, United Kingdom, 419 pp.

Nwachukwu, S.O. (1972). The tectonic evolution of the southern portion of the Benue Trough, Nigeria. Geological Magazine 109, 411–419.

Nwajide, C.S. (2005). Anambra Basin of Nigeria: Synoptic basin analysis as a basis for evaluating its hydrocarbon prospectivity. [In:] Okogbue, C.O. (Eds.) Hydrocarbon potentials of the Anambra basin: geology, geochemistry and geohistory

perspectives. Proceedings of the 1st seminar organized by Petroleum Technology Development Fund Chair in Geology, University of Nigeria, Nsukka, pp.1–46.

Nwajide, C. S. (2013). Geology of Nigeria's Sedimentary Basins. CSS Bookshops Limited, Lagos. 565 pp.

Obi, G.C. and Okogbue, C.O. (2004). Sedimentary response to tectonism in the Campanian–Maastrichtian succession, Anambra Basin, southeastern Nigeria. Journal of African Earth Sciences 38, 99–108.

Odigi, M.I. (2011). Diagenesis and reservoir quality of cretaceous sandstones of Nkporo Formation (Campanian) southeastern Benue Trough, Nigeria. Journal of Geology and Mining Research 3, 265–280.

Olade, M.A. (1975). Evolution of Nigeria's Benue Trough (aulacogen): a tectonic model. Geological Magazine 112, 575–583.

Olade, M. A. (1979). The Abakaliki pyroclastics of southern Benue Trough, Nigerian Journal of Mining and Geology 16, 17-25.

Olabode, S. O. (2014). Soft sediment deformation structures in the Maastrichtian Ajali Formation Western Flank of Anambra Basin, southern Nigeria. Journal of African Earth Sciences 89, 16–30.

Oliveira C. M.M., Hodgson D. M., Flint S. S. (2011). Distribution of soft-sediment deformation structures in clinoform successions of the Permian Ecca Group, Karoo Basin, South Africa. Sedimentary Geology 235, 314–330.

Okoro, A. U., Okogbue, C.O., Nwajide, C. S., Onuigbo, E. N. (2012a). Provenance and paleogeography of the Nkporo Formation (Late Campanian – Early Maastrichtian) in the Afikpo Sub-Basin, Southeastern Nigeria. European Journal of Scientific Research 88, 346–364.

Okoro A. U., Onuigbo, E. N., Akpunonu E. O., Obiadi I. I. (2012b). Lithofacies and pebble morphogenesis: Keys to paleoenvironmental interpretation of the Nkporo Formation, Afikpo Sub-Basin, Nigeria. Journal of Environment and Earth Science 2, (6), 26-38.

Owen, G. (1987). Deformation processes in unconsolidated sands. [In:] Jones, M. E., Preston, R. M. F., Deformation of Sediments and Sedimentary Rocks (Eds.), Geological Society of London 29, 11–24.

Owen, G. (1995). Soft-sediment deformation in Upper Proterozoic Torridonian sandstones (Applecross Formation) at Torridon, northwest Scotland. Journal of Sedimentary Research A65, 495–504.

Owen, G. (1996). Anatomy of a water- escape cusp in Upper Proterozoic Torridon Group sandstones, Scotland. Sediment. Geol.103, 117–128.

Owen, G. (2003). Load structures: gravity-driven sediment mobilization in the shallow subsurface, Geological Society Special Publication 216, 21–34.

Owen, G. and Moretti, M. (2011). Identifying triggers for liquefaction-induced soft-sediment deformation in sands. Sedimentary Geology. Sedimentary Geology 235, 141–147.

Owen, G., Moretti, M., Alfaro, P. (2011). Recognising triggers for soft-sediment deformation: Current understanding and future directions. Sedimentary Geology 235, 133–140.

Petters, S.W. (1978). Mid-Cretaceous paleoenvironments and biostratigraphy of the Benue Trough, Nigeria. Geological Society of America Bulletin 89, 151–154.

Petters S. W. and Edet, J. (1996). Shallow shelf and anoxic facies in the Late Campanian – Early Maastrichtian of SE Nigeria. Geologie de I' Afrique et L' Atlantique sud: Actes colloques Angers. 220 – 227.

Põldsaar, K. and Ainsaar, L. (2014). Extensive soft-sediment deformation structures in the early Darriwilian (Middle Ordovician) shallow marine siliciclastic sediments formed on the Baltoscandian carbonate ramp, northwestern Estonia. Marine Geology 356, 111-127.

Popoff, M., Kampunzu, A. B., Coulon, C., Esquevin, J. (1982). Découverte d'un volcanisme mésozoique dans le nord-est du Nigéria datations absolues, caractères magmatiques et signification géodynamique dans l'évolution du rift de la Bénoué: in Rifts et Fossés Anciens, résumé. Trav. Lab. Sci. Terre, Marseille St Jérôme (B), 19, 47- 49. Not seen, cited from Benkhelil, J. (1986). Structure and geodynamic evolution of the intracontinental Benue Trough (Nigeria). Unpublished Thesis, Nice et Elf Nigeria SNEA (P), 202pp.

Popoff, M., Wiedmann, J., De Clasz, I. (1986). The Upper Cretaceous Gongila and Pindiga Formations, northern Nigeria: subdivisions, age, stratigraphic correlations and paleogeographic implications. Eclogae Geologicae Helvetiae 79, 343 – 363.

Pulham, A. J. (1989). Controls on internal structure and architecture of sanstone bodies within Upper Carboniferous fluvial-dominated deltas, County Clare, western Ireland. [In:] Whateley, M.K.G., Pickering, K.T., (Eds.), Deltas: sites and traps for fossil fuels. Oxford, Blackwell Scientific Publications, Geological Society, Special Publication 41, p. 179-203.

Reyment, R.A. (1965). Aspects of the Geology of Nigeria: The stratigraphy of the Cretaceous and Cenozoic deposits, Ibadan University Press, Ibadan, 145 pp.

Rodríguez-Pascua, M.A., Calvo, J.P. De Vicente, G., Gómez-Gras, D. (2000). Soft-sediment deformation structures interpreted as seismites in lacustrine sediments of the Prebetic Zone, SE Spain, and their potential use as indicators of earthquake magnitudes during the Late Miocene. Sedimentary Geology 135, 117–135.

Samaila, N.K., Abubakar, M.B., Dike, E.F.C., Obaje, N.G. (2006). Description of soft-sediment deformation structures in the Cretaceous Bima Sandstone from the Yola Arm, Upper Benue Trough, Northeastern Nigeria. Journal of African Earth Sciences 44, 66-74.

Sanders, J.E. (1960). Origin of convoluted laminae. Geol. Mag., 97, 409-421.

Shanmugam, G. (2017). The fallacy of interpreting SSDS with different types of breccias as seismites amid the multifarious origins of earthquakes: Implications. Journal of Palaeogeography, 6(1), 12-44.

Sarkar, S., Choudhuri, A., Banerjee, S., Van Loon, A. J., Bose, P. K. (2014). Seismic and non-seismic soft-sediment deformation structures in the Proterozoic Bhander Limestone, central India. Geologos 20 (2), 89–103. doi: 10.2478/logos-2014-0008.

Simpson, A. (1954). The Nigerian coalfield. The geology of parts of Onitsha, Owerri and Benue provinces. Bull. Geol. Survey Nigeria 24, 85.

Trewin, N.H. (1986). Palaeoecology and sedimentology of the Achanarras fish bed of the Middle Old Red Sandstone, Scotland. Trans. R. Soc. Edinburgh, Earth Sci. 77, 21–46.

Topal, S. and Özkul, M. (2014). Soft-sediment deformation structures interpreted as seismites in the Kolankaya Formation, Denizli Basin (SW Turkey). The Scientific World Journal Article ID 352654, 1-13. http://dx.doi.org/10.1155/2014/352654

Van Loon, A.J. (2009). Soft-sediment deformation structures in siliciclastic sediments: an overview. Geologos 15, 3–55.

Vanneste, K., Meghraoui, M., Camelbeeck, T. (1999). Late Quaternary earthquake-related soft-sediment deformation along the Belgian portion of the Feldbiss Fault, Lower Rhine Graben system. Tectonophysics 309, 57-79.

Wright, J.B. (1981). Review of the Origin and Evolution of the Benue Trough in Nigeria. Earth Evolution Science 2, 98-103.

JJEES

JJEES (2020) 11 (1): 12-17
ISSN 1995-6681

Jordan Journal of Earth and Environmental Sciences

Use of GPR for Imaging Subsurface Archaeological Remains in the Islamic City of Ayla, Aqaba, Jordan

AbdEl-Rahman Abueladas

Al-Balqa Applied University, Faculty of Engineering, Department of Surveying and Geomatics Engineering, Jordan

Received 29 January 2019, Accepted 26 August 2019

Abstract

The Islamic city of Ayla was founded in the eighth century. The city is located adjacent to the beach and extends for a few tens of meters north of the Gulf of Aqaba shoreline. The city was, once, a flourishing and commercial port, communicating with other ports around the Indian Ocean and with the Far East. The city had land roads that connect with Egypt, Iraq, Syria, and the Arabian Peninsula.

The excavated ruins and other features are related to an ancient Islamic city.

The ground penetrating radar survey was carried out using a Subsurface Interface Radar System- (SIRvoyer-20) with two different central frequency monostatic antennae 900 MHz and 400 MHz to target abundant subsurface buried archaeological material for forward excavations.

The interpretation of radar cross section (radargram) shows many buried features with different patterns, widths, and shallow depths between 0.20 m to 0.6 m. These anomalies are corresponding to the depth of the excavated walls in the study area.

GPR anomalies are discontinuous and being shifted and located at a high liquefaction susceptibility zone confirms that several earthquakes have rocked Aqaba and Gulf of Aqaba region.

Keywords: Islamic city of Ayla, Ground penetrating radar, Monostatic antenna, liquefaction, buried walls.

1. Introduction

The city of Aqaba is situated at the northern part of Gulf of Aqaba, about 320 km south of the capital of Jordan Amman (Figure 1a). Aqaba has been an important trading city throughout history, including the Roman, Nabatane, Byzantine, and Islamic times (from first century (BC) to present). Aqaba Sea routes lead to East and North Africa and the ports of southern Asia. Land routes have carried trade with Syria, North Africa, and the Hejaz.

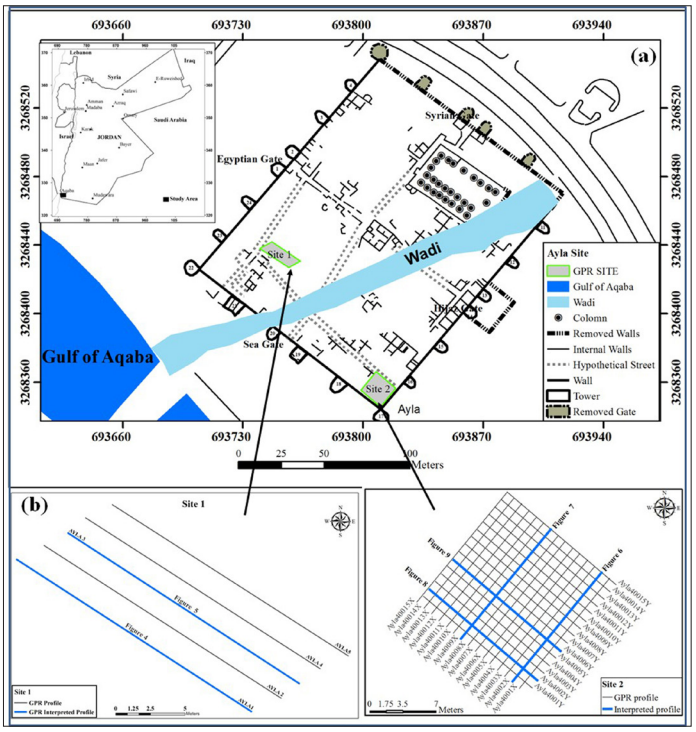

Figure 1. a) Location map of the study area showing the plan of excavations at the Islamic city of Ayla from 1986 to 1993 (Whitcomb 1994). **b)** Location map of the GPR profiles at the two sites.

* Corresponding author e-mail: aabueladas@bau.edu.jo

The discovery and delineation of the layout of the early Islamic city of Ayla is the result of excavations from 1986 through 1995 directed by Whitcomb (1990, 1991, 1994a, 1994b, 1994c, 1995, 1997, 2001) from University of Chicago. The excavations were carried out by the University of Chicago and the American Center of Oriental Research (ACOR), with the support of the United States Agency for International Development (USAID), in cooperation with the Department of Antiquities of Jordan.

GPR is an electronic device that emits Electromagnetic (EM) waves and determines the location of reflected energy. It has become a widespread instrument for usage in different fields, including geology, archaeology, the environment, engineering and construction, glaciology, and forensic science.

The GPR survey has been used to map buried remains or other construction features, the localization of tombs, burial mounds, shallow graves and the reconstruction of archaeological layers. The purpose of the surveys was to map the existence of uncovered subsurface archeological remains at a shallow depth, and, therefore, direct the archaeologists to the areas to be excavated.

2. Historical Background

The Islamic Ayla city was constructed by Caliph Othman Ben Afen around 650 AD. It was a flourishing city during the Umayyad period (650-750 AD) and the Abbasid period (750-970 AD) (Whitcamb, 1989a, 1989c, 1990, 1991) and also during the Fatimaied period (970-1116 AD) (Whitcamb, 1989b). The city was a very important port, and the artifacts found in the site indicated a commercial contact with ports in the Indian Ocean and the Far East; however, most of that contact was with the Arabian Peninsula, Egypt, Iraq, and with Syria using the road networks (Whitcamb, 1987). The city was established in a fortified 170 x 145 meters rectangle, with walls that are 4.5 meters high and 2.6 meters thick and is surrounded by twenty-four towers (Figure 1a). Excavations in 1987 at the site of the early Islamic Ayla (modern Aqaba, Jordan) revealed a city plan which included four gates (Whitcomb, 1987). The gates spread on all four sides as follows: the Damascus Gate (east), Door of the Sea (west), Door of the Hejaz (south), and Door of Egypt (north) (Figure 1a). In any Islamic city, the mosque is a very important building, and, here, it is located northeast of the city (Whitcamb 1994), (Figure 1a). Whitcomb (1993) theorised that the wadi running through the Islamic City of Ayla originated from earth's structural weakness. Such a fault was indicated on his site plan (Figure 1a). However, excavations by Rucker and Niemi (2005) of the Northeast corner tower of the walled city in the wadi and the interpretation of the 1918, 1945, and 1953 air photos indicated that the wadi was man-made. The city was destroyed in the late twelvth century by attacks of Bedouins, Crusaders, and also as a result of earthquakes. Whitcomb (1994) showed through a detailed mapping of the ancient architecture that this ancient city experienced subsidence due to several earthquakes.

The historical records indicate that numerous destructive earthquakes have occurred over the past 2000 years, and many of them are documented in Roman, Byzantine, and various Arabic sources (e.g. Guidoboni, 1994; Ambraseys, 2009). Several earthquakes are believed to have rocked Aqaba and the Gulf of Aqaba region in 1068, 1212, 1458, and 1588 A.D. (Ambraseys and Melville, 1989). The archaeological record verifys that a major damage to the Byzantine structures occurred in Aqaba in the 363 A.D. earthquake (Parker, 1999; Thomas et al., 2007). Also, a major damage occurred in the Islamic City of Ayla by the 1068 earthquake (Ghawanmeh, 1992; Whitcomb, 1994; Allison, 2013) which dstroyed the city of Aqaba (e.g. Guidoboni, 1994; Ambraseys, 2009). A comparison of the GPR images with the magnetic gradiometry maps were used by Conyers (2016) in order to provide information about buried buildings. GPR investigations are considered as an effective method to understand the ruins (Nawabi, 2016). The site was apparently never reoccupied after this earthquake. The geotechnical investigations carried out at the site showed sinking and tilting of the external walls, which was interpreted as slumping due to horizontal ground acceleration in an earthquake (Al-Hamoud and Tal, 1998). In the 1995 Nuweiba earthquake, many areas along the shoreline zone near Ayla ancient beared experiencing subsidence (Malkawi et al., 1999; Al-Tarazi 2000). The abundant groundwater and the shallow water table contributed to the rest and security of travelers and Hajj caravans from North Africa, Palestine, and Egypt, before continuing their journey through the desert. In other words, the shallow water table and shallow saturated sand demonstrated that Ayla lies in a high liquefaction susceptibility zone. (Mansoor et al., 2004; Abueladas, 2014). (Figure 2).

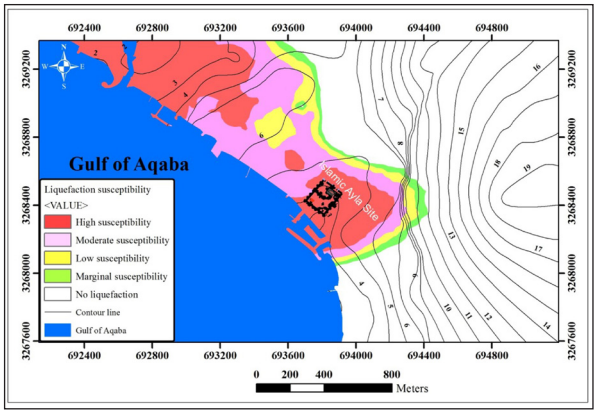

Figure 2. Map showing the ground water depth and the location of the liquefaction susceptibility zones (Abueladas, 2014).

3. GPR Concepts

The GPR technique, as a method of scientific investigation, has become an important technique that is neither destructive nor invasive, used for discovering, recovering, mapping, and understanding subsurface archeological data.

With this technique, a short pulse of high frequency (10 to 1,000 MHz) electromagnetic energy is transmitted into the ground from a shielded antenna pulled slowly across the ground at speeds varying from about 0.25– 4 m/h. The speed is dependent on the amount of detail desired and on the nature of the target.

The GPR signal is reflected, refracted, and attenuated depending on the distribution of the dielectric constant and electrical conductivity of the subsurface. These electrical

properties are highly dependent on the water content of the subsurface, and the presence of a high porosity environment.

The radar signal velocities are related to the relative permittivity by:

$$v = c/\sqrt{\mu_r \varepsilon_r} \quad \ldots\ldots\ldots\ldots\ldots\ldots\ldots\ldots\ldots\ldots\ldots\ldots (1)$$

where is the ratio of the dielectric permittivity of the medium to the dielectric permittivity of free space, is the relative magnetic permeability of the medium, and $c=3\cdot10^8$ m/s is the velocity of the EM waves in free space. Because is close to unity for most rock materials, radar velocity is primarily controlled by.

The dielectric permittivity across an interface causes part of an impinging radar pulse to be reflected. The radar signal amplitude is decreased at a reflecting boundary depending on the contrast and the thickness of the layer. The amount of the reflected energy related to signal amplitude is given by the reflection coefficient (R) (Neal, 2004). The reflection coefficient is defined as:

$R= \{(\varepsilon_{r2})^{1/2} - (\varepsilon_{r1})^{1/2}\}/ \{(\varepsilon_{r2})^{1/2} + (\varepsilon_{r1})^{1/2}\}$

Where ε_{r1} and ε_{r2} are the relative dielectric permittivity of the adjacent layers 1 and 2, or:

$R= \{(v_2)^{1/2} - (v_1)^{1/2}\}/ \{(v_2)^{1/2} + (v_1)^{1/2}\}$

The attenuation of a radar wave and its depth of penetration depend on the electrical conductivity and the dielectric constant of the media through which the wave propagates can be reduced for the case of low-loss media $\sigma/\varepsilon_w \ll 1$ to a simple form $\alpha = (\sigma/2) \times (\mu/\varepsilon_r)^{0.5}$ Where α donates the attenuation constant, and σ combines both the direct current (D.C.) conductivity and dielectric losses. The depth of penetration depends on the used frequency (the lower the frequency, the deeper the penetration) and on the conductivity of the materials (the higher the conductivity, the higher the penetration).

The horizontal resolution relates to the capability to detect a reflector position in space or time, which is a function of the pulse width (Neal, 2004). The vertical resolution increases with the increase in the frequency (Knapp, 1990). The vertical resolution is also controlled by wavelength (λ) (Knapp, 1990) which is a function of velocity and frequency:

$\lambda = v/f$

The optimum vertical resolution can be attained using one-quarter of the dominant wavelength (Sheriff, 1977).

The reflected energy is processed and displayed as a continuous strip chart recording of distance versus time. The depth of penetration of a GPR system is highly site-specific, and depends upon the soil and rock characteristics at the site, moisture content, and the frequency of the antenna (Battayneh et al., 2002).

The GPR data can be collected either by the fixed offset method in which the transmitter and the receiver antennas are separated by a fixed distance and moved across the area in regular steps, or by the common midpoint (CMP) mode in which the antennas are gradually separated from one another in constant steps. The CMP mode is often used to determine the velocity of the radar wave propagation through the subsurface.

The GPR methodology is similar to that of the shallow seismic reflection surveying in that these methods use the reflection of energy from underground features, but they differ largely in their site-specific applicability (Figure 3).

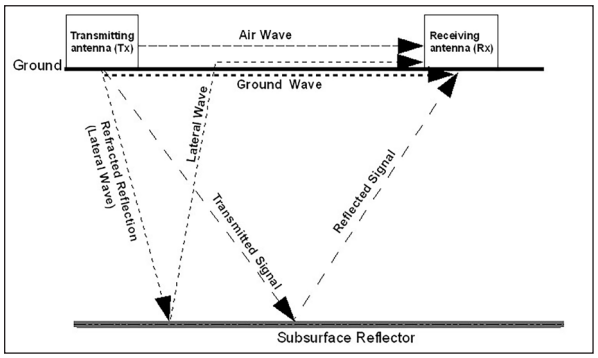

Figure 3. Ray paths between transmitting and receiving antennae (Neal, 2004). The diagram shows the ground surface along which the airwave and ground waves travel as well as the refracted lateral wave and the reflected wave. Modified after Fisher et al. (1996).

4. GPR Survey

4.1 Data aquisition

A continuous GPR survey was conducted using a Subsurface Interface Radar System- (SIRvoyer-20) manufactured by the Geophysical Survey System (GSSI) (Al-Ruzouq et al., 2018).

Two different central frequency antennae were used, namely the 900 MHz and 400 MHz antennae. The 400 MHz antenna is an excellent compromise between vertical resolution and depth penetration.

A total of 550 meters of GPR were collected along thirty-five profiles at two sites. The first survey site was located south-west of the Islamic city of Ayla, and the second was located at the south-east corner of the study area (Figure 1b).

4.2 Data processing

The GPR data were processed using the Geophysical Information System (GSSI) RADAN V software package.

Generally, attenuation reduces the radar signal with the increased travel time. Therefore, it is important to increase the weaker signals at greater receiver arrivals. Gains and color transformation are applied to increase the visibility of low amplitude features.

In the processing of the exhibited waveforms, two types of time domain filters, namely the finite impulse response (FIR) and infinite impulse response (IIR), were applied.

The horizontal and vertical high-pass filters have been used to remove the ringing system noise, and the horizontal and vertical low-pass filters have been applied to eliminate high-frequency noise from the GPR signal and to enhance the radar cross section. Data were stacked in a horizontal direction to get a clearer data dislpay. In the radargram, the vertical axis showed a two-way travel time (TWT) in nanoseconds (ns) (Ulriksen, 1982).

It is very important to calculate the subsurface radar wave velocity of the near-surface materials in order to convert the two-way travel time (TWT) of the reflected signal to the true depth of the reflector. The first way for estimating the GPR velocity is to measure TWT to a horizontal layer or buried object of an known depth (Annan, 2003; Topp et al., 1980; Fisher, 1992). However, the velocity was calibrated according to the known depth aligned with the top of the excavated wall in the study area.

The near-surface radar wave velocity estimates ranged

from 0.10 to 0.12 m/ns at the Ayla site. An average velocity of 0.11 m/ns was adopted for general use at the site.

5. Results and Discusstion

Because the GPR anomalies of man-made origin are generally specified by their pattern and extension, rather than by their numeric values alone, so the results of the GPR data of the archaeological sites are generally shown graphically. When presented graphically, one can distinguish the cultural and natural patterns better, and imagine the physical phenomena causing the detected anomalies.

A reconnaissance survey was conducted by recording five continuous parallel profiles, up to 20 m long at site 1. The separation between the northwest-southeast adjacent profiles was 1 m (Figure 1b).

In the radargram of figure 4, two strong anomalies are visible really well due to the presence of a strong reflector at a depth of about 0.6 and 0.5 m. The first anomaly may correspond to the buried wall. The second strong anomaly appears as a diffraction hyperbolas shape with high amplitudes observed at a depth of 0.5 m, and is probably caused by a metal pipe (Figure 4).

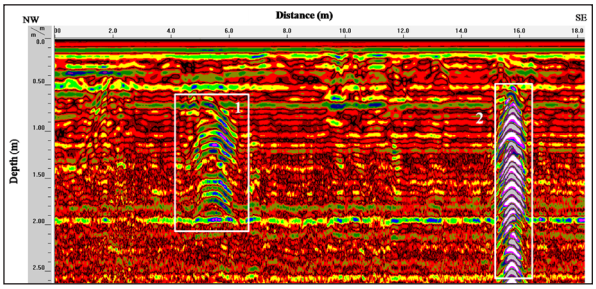

Figure 4. Part of the radar profile (400 MHz antennae) along Ayla 1. The first anomaly may represent a buried wall that is 0.6 m deep. The second anomaly is probably caused by a metal pipe that is 0.5 m deep.

GPR profile Ayla 3 runs parallel to profile Ayla 1 (Figure 1b). The radargram shows two anomalies at a depth of about 0.3 m (Figure 5). These reflectors are probably caused by two shallow walls.

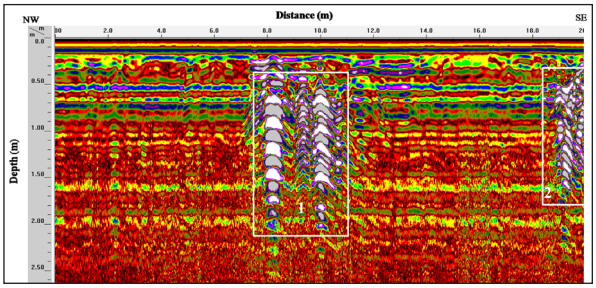

Figure 5. Radar profile (400 MHz antennae) along Ayla 3. The two main anomalies may represent 0.3 m deep buried walls.

Site 2 was a rectangle of 15 x 15 m, applied to the south-east of Islamic city of Ayla (Figure 1b). The uni-directional survey was conducted along fifteen profiles oriented approximately SW-NE, and fifteen profiles SE-NW oriented being 1 m apart, using the 400 and 900 MHz antennae.

In the radargram of figure 6, two strong anomalies are pictured at depths of about 0.5 and 0.3 m (Figure 6). These anomlaies perhaps refer to buried walls.

A hyperbolic event in the radargram at a depth of almost 1m as in figure 7 probably refer to a 0.3 m deep wall.

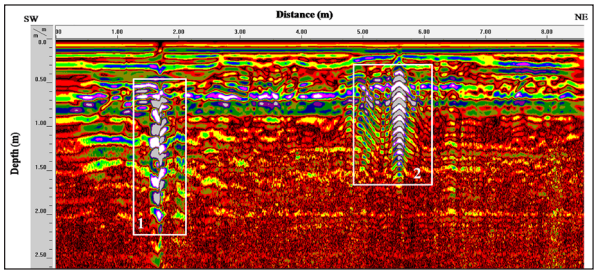

Figure 6. Part of the radar profile (400 MHz antennae) along Ayla4002x. The two main anomalies may represent 0.5 m and 0.3m deep buried walls.

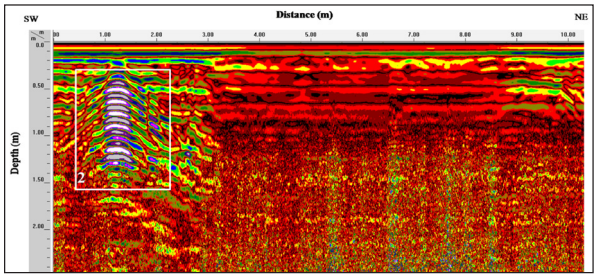

Figure 7. Radar profile (400 MHz antennae) along Ayla4009x. The hyperbolic- shaped anomaly may represent a 0.3 m deep buried wall.

GPR profile Ayla4002y runs perpendicular to Ayla4002x (Figure 1b). The two 0.3 and 0.5 m deep anomalies probably represent shallow buried walls (Figure 8).

Two different antenna frequencies were applied along this profile Ayla4006y (Figure 1b). In the radargram of figure 9a (400 MHz antennae), three anomalies are well visible due the presence of a strong reflector at about 0.2 m, 0.3 m and 0.5 m deep. The same anomaly can be seen at the 900 MHz profile (Figure 9b).

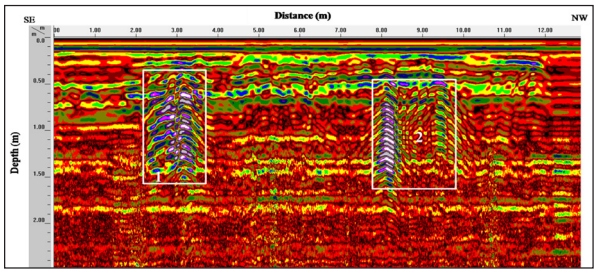

Figure 8. Part of the radar profile (400 MHz antennae) along Ayla4002y. The two 0.3 and 0.5 m deep anomalies probably represent shallow buried walls.

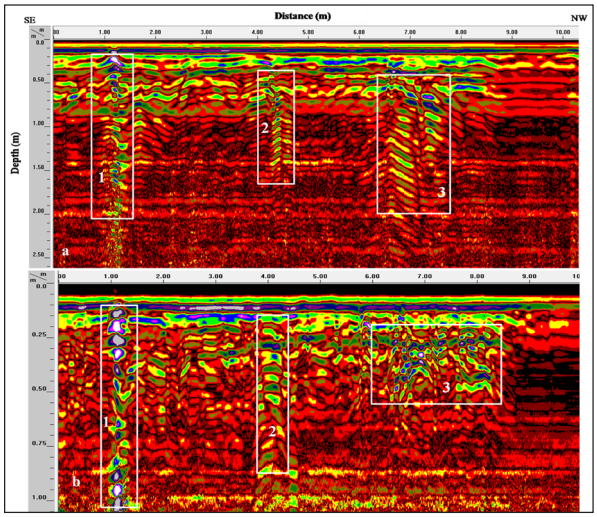

Figure 9. a) Part of the radar profile (400 MHz antennae) along Ayla 4006y. **b)** Part of the radar profile (900 MHz antennae) along Ayla 9006y. Both profiles show the same anomalies.

The GPR radargram profiles revealed many different subsurface anomalies across the study area located at different depths from 20 to 60 cm at both sites (Figure 10). Some of these anomalies are isololated and others are continuous. The anomaly map shows individual features at both sites. The anomalies appear similar to the GPR signature of the buried walls or scattered blocks at site 1 (Figure 10a), except for the second anomaly along profile Ayla1, which was probably caused by a metal pipe located at 50 cm (Figure 4).

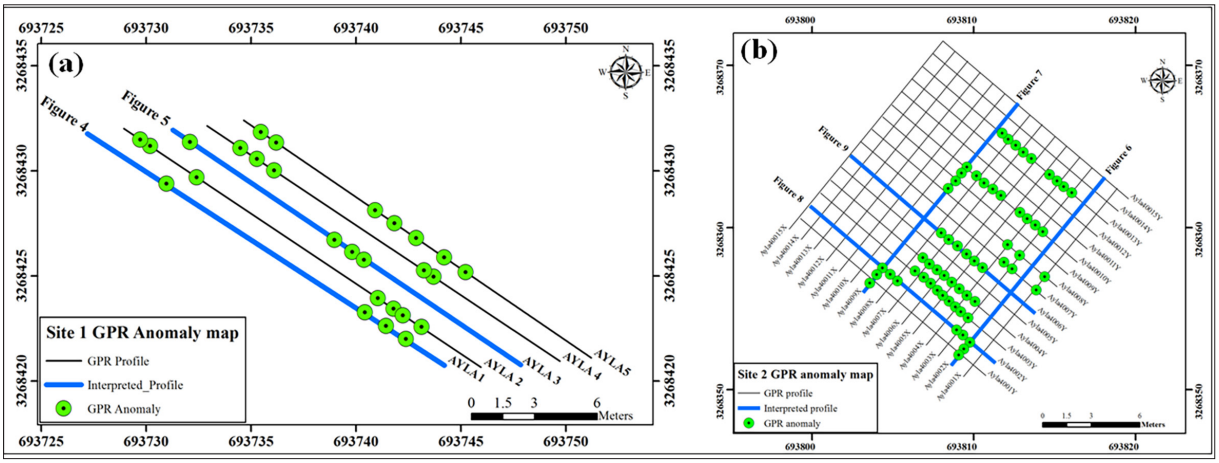

Figure 10. a) GPR anomaly location map, site 1. b) GPR anomaly location map, site 2.

Many anomalies were pictured at site 2, especially at the north-east and noth-west parts of this site. Continuous anomalies may represent buried walls (Figure 10b). The shape and direction of these anomalies are similar to the excavated walls which refer to the Egyptian, Hijaz, and Syria gates (Figure 1a). Other individual anomalies represented by walls had collapsed due to earthquakes.

6. Conclusions

Geophysical methods are intensively used for both the rescue and exploration of archaeology in some countries.

The main advantage of the GPR method is its capability of investigating a structure or a site with a non-destructive and a non-invasive technique, i.e., without digging, boring or causing changes to its original structure or shape especially in an urban area such as the Islamic Ayla site.

The GPR successfully produced images of the subsurface and the burried walls by using high and medium-frequency. It proved to be an excellent tool for the distinguishing and delineation of subsurface structures which are clearly expected to be of an archaeological interest.

The flat topography, the presence of sand and gravel, and the good electrical-property contrasts between a stonewall and sand at the study sites can help detect the anomalous zones at the study area.

Most of the archaeological anomalies are concentrated in the NE and SE parts of site 2.

The shallow hidden feature with depths between 10 cm to 60 cm mapped by GPR can interfere in the preservation of buried heritage and may provide basic information not only to increase the knowledge of the past, but also to aid in planning any future excavations.

The scattering anomalies at both sites may indicate damaged or missplaced wall sections due to several natural factors including earthquakes, or human activities such as wall demolition, removal, or reconstruction. The confirmation has been extemely difficult without excavations.

Acknowledgements:

The authors acknowledge colleagues, including Emad Alheyari, Yousef Alfaori, Abu Ali Aqrabawi, Musa Aldabbas, and Ziad Heyassat (from Al-Balqa Applied University, Jordan) who jointly participated in the collection of field data. The authors extend thanks also to the anonymous reviewers and the editor for their constructive criticsm and comments.

References

Abueladas, A. (2014). Assessment of Seismic Hazards along the northern Gulf of Aqaba. Dissertation, University of Missouri-Kansas City, PhD thesis, 107- 109.

Al-Homoud, A.S. and Tal, A.B. (1998). Geotechnical study for evaluating stability and restoration work at the 1,000 year old archaeological site of Ayla, Gulf of Aqaba, Kingdom of Jordan. Environmental and Engineering Geosciences 4(1), 103-114.

Allison, A., (2013). Paleoseismology and archaeoseismology along the southern Dead Sea Transform in Wadi Arabah near the municipality of Aqaba, Jordan. Ph.D. Thesis, University of Missouri Kansas City.

Al-Ruzouq, R., Venkatachalam, S., Abueladas, A., Abu Dabou, S. (2018). Geomatics for economic archaeological documentation and management. Applied Geomatics 10 (22), 1-20.

Al-Tarazi, E. (2000). The major Gulf of Aqaba earthquake, 22 November 1995- Maximum intensity distribution. Natural Hazards 22, 17–27.

Ambraseys, N. N. and Melville, C. P. (1989). Evidence for intraplate earthquake in northwest Arabia. Bulletin Seismological Society America 79, 1279–1281.

Ambraseys, N.N. (2009). Earthquakes in the Mediterranean and Middle East: A Multidisciplinary Study of Seismicity up to 1900. Cambridge University Press. Cambridge, UK, p. 947.

Annan, A. P. (2003). Ground Penetrating Radar Principles, Procedures and Applications. Sensors and Software Inc., 286 p.

Battayneh, A., Abueladas, A., Moumni, K. (2002). Use of the ground- penetrating radar for assessment of potential sinkhole conditions: an example from Ghor al Haditha area, Jordan. Environmental Geology 41, 977-983.

Conyers, L. B. (2016). Ground-Penetrating Radar Mapping Using Multiple Processing and Interpretation Methods. Remote Sens. 2016, 8(7). doi.org/10.3390/rs8070562.

Fisher, E. (1992). Examples of reverse-time migration of single-channel, ground- penetrating radar profiles. Geophysics 57(4), 577-586.

Fisher, S.C., Srewart, R.R., Jol, H.M. (1996). Ground penetrating radar (GPR) data enhancement using seismic techniques. J. Environ. Eng. Geophys. 1, 89-96.

Ghawanmeh, Y.H. (1992). Earthquake effects on Bilad Ash -Sham settlements, studies in history and archaeology of Jordan. IV, S. Tell (Ed.), Amman, Department of Antiquities, 53-59.

Guidoboni, E. (1994). Catalogue of ancient earthquakes in the Mediterranean area up to the 10th century. Roma, Italy. Istituto Nazionale di Geofisica, 504 pp.

Knapp, R.W. (1990). Vertical resolution of thick beds, thin beds and thin-bed cyclothems. Geophysics 55, 1183-1190.

Malkawi, A. H. and Alawneh, A. S. (1999). Dynamic Site Response Evaluation for the Chimney Located Near the Fertilizer Plant (Aqaba City). Research report, Civil Engineering Department, Jordan University of Science and Technology, Irbid, Jordan, 25 pp.

Mansoor, N. M., Niemi, T. M., Misra, A. (2004). GIS-Based Assessment of Liquefaction Potential of the City of Aqaba, Jordan. Environmental and Engineering Geoscience X (4), 297–320.

Nawabi, Y. A. (2016). A Non-Destructive Method for Archaeological Research using Ground Penetrating Radar: A Case Study in Chiba Prefecture, Japan. Waseda Rilas Journal 4(10), 122-139.

Neal, A. (2004). Ground-penetrating radar and its use in sedimentology: principles, problems and progress. Earth-Science Reviews (66), 261– 330.

Parker, S.T. (1999). Brief notice on a possible early 4th century church at Aqaba, Jordan. J. of Roman Archaeology 12, 372-376.

Rucker, J.D. and Niemi, T.M. (2005). New excavations of the city wall at Islamic Ayla in Aqaba, Jordan. Annual of Department of Antiquities of Jordan (49), 501-508.

Sheriff, R.E. (1977). Limitations on resolution of seismic reflections and geologic detail derivable from them. Applied geophysics (20), 3-14.

Thomas, R., Niemi, T.M., Parker, S.T. (2007). Structural damage from earthquakes in the second- 9th Century at the archaeological site of Aila in Aqaba, Jordan. Bulletin of the American School of Oriental Research (346), 59-77.

Topp, G.C., Davis, J.L., Annan, A.P. (1980). Electromagnetic determination of soil water content: measurements in coaxial transmission lines. Water Resour. Res. (12), 574-582.

Ulriksen, C. P. (1982). Application of impulse radar to civil engineering. Ph.D. Thesis, Lund University of Technology.

Whitcomb, D. (1987). Excavations in Aqaba: First Preliminary Report. ADAJ (32), 247.

Whitcomb, D. (1989a). Evidence of the Umayyad period from Aqaba excavations. The fourth international conference o the history of Bilad al-Sham during the Umayyad period. (Eds.) Bakhit, M.A. and Schick, R. University of Jordan (2), 164-84.

Whitcomb, D. (1989b). Coptic glazed ceramics from the excavations atAqaba, Jordan. JARCE 26, 167-82.

Whitcomb, D. (1989C). Mehesh ware: Evidence of early Abbasid occupation from southern Jordan. ADAJ 33, 269-85.

Whitcomb, D. (1990). "'Dioceltian's" misr at 'Aqaba. Zeitschrift des Deutschen Palestina Vereins 106, 156-161.

Whitcomb, D. (1991). Excavations in the site of Medieval 'Aqaba. In ANONYMUS 1991, 123-130.

Whitcomb, D. (1993). n.d. Out Arabia: Early Islamic Aqaba in its regional context, Paper prepared for Colloque d'archeologie islamque, Cairo.

Whitcomb, D. (1994). Ayla: Art and Industry in the Islamic Port of Aqaba. Special Publications, Oriental Institute, University of Chicago, Chicago, IL: 32.

Whitcomb, D. (1994a). Amsar in Syria, Syrian cities after the conquest. ARAM 6, 13-33.

Whitcomb, D. (1994b). Ayla. Art and Industry in the Islamic Port of Aqaba (Oriental Institute Museum Publications). Chicago.

Whitcomb, D. (1994c). The Misr of Ayla: Settlement at al-'Aqaba in the Early Islamic Period. In King and Cameron 1994, 155-170.

Whitcomb, D. (1995). The Misr of Ayla: New Evidence for the Early Islamic City. Studies in the History and Archaeology of Jordan, 277-288.

Whitcomb, D. (1997). The Town and Name of 'Aqaba: An Inquiry into the Settlement History from an Archaeological Perspective. Studies in the History and Archaeology of Jordan VI, 359-363.

Whitcomb, D. (2001). Umayyad and Abbasid Periods. In Macdonald et al. 2001, 503-514.

JJEES

JJEES (2020) 11 (1): 18-25
ISSN 1995-6681

Jordan Journal of Earth and Environmental Sciences

The Impact of Composting on Air Quality in the Jordanian Badia

Mahmoud Abu-Allaban

The Hashemite University, Faculty of Natural Resources and Environment, Department of Water Management and Environment, Jordan

Received 29 April 2019, Accepted 12 September 2019

Abstract

The Jordanian Badia, which makes up almost 80% of the Jordanian territories, is becoming an important source for food production due to the rapid population growth and the large demand for food. Low precipitation slows down the production and decomposition of organic material, which leads to poor soils which lack basic elements that are necessary to maintain a lavish agriculture in the Badia. The composting of organic material is believed to be a good option to improve soil conditions in the Badia and to reduce the burdens on domestic landfills. However, composting may induce odors and air contaminants including NH_3, CH_4 and N_2O in the vicinity of composting premises. This paper is carried out in order to assess air quality under the impact of composing in the Jordanian Badia by applying the well-known AERMOD Model. It studies the dispersion of odors and other pollutants from a proposed composting facility to be located at the campus of The Hashemite University in Jordan. The selected location is a good representation of the Jordanian Badia due to similarities in the climate, soil type, and fragile ecosystems. The study reveals that the predicted concentrations of the contaminating gasses vary between 5.0-8.0 ppb, 1870-2110 ppb, and 110-170 ppb for H_2S, CH_4, and NH=, respectively. The calculated odor concentrations were found to be in the range of 110-250 Ou_E/m^3. The findings of this paper emphasize the importance of composting as a good practice to manage agricultural and domestic solid waste, and to produce valuable composts which are highly needed to improve the soil conditions in the Badia with minimal consequences on air quality. The vast area of the Badia offers a myriad of places far from sensitive receptors to establish compost facilities without causing any nuisance to the (Bedouins) nomads, the main inhabitants of the Badia.

Keywords: Aermod, Air quality, ammonia, composting, hydrogen sulfate, methane, odors.

1. Introduction

Air pollution continues to receive a great deal of interest worldwide due to its negative impacts on human health and welfare. Several studies reported significant correlations between air pollution and certain diseases including shortness of breath, sore throat, chest pain, nausea, asthma, bronchitis and lung cancer (Dockery and Pope, 1994,). Extreme effects of air pollution include high blood pressure and cardiovascular problems (Pope et al., 2002; Sanjay, 2008). Correlations between air pollution and increased morbidity and mortality rates were also reported (Laden et al., 2000; Pope et al., 1995). The World Health Organization states that 2.4 million people die each year from causes directly attributable to air pollution (WHO, 2007). Epidemiological studies suggest that more than 500,000 Americans die each year from a cardiopulmonary disease linked to breathing fine particles of polluted air (Marsh and Bernstein, 2008). Another study has shown a strong correlation between pneumonia-related deaths and air pollution from motor vehicles in the UK (Knox, 2008). In addition to its negative impacts on human health, air pollution is known to cause injuries to animals, forests and vegetation, and aquatic ecosystems. Its impacts on metals, structures, leather, rubber, and fabrics include cracks, soiling, deterioration, and erosion (Boubel et al., 1994).

The Jordan Badia is classified as a semiarid to arid steppe environment and falls within the arid climate zone (Dutton et al., 1998). Most of the Badia area is bare and lacks a vegetation cover (Cope and El-Eisawi, 1998; Dutton and Shahbaz, 1999). Land use in the Badia region is mainly restricted to agriculture (rained or irrigated), animal husbandry, and mining. These areas have also been important grazing lands for the local population over the years (Juneidi and Abu-Zanat, 1993).

Badia is facing severe soil deterioration and fragile natural resources due to climate change, overgrazing, and the impact of several waves of refugees to this region. There have been few studies to address these challenges. Al-Ayyash et al. (2012) studied the feasibility for storm water harvesting in the northern Badia for the purpose of using collected water in raising cattle. They have found that the estimated runoff that could be harvested varies between 0.2 Million Cubic Meters at Alaasra and 0.82 MCM at Al-Manareh, which indicates that these sites have a good potential for water harvesting to be utilized by local farmers and livestock owners.

Rawajfih et al. (2005) investigated soil samples collected at four different areas in the Azraq basin of the northern Badia, and reported that most of the studied soils contain considerable amounts of carbonates. This leads to an alkaline reaction of the soils with pH values mostly being above eight, resulting in low availability of certain nutrients such as phosphorus. The authors recommended the usage of organic-based composts to improve the physical and chemical characteristics of the Badia soils in order to achieve

* Corresponding author e-mail: mlaban@hu.edu.jo

a sustainable agricultural production. The use of compost can be beneficial to improve the organic matter status in the Badia. Composts are rich sources of nutrients with a high organic-matter content. The physical and chemical properties of the soils are improved by adding compost, which ultimately increases the crop yield (Hussain et al., 2001).

There are two main types of composting: Vermicomposting and aerobic composting. Vermicomposting is usually used to decompose food materials using a bevy of microorganisms, insects, etc. Vermicomposting uses red worms, fungi, bacteria, and other insects to break down the materials or to produce food for others. It requires a medium level of maintenance. Proper moisture and constant monitoring are needed to keep the compost healthy.

Aerobic compost is composting by treatment with air and bacteria. The microorganisms disseminating the organic waste, that is high in nitrogen, will create high temperatures, breaking it down quickly without any odors. This type of composting needs constant attention and care as the matter needs to be overturned at periodic intervals for air supply and to keep the temperature up. This type of composting works very well for large amounts of waste. Proper moisture and air circulation are needed to make sure that the compost does not dry up.

Anaerobic composting, is composting without the need of air. Herein, one has to make a pile of waste products and wait for several years for a compost to occur. This requires little or no maintenance; as slow moving bacteria inside the waste does not require air to break down. This type of compost is normally found in landfills. The compost matter decays creating a smell. That is the reason why most landfills create awful odors.

Composting has several air quality consequences; mainly odors and fugitive gasses including H_2S, NH_3, CH_4 and N_2O. Pagans et al. (2006) reported that the emissions of volatile organic compounds VOC from lab-scale composting of various organic wastes exhibit maximum emissions early in the composting process. Spencer and Alix (2006) recommended controlling the dust at compost facilities by maintaining sufficient moisture content because dust can be a fire hazard at the facility, and may clog drainage systems and give odor and BOD to the leachate. They argued that the optimal moisture during decomposition is 60-65%; if compost gets too dry, dust will be created. Goldstein and Goldstein (2005) showed that insufficient carbon and insufficient turning caused leachate and odor problems. Schlegelmilch et al. (2005) suggested that main odorous emissions from compost facilities occur during the movement of materials. They have recommended minimizing odors by avoiding anaerobic conditions such as the storage of feedstocks which can be odor-producing. Rosenfeld et al. (2004) suggest that chemicals responsible for odors include ammonia, methane, hydrogen sulfide, and sulfur dioxide. They found that aerated static pile composting reduced ammonia by (72%), and aeration followed by biofiltration, reduced odor by 98%. Prasad et al. (2004) presented a review of the data on bioaerosols from various compost studies, where a setback of 200 m is recommended since background concentrations are achieved within a few hundred meters. Heroux et al. (2004) argued that odors were significant within 500 m of the yard waste composting facility. In addition to odors and gasses, the composting facilities generate fugitive PM10 via several mechanisms including composting operations, screening and grinding operations, and vehicles transporting feed stock from the site and picking up compost for distribution.

Muller et al. (2004) measured microbial-generated odorous volatile organic compounds (MVOCs) in the vicinity of two enclosed facilities composting a mixture of plant waste and sewage sludge in Germany. MVOCs were not found in the background air, but were detected downwind. Terpenes were the dominant compounds, and were detected to a distance of 800 m (the farthest point measured) at 103 nanograms/m^3. Concentrations varied over three orders of magnitude in the eight sampling events. At one facility, the concentrations were higher at a greater distance, which is likely due to air circulation patterns.

Herr et al. (2004a) found that total bioaerosols (total bacteria, molds, and thermophilic actinomycetes) were found at >105 CFU/m^3 in the outdoor air in the vicinity of an outdoor composting facility, dropping to background concentrations within 550 m. They also reported an association between irritative respiratory symptoms and general health complaints and distance to the site. Herr et al. (2004b) measured total bacteria and molds in the air downwind from an outdoor composting site and noticed a drop to the near background within 300 m.

A physician-administered survey found airway symptoms in residents with the highest exposure (150-200 m downwind) compared to those further away (400-500m). An association was demonstrated between residential bioaerosol pollution and irritative airway complaints as well as excessive fatigue and shivering (Herr et al., 2004b). Bunger et al. (2006) found that exposure to organic dust at composting workplaces is associated with adverse acute and chronic respiratory health effects. They have reported high concentrations of fungi and actinomycetes. Compost workers report significantly higher prevalence of mucosal membrane irritation of eyes and upper airways as well as more conjunctivitis. Muller et al. (2006) reported that short-term exposure of healthy young subjects to organic dust at composting facilities had mild but measurable effects in eliciting acute systemic alterations.

This paper aims at studying the impact of composting on air quality at the Jordanian Badia by employing AERMOD to study the dispersion of odors and gasses released from the composting site. The findings of this paper provides comprehensive insight of how composting is impacting ambient air quality in the vicinity of the composting facilities. The investigations of this study would enable stockholders to take necessary precautions and mitigation measures that would prevent or minimize adverse consequences of envisioned large-scale composting on atmospheric environment at the Jordanian Badia.

2. Composting Technology

In order to make good compost, there are five main factors to be controlled during the process: nutrient balance, particle size, moisture content, oxygen flow, and temperature.

Maintaining a reasonable balance between green organic materials such as grass clippings, food scraps, and manure, which is rich in nitrogen; and brown organic materials that have a higher carbon content including dry leaves, wood chips, and branches is very important in order to get a fertile and sweet-smelling compost. Typically, carbon to nitrogen ration (C:N) has to be in the range of 25-30:1. A higher carbon content slows down decomposition, whereas a lower carbon content may lead to a stinky compost pile.

Microbial activity during early composting stages can raise the temperature at the core of the pile to above 60° C. High temperatures promote rapid composting and destroy pathogens and weed seeds. However, very high temperatures are not favored as they may kill microorganisms or constrain their activities. Therefore, a certain temperature range has to be maintained to ensure optimal microbial productivity. In addition to temperature, oxygen and moisture contents have to be controlled in order to sustain a healthy and productive microbial environment in the compost pile. Water facilitates the transport of substances within the pile and makes nutrients in the organic substances available for microbes. Aerating the compost speeds up the decomposition. It can easily be done by turning the pile or placing the pile on a series of pipes. However, too much oxygen can dry out the pile and hinder the composting process. Having a mixture of large and small particles is critical. Small particles improve the pile insulation to help maintain optimum temperatures and produce a more homogeneous compost mixture. They also increase the surface area on which the microorganisms can feed. However, any excess of tiny particles would obstruct aeration into the pile and lead to anaerobic conditions.

There are several composting techniques that are employed in different parts of the world depending on waste type and volume. Techniques include vermicomposting, in-vessel composting, and aerated static piles. Vermicomposting uses red worms in bins to feed on food scraps, yard trimmings, and other organic matter to create compost. In-vessel composting can process large amounts of waste without taking up a large space, and can accommodate virtually any type of organic waste including meat, animal manure, biosolids, and food scraps. This method involves feeding organic materials into a drum, silo, concrete-lined trench, or similar equipment. This allows for good control of the micro-environmental conditions such as temperature, moisture, and airflow. The material is aerated by mechanical turning.

The proposed composting facility will employ the aerated pile technique. It involves forming organic waste into rows of long piles and frequently turning the piles for aeration. The ideal pile height is between one to two meters with a width of four to five meters. The pile will be aerated by turning. Adding layers of loosely-piled bulking agents (e.g., wood chips, shredded newspaper) facilitates air percolation through the pile. This method produces compost within three to six months. It is suitable for a relatively homogenous mix of organic waste and works well for larger quantity-generators of yard trimmings and compostable domestic solid waste, which includes food scraps and paper products.

3. Compost Site

The Hashemite University (HU) is a Jordanian university which includes nineteen colleges that offer Bachelor and Master degrees in numerous disciplines including medicine, engineering, science, arts, education, etc. It spans over a vast campus (850 hectare) in a semi-arid region with a smooth terrain. The campus is located about 15 km to the east of Zarqa, the second mostly populous city in Jordan. It is bordered from the east by Zarqa-Free Zone (ZFZ). The compost site is proposed to be located at the North-Eastern portion of the campus (Figure 1). Wind mainly blows from West and North West, therefore odors and toxic gases emanated from the composting will be dispersed in empty arid land downwind from the composting site before entering into ZFZ.

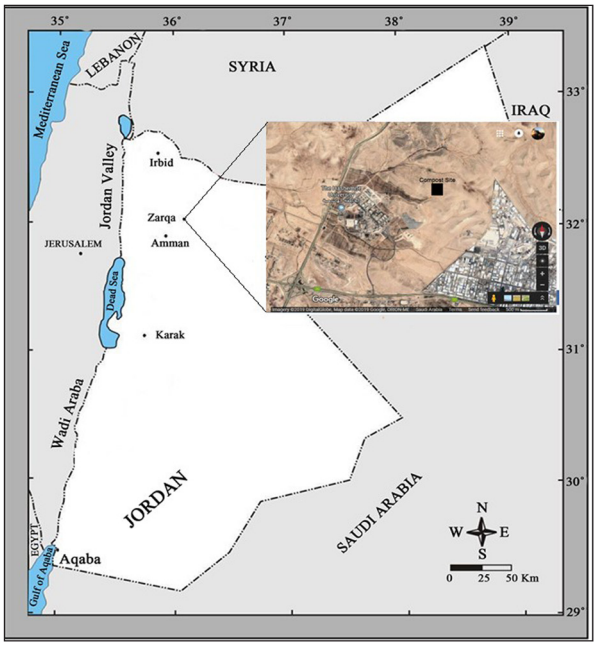

Figure 1. Study Area, modified after Abuqubu et al., 2016. Coordinates (32°06'24.7"N 36°11'59.3"E) and the satellite image is retrieved from www.google.com.

4. Environmental Baseline

Historical meteorological data were collected from an automated station during the years 2010 to 2014 (Table 1). Instruments were programmed to read and record weather parameters at five-minute intervals. Data were then downloaded and subjected to statistical treatment including checking for blanks and calculating monthly arithmetic means. Upper sounding is acquired from Almafraq weather station. It is evident that weather conditions at the site of the proposed facility are perfect for composting stages. Mild to warm air temperatures throughout the year speed up different thermophilic and maturation stages. Low numbers of precipitation days and accumulative annual precipitation provide a natural shelter against excess rain that would otherwise enhance the formation of anaerobic conditions, which lower the compost grade and enhance emissions of methane, hydrogen sulfide, and other odor agents. According to windrows (Figure 2), North-West Wind dominates the wind direction at the campus of The Hashemite University. Consequently, the compost facility, which is proposed to

be constructed at the North-Eastern sector of the campus, would have no impact on students or staff as odors will be transported away to the empty-desert spaces in the Eastern part of the campus.

Table 1. Meteorological data for The Hashemite University station over the period (2010-2014). Temperature is reported in (°C).

Parameter	Jan	Feb	Mar	Apr	May	Jun	Jul	Aug	Sep	Oct	Nov	Dec	Yearly
Mean Air Temperature (Max. +Min.) /2	6.5	6.8	9.3	15.0	19.3	21.7	23.5	23.7	22.1	18.6	13.3	8.5	15.7
Mean Max. air temperature	9.3	10.0	13.1	19.8	24.6	27.3	28.9	29.0	27.2	23.0	16.9	11.5	20.1
Mean Min. air temperature	3.6	3.6	5.2	10.1	14.0	16.2	18.1	18.3	17.0	14.2	9.6	5.6	11.3
Absolute Max. air temperature	23.0	22.8	24.8	32.6	36.7	37.0	38.3	39.5	36.8	33.4	29.0	24.5	39.5
Absolute Min. air temperature	-3.8	-6.6	-1.8	-2.2	4.5	6.4	11.3	13.5	11.6	7.0	-3.2	-3.2	-6.6
Mean wind speed (knot)	7.1	6.9	7.0	6.3	5.4	6.3	6.3	5.9	5.0	4.9	6.4	6.4	6.2
Max. wind speed (knot)	30.0	36.0	40.0	40.0	20.0	25.0	25.0	30.0	20.0	21.0	25.0	30.0	40.0
Daily mean Relative Humidity %	78.1	74.8	68.2	53.4	44.7	46.5	49.5	52.5	54.5	58.3	63.6	74.6	59.9
Mean sunshine hours	4.0	5.0	6.5	8.7	10.3	12.1	12.4	11.6	9.2	7.7	5.7	3.7	8.1
Total Rainfall amount (mm)	40.6	38.3	30.6	5.9	2.4	0.0	0.6	0.0	0.2	5.1	19.9	33.6	160.2
Mean no. of days with precipitation >= 1.0 mm	9.8	8.9	7.1	1.5	1.3	0.0	0.1	0.0	0.1	2.8	4.3	7.8	43.7

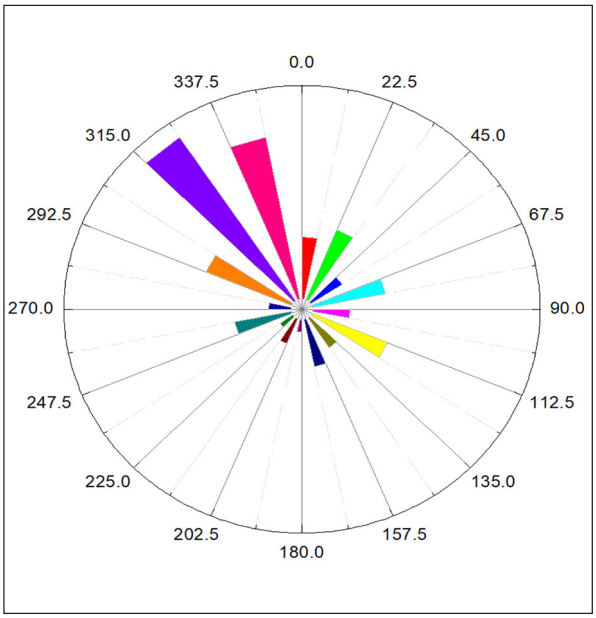

Figure 2. Windrows for The Hashemite University over the period from 2010 through 2014.

Ambient particulates and gaseous air pollutants (particulate Matter (PM), SOx, NOx, and CO) were monitored over the period from (12-14/8/2018) using the air quality monitoring station of The Hashemite University. They were found to be well below corresponding Jordanian standards of ambient air quality specified in JS-1140/2006 (Table 2). The monitoring station is equipped with analyzers (Thermo Environmental Instruments Inc.) which are capable of measuring sulfur dioxide (pulsed fluorescence method, model TEII 43C), nitrogen oxides (chemiluminescence, model TEII 42i), ozone (UV optical absorbance, model 49), and carbon monoxide (gas filter I.R. absorption, model 48i), in addition to air temperature, wind speed, wind direction, and relative humidity. The concentration of ambient Ammonia was also measured, and was found to be 76µg/m^3, which is below the Jordanian standard of 270 µg/m^3. Analyzers were programmed to record readings at five-minute intervals. The collected data were automatically and continuously downloaded into a companion PC. Analyzers were calibrated at the sampling site prior to starting the experiment in order to ensure proper functioning.

Table 2. Concentrations of particulates and gaseous air pollutants monitored at the proposed location of the composting facility

Date	TSP (µg/m^3)	PM10 (µg/m^3)	PM2.5 (µg/m^3)	CO (1-hr) (µg/m^3)	CO (8-hr) (µg/m^3)	NO_2 (1-hr) (µg/m^3)	NO_2 (Daily) (µg/m^3)	SO_2 (1-hr) (µg/m^3)	SO_2 (Daily) (µg/m^3)
2018/8/12	98.6	48.57	23.2	1.2	<1.0	35.19	35.9	20.5	16.9
2018/8/13	114.8	57.61	29.4	1.1	<1.0	34.048	34.81	38.5	36.7
2018/8/14	174.6	86.96	42.9	1.13	<1.0	32.74	31.36	32.72	31.36

5. Impact on Air Quality

The impact of composting on air quality was calculated by employing the AERMOD regulatory model, which is developed and maintained by The U. S. Environmental Protection Agency (EPA) in conjunction with the American Meteorological Society (AMS) (EPA-454/R-03-004).

Model Validity and Input

The prediction of impacts on air quality during the operation phase has been carried out using the AERMOD Regulatory Model which is based on the famous Gaussian Plume Dispersion. AERMODE has many important features which make it the preferred model for air-dispersion modeling studies worldwide.

Model Validity

The American Guideline on Air Quality Models (40 CFR Part 51, Appendix W, Federal Register, November 9, 2005) and the NYSDEC Guidelines on Air Dispersion Modeling Procedures for Air Quality Impact Analysis (DAR-10, May 9, 2006) recommend the use of AERMOD in air dispersion modeling studies for stationary industrial sources. It is developed by The U. S. Environmental Protection Agency (EPA), in conjunction with the American Meteorological Society (AMS). The model is capable of handling multiple sources, including point, volume, and area source types. Line sources may also be modeled as a string of volume sources or as elongated area sources. Several source groups may be specified in a single run, with the source contributions combined for each group. This is particularly useful for applications in which combined impacts may be needed for a subset of the modeled background sources that consume increment. The combined impacts from all background sources (and the permitted source) are needed to demonstrate compliance with the National Ambient Air Quality Standards (NAAQS). The model contains algorithms for modeling the effects of aerodynamic downwash due to nearby buildings on point source emissions. AERMOD does include algorithms for modeling depositional effects on particulate emissions. The AERMOD model has considerable flexibility in the specification of receptor locations. The user has the capability of specifying multiple receptor networks in a single run, and may also mix Cartesian grid receptor networks and polar grid receptor networks in the same run. This is useful for applications in which the user may need a coarse grid over the whole modeling domain, but a denser grid in the area of maximum expected impacts. There is also flexibility in specifying the location of the origin for polar receptors, other than the default origin at (0,0) in x,y, coordinates. For more information, refer to the model description document (EPA-454/R-03-004).

Modelling Input

Surface meteorology and upper sounding are prepared in format that can be read by AERMOD using AERMET, a companion model designed to handle meteorology. The two files in addition to emission rates are used by AERMOD in order to estimate concentrations of odor and other air contaminants at the earth surface in the vicinity of the proposed composting site. Emission rates of released odor, gasses, and particulate matter (PM10) are presented in Table 3. They are calculated based on published data. The composting site will contain ten windrows. Each row is 40m long, 4m wide, and 1.5m high. The entire composting would last for about one year: nine months for active phase and three months for curing phase. Total volume and surface area of windrows are calculated to be about 1200 m^3 and 2060 m^2, respectively (Figure 3). Compost density is assumed to be 600 kg/m^3 ; therefore, the total mass of the processed compost will be (density * volume) 720 ton/year.

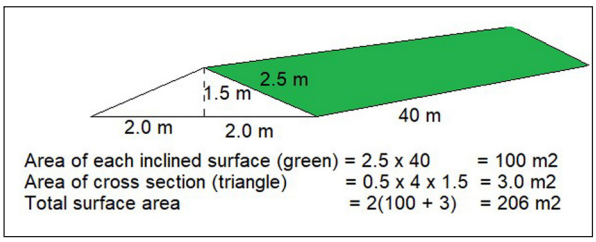

Figure 3. Calculating surface area of a compost windrow.

Table 3. Emission rates of odors and other air contaminants released from the proposed composting facility.

Contaminant	Reported Emission Rate	Converted Emission Rate	Source
PM10	3.03 3.03 ton/ year	0.67 **(g/s)**	USEPA, 2006
CH4	13.5 g/ m^2day	3.22E-01 **(g/s)**	Leytem et al., 2011
NH3	1.6 g/m^2day	3.81E-02 **(g/s)**	Leytem et al., 2011
N2O	0.9 g/ m^2day	2.15E-02 **(g/s)**	Leytem et al., 2011
H2S	0.08 g/ kg.day	1.8 E-03 (g/s)	Yuan et al., 2015
Odor	1.19 E+07 Ou_E/ton	2.72E+02 **(Ou_E/s)**	Capelli et al., 2014

6. Aermod Findings

The highest 24-hour and annual PM10 concentrations in the vicinity of The Hashemite University's proposed composting facility (HUPCF) is illustrated in Figure 4. The highest predicted concentration is expected to be slightly higher than 70 $\mu g/m^3$ within a "circular" area of radius 200m surrounding the HUPCF, which is well below the national standard for PM10 in ambient air (120 $\mu g/m^3$).

The impact of the HUPCF plant on the gaseous air pollutants including Hydrogen Sulfide (H2S), Methane (CH4), and Ammonia (NH3), are also estimated (Figures 5-8). It is clear that the concentrations of these gasses show relatively high values within the borders of the compost site and drop to background concentrations in less than 2000m downwind. The predicted concentrations of these gasses vary from 5.0 to 8.0 ppb, 1870 to 2110 ppb, and from110 to 170 ppb for H2S, CH4, and NH3, respectively.

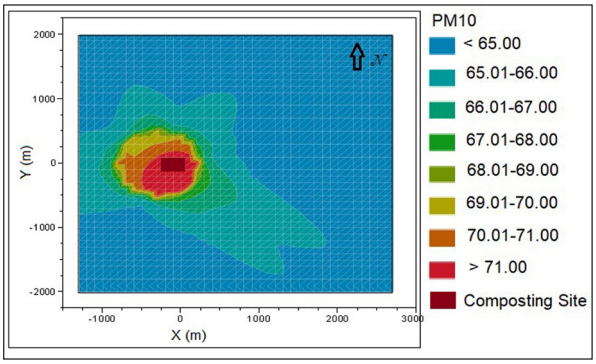

Figure 4. The highest 24-hour PM10 concentration in the vicinity of the HUPCF. The X-axis indicates a West-East direction.

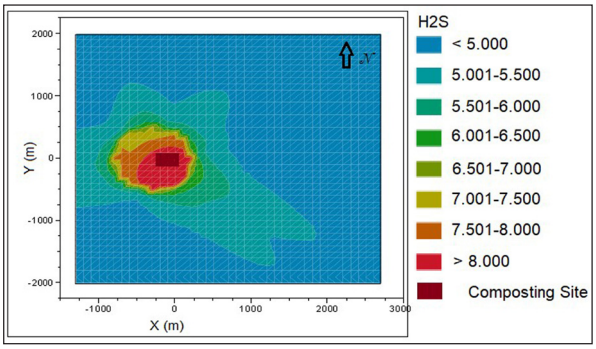

Figure 5. The highest 24-hour H2S concentration in the vicinity of the HUPCF. It is noted that the Jordanian 24-hour H2S standard of 10 ppb (JS-1140/2006) is attained.

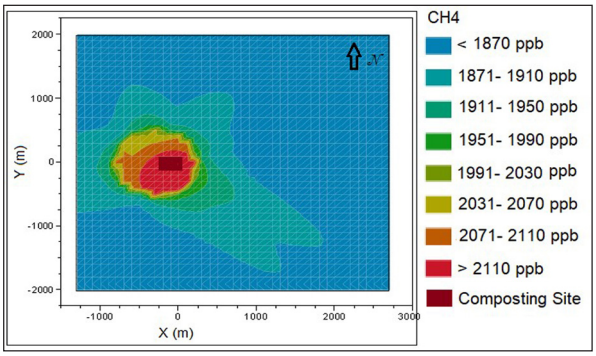

Figure 6. The highest 24-hour CH4 concentration in the vicinity of the HUPCF.

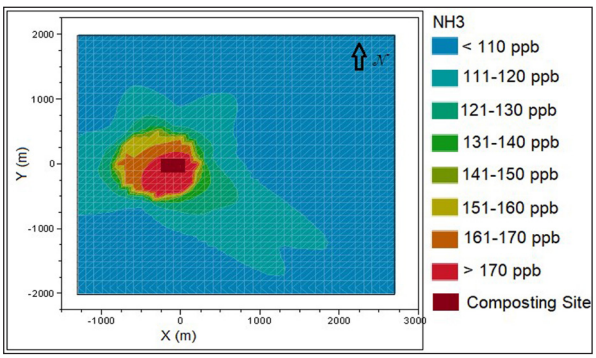

Figure 7. The highest 24-hour NH3 concentration in the vicinity of the HUPCF.

Odors

Odor concentration is expressed in terms of odor dilution ratio or odor units (Ou_E/m^3) per cubic meter of air (Ou_E/m^3), where the odor is no longer perceptible by 50% of the panelists. Odor is associated with odorant molecules, which imply that they cannot be physically or chemically measured. Therefore, their concentration is measured in odor unit per cubic meter (Ou_E/m^3).

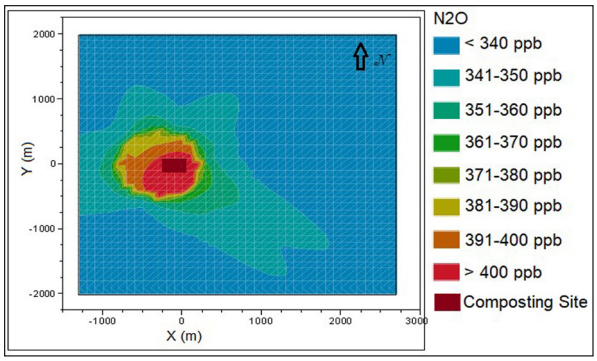

Figure 8. Highest 24-hour N2O concentration in the vicinity of HUPCF

The odor perception by humans is proportional to the instantaneous peak concentration of the odorant rather than to mean values (Latos et al., 2011). AERMOD, similar to other dispersion models, is set for the calculation of at least hourly mean concentrations. The sensation of odor, however, depends on the momentary (peak) odor concentration, but not on a mean value. In order to calculate the five-second average concentration, the hourly averaged concentrations predicted by AERMOD are first converted to three-minute average concentrations using the formula below (Duffee et al., 1991):

$$C_{3\ minute} = C_{30\ minute}\left(\frac{30\ minute}{3\ minute}\right)^{0.2} \quad \ldots\ldots\ldots\ldots\ldots (1)$$

The three-minute average concentration is converted to five-second average concentrations by multiplying by a factor of five (OME, 1996). The findings are illustrated in Figure 9. It is now evident that odor concentration could be slightly higher than 250 Ou_E/m^3 inside the borders of the composting site itself, but the concentration drops exponentially to less than 10 Ou_E/m^3 downwind the site.

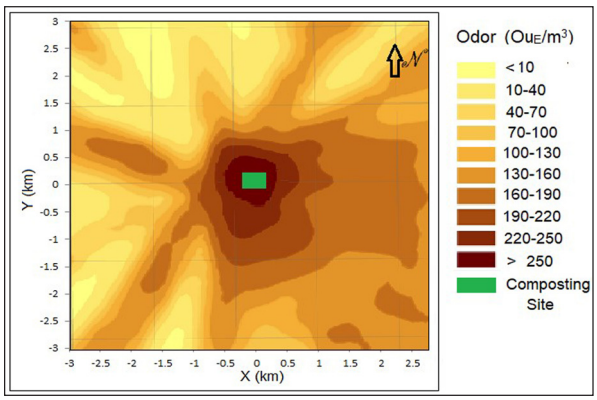

Figure 9. The highest five-second odor concentration (Ou_E/m^3) in the vicinity of the HUPCF.

7. Discussion

It can be seen that the odor dynamics are similar in almost all directions; the concentrations drop rapidly in the first 400 m and then they decrease slowly to values close to 10 Ou_E/m^3. The concentration towards the East direction presents very high values (open sheds). The area close to the composting site is in critical conditions, and odor can be perceived also at a significant downwind distance (more than 1.5 km). The impact on workers and staff is often assessed in terms of odor-

exposure duration per year. However, exposure time (day or night) is an important factor that needs be considered. The results showed that the unfavorable events happen often in the early morning because dilution is halted during the night due to the absence of natural convection. Nights undergoing thermal inversion are therefore expected to yield a poorer air quality with high levels of odors and other contaminants. In December and January, wind direction reverses; therefore, odors would be transported westward of the composting site toward the developed area of the university campus. Therefore, early-morning classes in the Eastern building would be subject to annoying odors. Consequently, the composting site has to be located at least 2000 m to the east of classrooms, and 2000 m to the west of ZFZ.

8. Conclusions

The compost site that is proposed to be established at the campus of The Hashemite University would have several advantages as it offers affordable and sound management for organic waste. Composting has many advantages compared with landfilling and incinerating. It does not require the allocation of vast land, nor does it release vast quantities of greenhouse gasses including carbon dioxide and methane. The final product will be distributed throughout the cultivated part of the campus. This is anticipated to improve soil texture and organic content.

The project will have minimal impacts on air quality (odors) in areas located downwind from the site, which is mainly composed of a barn semi-arid plateau. During the events of the night thermal inversion, odors may reach Zarqa Free Zone, but this should not be a problem because the Free Zone is active only during the daytime where convection is strong enough to dilute pollution by carrying air contaminants upward. Academic and administration buildings might be exposed to odors in the early morning during December and January. Most of these impacts are eliminated by simply placing the composting site at the southeastern part of the campus, where odors and gasses would be transported and dispersed in an empty land that does not have sensitive receptors.

Based on these findings, it is recommended to adopt composting as a sound environmental practice throughout the Badia region in Jordan. The final product is highly needed in the region because it is a natural soil conditioner that is rich in organics and other elements that are essential to enhance soil quality in the Badia, which is becoming a main area for growing vegetables and fruits as well as livestock fodder.

Acknowledgment

The author is grateful to The Hashemite University and the Deanship of Scientific Research for offering a fully-covered sabbatical leave for the academic year 2018/2019 in order to accomplish this research.

References

Abuqubu, J., Al Dwairi, R., Hadi, N., Merkel, B., Dunger, V., Laila, H. (2016) Geological and Engineering Properties of Granite Rocks from Aqaba Area, South Jordan. Geomaterials, 6, 18-27. doi: 10.4236/gm.2016.61002.

Al-Ayyash, S., Al-Adamat, R., Al-Amoush, H., Al-Meshan, O., Rawjefih, Z., Shdeifat, A., Al-Harahsheh, A, Al-Farajat, M. (2012). Runoff Estimation for Suggested Water Harvesting Sites in the Northern Jordanian Badia. Journal of Water Resource and Protection, 4: 127-132.

Boubel, R.W., Fox, D.L., Turner, D.B., Stern, A.C. (1994): Effects on Materials and Structures. Fundamentals of Air Pollution, 3rd ed. Academic Press, New York.

Bunger, J., Schappler-Scheele, B., Hilgers, R., Hallier, E. (2006). A 5-Year Follow-Up Study on Respiratory Disorders and Lung Function in Workers Exposed to Organic Dust from Composting Plants. International Archives of Occupational and Environmental Health. Online: http://www.springerlink.com/content/82u23r2371414873/fulltext.pdf

Capelli, L., Sironi, S., Del Rosso, R. (2014). Odor emission factors: fundamental tools for air quality management, Chemical Engineering Transactions, 40, 193-198. DOI: 10.3303/CET1440033

Cope, T.A., and Eisawi, D. (1998). Checklist of the flora. In: Dutton, R.W., Clarke, J.I. and Battikhi, A.M. Arid Land Resources and Their Management: Jordan's Desert Margin, pp. 183 – 188. Kegan Paul International: London, pp. 332.

Dockery, D.W., and Pope, C.A. (1994). Acute respiratory effects of particulate air pollution. Annual Revision Public Health, 15: 107–132.

Duffee, R.A., O'Brien, M.A., Ostojic, N. (1991). Odor Modeling: Why and How, Transactions -Air & Waste Management Association, Pittsburgh, Pennsylvania, 1991. In recent Developments and Current Practices in Odour Regulations, Control and Technology. Edited by D.R. Derenzo and A. Gnyp.

Dutton, R., and Shahbaz, M. (1999). The Badia program: defining and overcoming constraints on sustainable development. Applied Geography, 19,275–281.

Dutton, R.W., Clarke, J.I., Battikhi, A.M. (1998). Arid Land Resources and Their Management: Jordan's Desert Margin. Kegan Paul International, London, pp. 332.

Goldstein, J., and Goldstein, N. (2005). Controlling Odors at Composting Facilities. BioCycle, 46(5):22.

Heroux, M., Page, T., Gelinas, C., Guy, C. (2004). Evaluating Odor Impacts from a Landfilling and Composting Site: Involving Citizens in the Monitoring. Water Science and Technology, 50(4):131-137.

Herr, C.E. zurNieden, W.A., Stilianakis, N.I., Eikmann, T.F. (2004b). Health Effects Associated with Exposure to Residential Organic Dust. American Journal of Industrial Medicine. 46:381-385.

Herr, C.E., Zur Nieden, W.A., Seitz, H., Harpel, S., Stinner, D., Stilianakis, N.I., Eikmann, T.F. (2004a). Bioaerosols in Outdoor air - Statement of Environmental Medical Assessment Criteria on the Basis of an Epidemiological Cross Sectional Study. GefahrstoffeReinhaltung Der Luft., 64(4):143-152.

Hussain, N., Hassan, G., Arshadullah, M., Mujeeb, F. (2001). Evaluation of amendments for the improvement of physical properties of sodic soil. Intl. J. Agric. Bio., 3:319-322.

Juneidi, M., and Abu-Zanat, M. (1993). Jordan's Agricultural Review and Policy Implementation Plan Low Precipitation Zone. Ministry of Agriculture, Amman, pp. 98.

Knox, G. (2008). Atmospheric pollutants and mortalities in English local authority areas. J. Epidemiol Community Health 2008, 62:442-447. doi:10.1136/jech.2007.065862.

Laden, F., Neas, L.M., Dockery, D.W., Schwartz1, J. (2000). Association of Fine Particulate Matter from Different Sources with Daily Mortality in Six U.S. Cities. Environ Health Perspect 108: 941–947. http://ehpnet1.niehs.nih.gov/docs/2000/108p941-947laden/abstract.html.

Latos, M., Karageorgos, P., Kalogerakis, N., Lazaridis, M. (2011). Dispersion of odorous compounds emitted from

wastewater treatment plants. Journal of Water Air and Soil Pollution, 215(1): 667-677. DOI: 10.1007/s11270-010-0508-8

Leytem, A.B., Dungan, R.S., Bjorneberg, D.L., Koehn, A. (2011). Emissions of Ammonia, Methane, Carbon Dioxide and Nitrous Oxide from Dairy Cattle Housing and Manure Management Systems. September 2011, Journal of Environmental Quality, 40(5): 1383-94. DOI: 10.2134/jeq2009.0515

Marsh, C., and Bernstein, M. (2008). Newly detected air pollutant mimics damaging effects of cigarette smoke. American Chemical Society. http://www.eurekalert.org/pub_releases/2008-08/acs-nda072308.php. Retrieved Feb.17, 2011.

Muller, T., Jorres, R.A., Scharrer, E.M., Hessel, H., Nowak, D., Radon, K. (2006). Acute Blood Neutrophilia Induced by Short-Term Compost Dust Exposure in Previously Unexposed Healthy Individuals. International Archives of Occupational and Environmental Health, 79: 477-482.

Muller, T., Thissen, R., Braun, S., Dott, W., Fischer, G. (2004). (M)VOC and Composting Facilities. Part 2: (M)VOC Dispersal in the Environment. Environmental Science and Pollution Research – International, 11(3): 152-157.

Ontario Ministry of Environment (OME) (1996). Odor Impacts - An Overview. Science and Technology Branch, Environmental Engineering Services, STB Technical Bulletin No. EES-1, February 1996.

Pagans, E., Font, X., Sanchez, A. (2006). Emission of Volatile Organic Compounds from Composting of Different Solid Wastes: Abatement by Biofiltration. Journal of Hazardous Materials, 131: 179-186.

Pope, C., Arden, Burnett, R.T., Thun, M.J., Calle, E.E., Krewski, D., Ito, K., Thurston, G.D. (2002). Lung Cancer, Cardiopulmonary Mortality, and Long-term Exposure to Fine Particulate Air Pollution. Journal of American Medical Association, 287(9): 1132-1141.

Pope, C.A., Thun, M.J., Namboodira, M., Dockery, D.W., Evans, J.S., Speizer, F.E., Health Jr., C.W. (1995). Particulate air pollution as a predictor of mortality in a prospective study of US adults. American Journal of Respiratory Critical Care Medicine, 151: 669–674.

Prasad, M., van der Werf, P., Brinkmann, A. (2004). Bioaerosols and Composting – A Literature Evaluation. Composting Association of Ireland TEO.

Rawajfih, Z., Khresat, S.A., Buck, B. (2005). Arid soils of the Badia region of northeastern Jordan: Potential use for sustainable agriculture. Archives of Agronomy and Soil Science, 51(1): 25-32.

Rosenfeld, P., Grey, M., Sellew, P. (2004). Measurement of Biosolids Compost Odor Emissions From a Windrow, Static Pile, and Biofilter. Water Environment Research, 76(4): 310-315.

Sanjay, R., (2008). "Exposure to Bad Air Raises Blood Pressure", Study Shows. Science Daily, Ohio State University.

Schlegelmilch, M., Streese, J., Biedermann, W., Herold, T., Stegmann, R. (2005). Odor Control at Biowaste Composting Facilities. Waste Management, 25: 917-927.

Spencer, R., and Alix, C.M. (2006). Dust Management, Mitigation at Composting Facilities. BioCycle, 47(3): 55.

USEPA AP-42: Compilation of Air Pollutant Emission Factors Section 13.2.4 Aggregate Handling and Storage Piles Table 13.2.4-1 November (2006). United States Environmental Protection Agency. https://www3.epa.gov/ttnchie1/ap42/ch13/final/c13s0204.pdf

World Health Organization (2007). Estimated deaths & DALYs attributable to selected environmental risk factors, by WHO Member State, 2002. Department of Public Health and Environment, January 2007.

Yuan J, Yang Q, Zhang Z, Li G, Luo W, Zhang D. Use of additive and pretreatment to control odors in municipal kitchen waste during aerobic composting. J Environ Sci 2015;37:83–90. http://dx.doi.org/10.1016/j.jes.2015.03.028

JJEES

JJEES (2020) 11 (1): 26-37
ISSN 1995-6681

Jordan Journal of Earth and Environmental Sciences

Model Simulations of Local Meteorological Conditions in the Vicinity of a Hypothetical Nuclear Power Plant in Jordan

Marwan M. Al-Kloub[1, 2], Alexander Mahura[3], Alexander Baklanov[4,5], Nahid Atashi[3,6], Tareq Hussein[1,3 *]

[1]The University of Jordan, School of Science, Department of Physics, Jordan
[2]Prince Faisal Technical College, Department of Physics, Jordan
[3]University of Helsinki (UHEL), Faculty of Science, Institute for Atmospheric and Earth System Research (INAR/Physics), Finland
[4]World Meteorological Organization (WMO), Switzerland
[5]University of Copenhagen (UCPH), Niels Bohr Institute (NBI), Denmark
[6]University of Isfahn, Faculty of Geographical science and Planning, Iran

Received 22 June 2019, Accepted 6 October 2019

Abstract

As a solution for the increasing energy demand in Jordan, nuclear power was recommended for the energy mix at the national level. However, investigations of the meteorological conditions and mass transfer have never been conducted and reported earlier based on typical Jordanian conditions in order to have prior knowledge in case of a future hypothetical nuclear accident in Jordan. In this study, the variabilities of horizontal and vertical wind components and surface temperature differences have been investigated near one of the originally suggested locations for the construction of a nuclear power plant facility. That proposed location is the site of the Samra Energy Power Plant (SEPP). The selected domain of the simulation model was 85×85 km^2 in area (17×17 grid points and 13 vertical layers) surrounding the SEPP site. The simulations revealed that the wind direction near the surface was developed to comply with the complexity of the terrain regardless of the input values of the prevailing wind direction. The wind direction propagated along the valleys that are surrounded by the dominating mountains. The surface wind speed was proportional to the input value of the wind speed as well as to the slope of the surrounding terrain. Quantitatively, the developed surface wind speed was 0.5–2.1 m/s in January compared with 1.0–4.3 m/s in July. The vertical component of wind velocity was the lowest (nearly zero in January versus ~0.1 m/s in July) near the surface. In practice, the main outcome of this investigation can serve as a base-block for considering other possible geographical locations for the construction of a nuclear power plant in Jordan and for case studies intended to assess possible consequences in case of accidental releases and other potential accidents of possible nuclear, chemical, industrial danger.

Keywords: meteorological modeling, nuclear power plant, horizontal and vertical components of wind speed, surface temperature difference

1. Introduction

In general, it is difficult and rather complex to make a correct and clear decision in a dangerous situation, especially at the initial stages, based on the availability of exhaustive information that might be delayed to reach the hands of decision-makers. Therefore, it is wise to make preliminary estimations on the basis of information prepared beforehand regarding a hypothetical nuclear accident and its possible consequences. On the whole, nuclear power plant (NPP) accidents involve emissions of radioactive pollutants into the environment and their transport in the atmosphere covering large geographical regions. Although nuclear safety at NPPs is very strict and tight that accidents are less probable to happen; however, such events were recorded several times in the past. According to the International Nuclear Event Scale (INES; levels 1-7), two accidents of the highest level (7) were reported in the past, namely Chernobyl, Ukraine in 1986 and Fukushima Daiichi, Japan in 2011.

For the purpose of securing prior knowledge for the sake of making a clear decision during nuclear accidents, mathematical models can be utilized to simulate the physical and dynamical processes of radionuclides' atmospheric transport, dispersion, removal, and deposition (e.g. Cao et al., 20016; Mitrakos et al., 2016; Lauritzen et al., 2007; Baklanov, 2003; Mahura et al., 1999; Baklanov et al., 1994). This can help understand and forecast the transport of radioactive emissions from potential sources that play a considerable role in the preparation of valuable data for decision-making processes. From a large diversity of factors, influenced by the environmental consequences of accident situations, the considerable part of the preparation of data is more influenced by local peculiarities and regional conditions. These conditions include: location of accident source, geographic peculiarities of local terrains; climatic conditions; density and quantity of the population; character and types of urban settlements, etc. As a matter of fact, creating centers for ecological monitoring and forecasting accidental consequences are especially important at both the local and regional levels.

After being emitted into the atmosphere, radioactive pollution clouds undergo additional changes such as: advection, turbulence, radioactive decay, dry and wet

* Corresponding author e-mail: t.hussein@ju.edu.jo

deposition, etc. (e.g. Matsuda et al., 2017; Evangeliou et al., 2016; Mészáros et al., 2012; Momoshima and Bondietti, 1994). Many models, describing the distribution of radioactive emissions from NPPs, have been developed and applied worldwide (e.g. Christoudias el al., 2014; Kawamura et al., 2014; Mazur et al., 2014; Baklanov et al., 2008a and 2008b; Mahura et al., 2005; Srinivas and Venkatesan, 2005; Baklanov and Mahura, 2001; Glyshenko el al., 1981; Davydova el al., 1990; AGROS). The Gaussian models require a minimum of input data; and hence, these are simple to simulate the distribution and transport of emissions. However, such models are not fully realistic, because they assume a homogeneous vertical distribution of pollution, whereas, in reality, the normal distribution law does not always occur. Besides, the wind velocity measurement is usually sparse and sometimes the trajectory of radioactive cloud is represented by a straight line. This limits the application of this model to an approximate distance between 10 and 15 km. Therefore, a more detailed description of emissions' distribution from NPP requires the application of higher order models, through which it is necessary to take into account temporal and spatial wind velocity components' changes. Such models require information about the velocity at several points (e.g. observation stations). The complex three-dimensional (3D) models, which are based on 3D wind fields, are capable of taking into account the influence of the surrounding terrain, roughness of the surface, wind change, atmospheric stability, etc. Such models are also embedded with the Atmospheric Boundary Layer (ABL) models in order to have better simulation results for the vertical and spatial structure of the wind field and turbulence. Typically, the effective source height of pollution, the increase of initial concentration at different stages of the accidental release, changes in concentration due to processes of the radioactive decay, wet and dry deposition removal of radionuclides from the atmosphere are also taken into account under the simulation of the distribution of emissions.

In 2001, Jordan started working on its own national nuclear power programme by establishing the Jordan Nuclear Energy Commission (JNEC). In 2007, the JNEC was replaced by the Jordan Nuclear Regulatory Commission (JNRC), and in 2008, it was replaced by the Jordan Atomic Energy Commission (JAEC). The JNRC works in coordination with relevant organizations to regulate and monitor nuclear energy, to protect the environment from radioactive hazards and related pollution, and to ensure the requirements for radiation safety, protection, and security. The JNRC also works closely with the International Atomic Energy Agency (IAEA) to apply nuclear safety standards in Jordan. The main objective of the JAEC has been to promote and develop a peaceful utilization of atomic energy to produce electricity and desalinate water.

The Jordanian nuclear programme also includes a research nuclear power plant, which has been established on the campus of the Jordan University of Science and Technology with a capacity of 5-10 MWatt (MW). The main purpose of this research plant is to conduct scientific research in medical, agricultural, and health sciences and services. Jordan also accommodates the International Centre for Synchrotron-Light for Experimental Science Applications in the Middle East (SESAME), which is ought to be the first major international research center in the Middle East with collaboration between the JAEC and the United Nations Educational, Scientific and Cultural Organization (UNESCO).

Originally, Jordan aimed to have two 1000 MW water-water energetic reactor units (VVER-1000) in operation by 2025, but is now reconsidering the use of smaller modular reactors instead. The exact locations of NPP's units have been under continuous consideration and analysis. One of originally suggested locations was near the Samra Electric Power Plant (SEPP) located in the northeastern part of Jordan.

The main objectives of this study are to simulate and investigate the meteorological conditions over the domain (85×85 km^2) centering around the SEPP site. It should be noted that this kind of investigation regarding the Jordanian conditions has never been made or published before. In practice, the study presented in this manuscript may serve as a base-block to consider other possible geographical locations in Jordan and to conduct case studies for the assessment of other potential objects that pose possible nuclear, chemical, and industrial threats.

2. Three-dimensional meso-meteorological model

2.1 Model description

This study utilizes a modified version of the Model Package (MP) named after the Institute of the Northern Environmental Problems (INEP), developed for the Simulation of Meteorological Fields (METEO) and Distribution of Pollution within the Atmospheric Boundary Layer (TRANS). This MP includes a three-dimensional (3D) modeling system that describes atmospheric dynamics and radioactive pollution within a modeling domain near a nuclear power plant. It consists of two main parts (e.g. Baklanov et al., 1994) as follows:

(1) METEO: a numerical meso-meteorological model over a complex terrain around a nuclear power plant to simulate the 3D meteorological fields

(2) TRANS: an Eulerian transport model to simulate the 3D atmospheric transport, diffusion, and deposition of a variety of radioactive pollutants over the terrain due to a hypothetical accident at the selected nuclear power plant as well as to calculate doses due to inhalation from the passing radioactive clouds and from the surfaces of different human organs of different population groups.

The MP was developed by a team of the researchers from INEP of the Kola Science Center, Russian Academy of Science. It was utilized for various case-studies (e.g. Baklanov et al., 1994; Baklanov et al., 2000; Baklanov et al., 2002). In this particular study, the MP was modified and prepared to accommodate for the typical Jordanian conditions of the complex terrain and to simulate the meteorological fields within the boundaries of the selected domain (within a 85×85 km^2 zone around a hypothetical NPP in the northeastern part of Jordan). This paper is focused on running the first part of the MP package (METEO - i.e. the meteorological fields' simulation). Although the MP second part (TRANS - i.e. distribution and atmospheric transport

of radioactive pollution and calculation of doses) is also of great interest in this regard, it will be presented in details in another paper in the nearest future.

The METEO model can be extended from a very local scale to larger scales. The concept of the 3D wind field is typically used in the most complex 3D models, so it is possible to take into account the influence of the terrain, roughness, wind characteristics, atmospheric stability, and other factors.

The numerical simulation of atmospheric pollution transport processes and diffusion consists of model realizations of pollution distribution (e.g. TRANS) based on the determination of both the u,v,w - components of wind field U, and coefficients of turbulent diffusion K along x,y,z-directions. The wind fields can be determined by a combined objective analysis of meteorological data obtained from a meteorological measurement network and mathematical modeling of the hydrothermodynamical characteristics of the atmospheric boundary layer. Even without an existing meteorological measurement network, the fields can be determined by means of modeling only. However, validation is still required against ground-based measurements. The details of the TRANS model description are explained by e.g. Baklanov et al. (1994).

The main components of the METEO-part are: (1) equations to describe the atmospheric processes, (2) a system of equations to describe the atmospheric surface layer in small–angle cases of a terrain, (3) boundary and initial conditions, and (4) determination of surface temperature by using actual measurements or by utilizing radiation and the heat balance equation of an orographic non-homogeneous surface. The use of special methods in the solution of model equations, including the system of coordinates with reducing height and the method of fictitious domains, allows for the simulation of the dynamics of the atmosphere over an arbitrary terrain.

2.2 Model input and output

The METEO model requires a set of input variables (see Tables 1–3). These include parameters related to the terrain and its contents (location of the nuclear power plant (thereafter, the plant) and water surfaces in the selected model domain), characteristics and operation mode of the plant, temporal parameters related to the occurrence of a hypothetical accident, a series of meteorological parameters and numerical parameters. The output of the METEO simulations includes 3D arrays that describe (in y-latitude, x-longitude, and z-altitude directions) the wind and turbulence fields as well as the temperature difference within the terrain at selected time-steps after the occurrence of a hypothetical accident.

The terrain parameters consist of a relief for the local terrain in the selected model domain, which is a 2D array that contains the height of a point above the sea level (a.s.l.). This digital map is scaled down or up when it is needed, so that the vertical structure of the model covers most of the boundary layer above the terrain. Other terrain-related parameters are locations and altitudes of water surfaces and the plant in the domain. The temporal parameters of the accident include time (hour and minute) and date (year, month, and day) of the accident's starting time. The numerical parameters include: a 3D grid description (number of grid points in the three x, y, z-directions), simulation time-step [s], continuity of time-step [s], number of steps and duration of step for iteration procedures, and a number of steps and intervals at which to write/save the results to the output files.

The meteorological parameters describe the conditions within the terrain at the location of the source (i.e. the plant). These include: wind direction and speed [in degrees from north and m s^{-1}, respectively], ambient air temperature [^{o}C], relative humidity [in %], intensity and quantity of precipitation [in mm/h and mm]. Such parameters are additionally required to be collected (of course, if available for as many locations as possible from a nearby meteorological network of measurements). Other meteorological background variables include: air temperature gradient [^{o}C], Coriolis parameters [s^{-1}], buoyancy parameters, 3D coefficient of turbulence, lambda constant, air density [kg m^{-3}], vertical wind profile description, surface temperature initial condition, as well as the temperature difference between land surface and air, between water surface and air, and between "hot" water surface (e.g. water used for cooling NPP and released into a nearby water object) and air.

3. Case studies

In this study, a series of the METEO model simulations have been performed for the location of the hypothetical NPP (which coincides with the SEPP location as one of previously and originally suggested locations to construct the Jordanian NPP) and its surrounding domain (Figure 1). The METEO model simulations were performed on a monthly basis taking into account the dominating average meteorological conditions (based on a statistical analysis of the available climatological data; see Table 3).

3.1 Site location and surrounding terrain

Although the exact location of the planned NPP in Jordan has not been certain yet, the model simulations have been made to investigate the Jordanian conditions and extend this exercise to other suggested locations in the future. The Samra EPP is located in the northeastern part of Jordan (32.1443 °N, 36.1428 °E) at an altitude of ~560 m (see Figure 1c). It is about 30 km to the north-east of Amman (the Jordanian capital city) and about 10 km to the north-east of Zarqa (Figure 1b). These two cities accommodate most of the Jordanian population (that is ~10 million inhabitants, www.worldmeters.info, 2019).

For this study, a model domain (size of 85×85 km^2) has been selected and at the center of which the NPP plant is placed (Figure 1d). It should be noted that the original terrain topography (Figure 1c) is very complex with about ~110 m a.s.l. at the south-west (near the Jordan Valley) and three mountains to north-west, south-west, and north-east with heights of about ~1240 m, ~1050 m, and ~1100 m, respectively. The terrain has a valley along the east-west line between the aforementioned mountains. This valley divides the terrain into rather equal halves, and it is nearly 10 km wide at the eastern side (height ~550 m) of the terrain, but becomes very narrow (less than 4 km wide) and deeper (down to heights of even ~10 m) at the western side of the domain. There are also small-size water reserves, which are located close to the power plant.

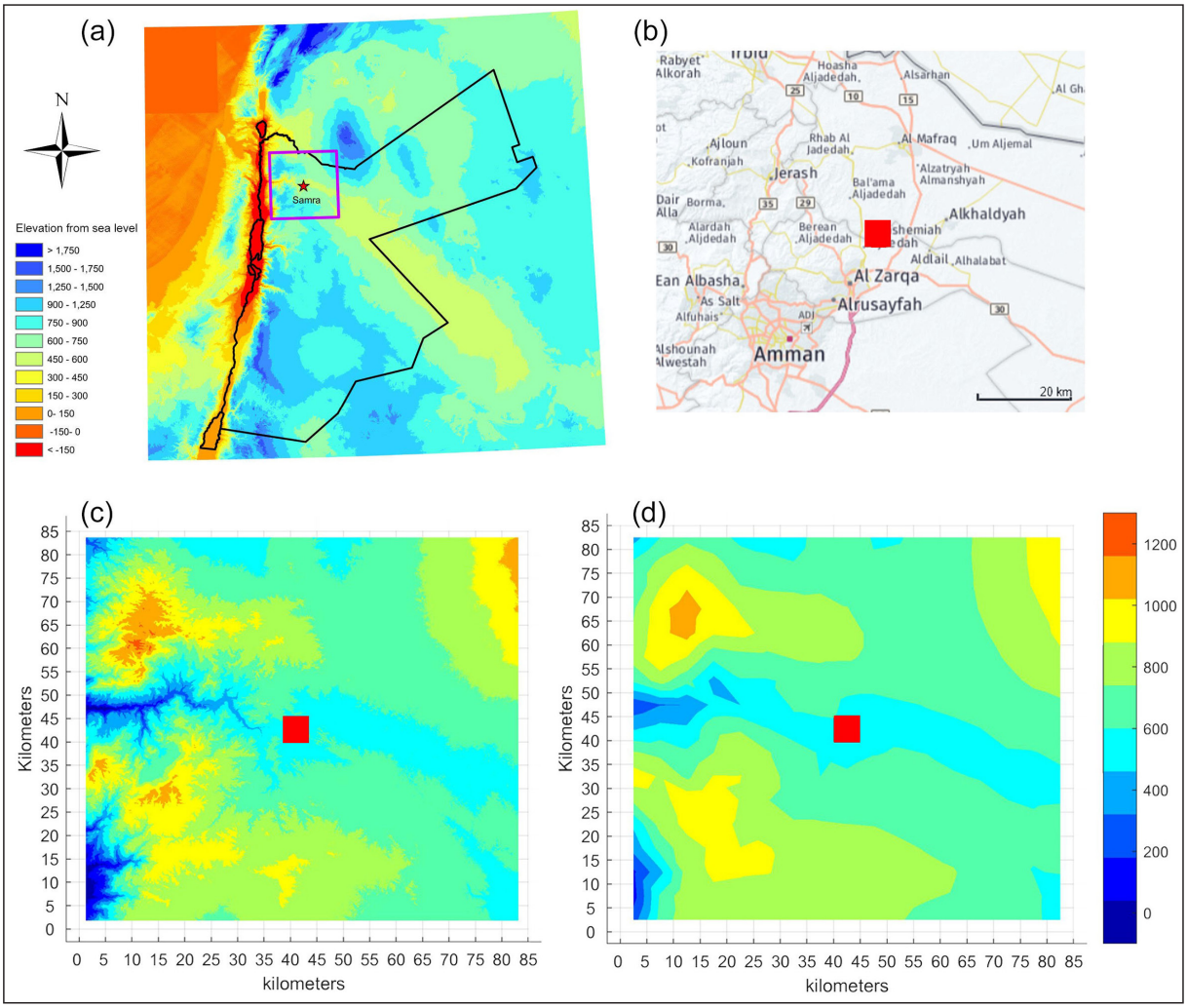

Figure 1. (a) Jordan map showing elevation above sea level and the domain (red square corresponding to 85×85 km^2), which is also shown from three different prospective: **(b)** land use, **(c)** detailed map of elevation above sea level, and **(d)** converted elevation map as 17×17 grid. The location of the hypothetical Jordanian nuclear power plant (hJNPP) is marked by a red square in the middle of the domain.

The original digital map of the terrain (Figure 1c) was transformed by interpolating into a 17×17 grid domain with a 5000 m horizontal resolution (Figure 1d). It was used as an input pre-defined terrain data for the METEO model simulations. The power plant and the nearby water surfaces lied within the same grid cell, which was located at ~560 m a. s. l. For practical purposes, the whole pre-defined terrain was "lowered down" by 200 meters, and hence, the original heights of locations of NPP and water surfaces were shifted down to 358 m in the model domain. This was done in order to accommodate more vertical levels in the atmosphere for better representation of hypothetical emissions by vertical layers. In total, there are thirteen vertical levels covering a 1300 m depth layer. Here, the depth of each sub-layer is as follows: 50 m – for 1-5th layers, 75 m – 6th, 100 m – 7th, 125 m – 8th, 150 m – 9-13th layers. Table 1 lists the details of the inputs related to the terrain, domain, and model simulation parameters.

3.2 Meteorological conditions

The meteorological parameters which are required as inputs for the METEO model simulation are listed in Table 2. The main meteorological parameters (wind speed and direction, ambient air temperature, relative humidity, and hourly and daily precipitation) were obtained from continuous measurements at the selected weather station. The year 2017 was considered as the most typical year in a series of observations starting with 2015 at the campus of the University of Jordan (32.0160 °N, 35.8695 °E). The statistics of monthly (from January until December) variabilities of these meteorological parameters are summarized in Table 3 (Hussein et al., 2018). The monthly mean ambient air temperature varied between +7 and +26.5 °C (the coldest in January and the warmest in July). The monthly mean relative humidity was inversely proportional to the temperature, and it was within the range of 38–78% (the highest in January and the lowest in July). The wettest month was February (daily mean precipitation of 5.52 mm/day; with the highest hourly rainfall being 0.23 mm/h and the driest months being May-June-July and September with no precipitation observed. Based on the monthly analysis of the wind characteristics, the prevailing wind direction varied from SE (~145°, November) to NW (~321°, September). In particular, the winds from the north-western sector dominated over the period from April to October, the winds from the south-eastern sector prevailed from November to December, and winds from the south-western sector dominated from January to March. The magnitude of the wind speed was in the range of 1–1.9 m/s (the highest in July and the lowest in October). Lower wind speeds were observed during the period from October to December, and the period for higher wind speeds was from June to August.

Table 1. Geographical properties of the model simulation and their numerical input parameters

	Parameter	Note	Assigned value
Terrain	Relief for local terrain	XY grid points	85×85 km^2 on a 17×17 grid Figure 2
	Relief grid resolution	arbitrary	5000 meters for 85×85 km^2
	Geographical locations of: - nuclear power plant - water surfaces	assigned to a certain cell in the terrain	nuclear power plant at the middle of the terrain (i.e. cell (9,9) water surfaces were assigned to closest cells
	Altitude of: - nuclear power plant - water surfaces	assigned after scaling up/down the terrain	on the downward scaled (85×85 km^2) domain, nuclear power plant at 358 m and water surfaces 358 m
Numerical	3D grid-points	arbitrary	17×17 (85×85 km^2); Figure 2
	Simulation time	arbitrary	180 minutes
	Continuity of time step	arbitrary	60 s
	XY grid steps	identical for X and Y	5000 m for 85×85 km^2
	Vertical profile	13 layers	1300 meters vertical profile: layers 1-5: 50 m layer 6: 75 m layer 7: 100 m layer 8: 125 m layers 9-13: 150 m
	Time step iteration	arbitrary	10 seconds
	Output steps	arbitrary	every 10 minutes

Table 2. Model input that describe the meteorological conditions.

	Parameter	Note	Assigned value
Meteorological	Wind direction	North à 0^o (clock-wise)	Table 3
	Wind speed	$WS = \sqrt{(U^2 + V^2)}$ U and V are horizontal components	Table 3
	Ambient temperature	Measured at 2 meters	Table 3
	Relative humidity	Measured at 2 meters	Table 3
	Intensity of precipitation	Measured	Table 3
	Quantity of precipitation	Measured	Table 3
	Temperature gradient	Temperature vertical gradient (dry vs humid atmosphere)	dry adiabatic condition (0.01 ^{o}C/m)
	Coriolis parameters	$f = 2\Omega sin\varphi$ φ is the latitude $\Omega = 2\pi/T$ is the Earth's rotation rate (7.2921×10^{-5} rad/s and T = 23 hr 56 m 4.1 s)	For the altitude at Samra Electric Power Plant $f = 7.71\times10^{-5}$ s^{-1}
	Buoyancy parameter	0.003 – 0.01	0.003
	3D turbulence coefficient	Coefficients of turbulent diffusion assigned depending on horizontal vs vertical resolution	XY plane (5000) and Z direction (50)
	Lambda constant	Constant for turbulence modeling to calculate fluxes	0.035
	Air density	ideal gas law	1.18 kg/m^3
	Vertical wind profile	1- Linearly increasing with height within first 4 layers of the domain (up to 200 m). Above that, a steady-state profile is assumed 2- Exponentially increasing with height within the first 8 levels (up to 550m). Above that, a steady-state profile is assumed 3- Exponentially increasing with height within the first 4 levels (up to 200m). Above that, a steady-state profile is assumed	We selected the second option
	Surface temperature initial condition	*1- PSI*(i,j) = 0 whole domain 2- Assumes temperature difference: land surface and air ($T_{land} - T_a$) water surf and air ($T_{water} - T_a$) hot-water and air ($T_{hot\text{-}water} - T_a$)	We selected the second option Table 3

The model simulation also requires the temperature difference between the land surface and air ($T_l - T_a$), water surface and air ($T_w - T_a$), and "hot" water and air ($T_{hw} - T_a$). These were adopted from the "World Climate Guide" and are listed in Table 3. The $T_l - T_a$ was in the range of 1–4°C (the highest in August and the lowest during December–March). The $T_w - T_a$ varied from +3°C to -2°C (the highest was in December-January, whereas the lowest (and negative) was during May–July), and it was negative during April-September. The $T_{hw} - T_a$ difference followed a rather similar monthly trend as that of the $T_w - T_a$ difference but it was always positive and had a range of 1–6 °C (the highest was in December-January whereas the lowest was during May–July).

3.3 Model simulations

As mentioned before, the meteorological field simulations were performed based on monthly mean inputs, which are listed in Table 3. The main obtained results for the horizontal wind speed are presented in Figures 2–4, vertical mixing in Figure 5, and surface temperature difference is presented in Figure 6 summarized for winter (January), and summer (July), and averaged over all the twelve months.

Table 3. Monthly means of the weather conditions and temperature differences [°C] between land surface and air ($T_l - T_a$), water surf and air ($T_w - T_a$), and hot-water and air ($T_{hw} - T_a$). The weather data was obtained from the measurement at the campus of the University of Jordan during 2017. The data for temperature differences was obtained from the "World Climate Guide".

Month	Temp. [°C]	RH [%]	Wind Speed [m/s]	Wind Direct. [degree]	Hourly Rainfall [mm/h]	Daily Rainfall [mm]	$T_l - T_a$	$T_w - T_a$	$T_{hw} - T_a$
Jan	7.0	78	1.4	232	0.14	3.36	1.0	3.0	6.0
Feb	8.7	63	1.6	226	0.23	5.52	1.0	2.0	5.0
Mar	12.9	62	1.5	265	0.03	0.72	1.0	1.0	4.0
Apr	17.1	49	1.4	284	0.03	0.72	2.0	- 1.5	1.5
May	20.8	42	1.6	291	0.00	0.00	2.0	- 2.0	1.0
Jun	23.9	49	1.8	304	0.00	0.00	2.0	- 2.0	1.0
Jul	26.5	38	1.9	313	0.00	0.00	3.0	- 2.0	1.0
Aug	26.3	52	1.8	312	0.02	0.48	4.0	- 1.0	2.0
Sep	24.7	52	1.4	321	0.00	0.00	3.0	- 1.5	1.5
Oct	21.1	56	1.0	308	0.17	4.08	2.0	1.0	4.0
Nov	14.3	68	1.1	145	0.04	0.96	2.0	2.0	5.0
Dec	8.1	76	1.1	188	0.14	3.36	1.0	3.0	6.0

Comment: the temperature differences are calculated based on data from the World Climate Guide website (https://www.climatestotravel.com/climate/jordan - publicly accessible) containing also averaged climatological data for air, sea/water temperatures.

The horizontal wind speed profiles are presented for model layer 8 (425–550 m), layer 10 (700–850 m), and layer 12 (1000–1150 m) after 60, 120, and 180 minutes (Figures 2–4) of model simulations. In general, the wind characteristics (speed and direction) were originally developed near the surface to comply with the complexity of the terrain surrounding the studied site. They, then, further propagated along the valleys that are surrounded by dominating mountains. Although the input values of the prevailing wind direction for the model simulations (see Table 3) were different between January and July, the wind direction near the surface was almost similar for all months; i.e. drifting parallel to the valleys (Figure 2a–f, Figure 3a–f, and Figure 4a–f). At the top layer of the model domain, the wind direction and speed were aligned with the monthly input values (i.e. magnitudes of wind speed and prevailing wind direction). As for the wind speed near the surface, it was higher in July than in January (i.e. proportional to the input value). Furthermore, the wind speed was proportional to the slope of the terrain. Quantitatively, after 180 minutes of simulations, the wind speed near the NPP location and close to the terrain surface was in the range 1.3–2.0 m/s in January (Figure 4a) and was slightly higher (1.4–2.6 m/s) in July (Figure 4d). The annual mean wind speed was 1–2 m/s (Figure 4g). Along the valley towards the west sector, the surface wind speed was in the range of 0.5–2.1 m/s in January and 1.0–4.3 m/s in July (annual mean 0.5–3.4 m/s) with the prevailing wind direction down the valley being towards the west. Along the valley towards the east, the surface wind speed was in the range of 1.4–2.1 m/s in January and 2.9–3.2 m/s in July (annual mean 0.7–2.3 m/s) with the prevailing wind direction along the valley being towards the east. The valley on the west side of the domain was steeper and narrower than the valley on the east side.

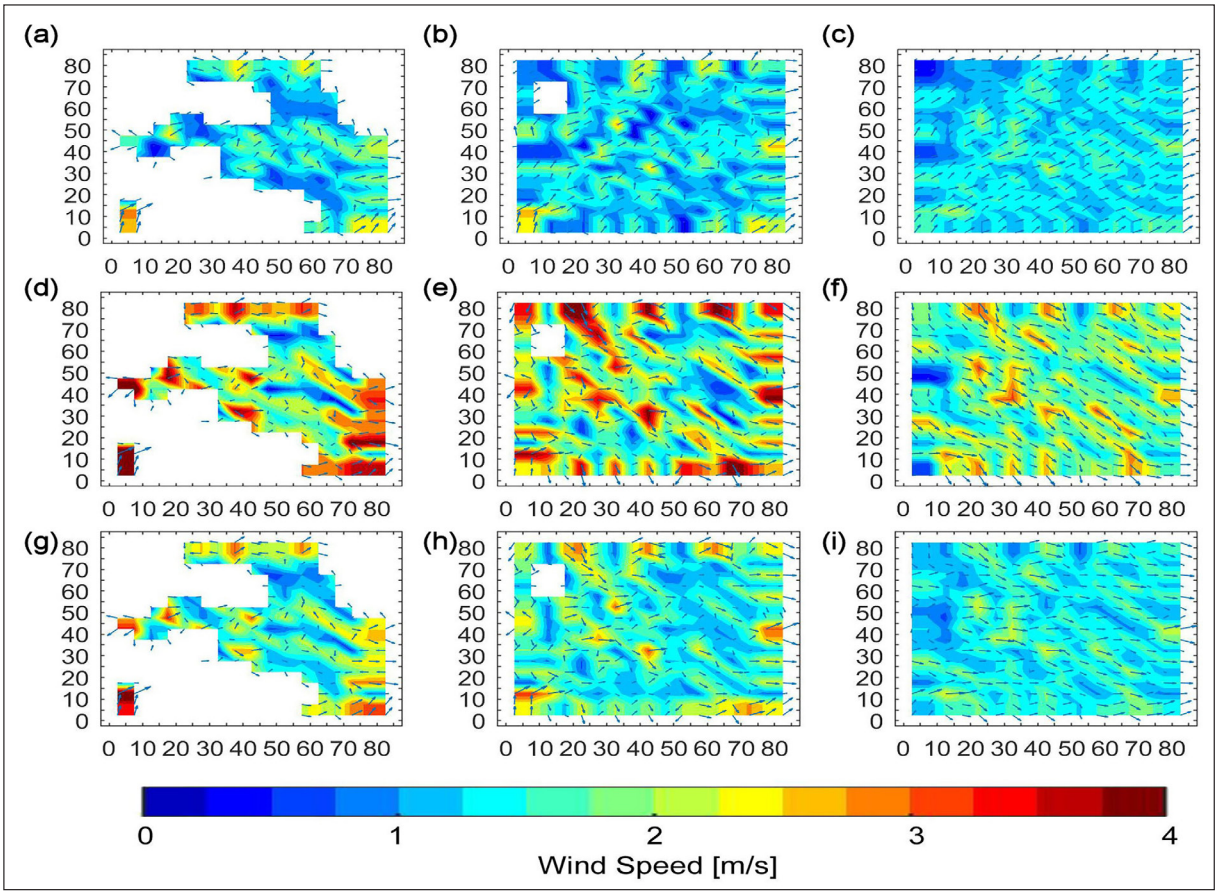

Figure 2. Wind fields simulation after 60 minutes for **(a–c)** January, **(d–f)** July, and **(g–i)** overall annual average. Each row subplots respectively show the simulation results for the model layer 8 (425–550 m.a.s.l.), layer 10 (700–850 m.a.s.l.), and layer 12 (1000–1150 m.a.s.l.).

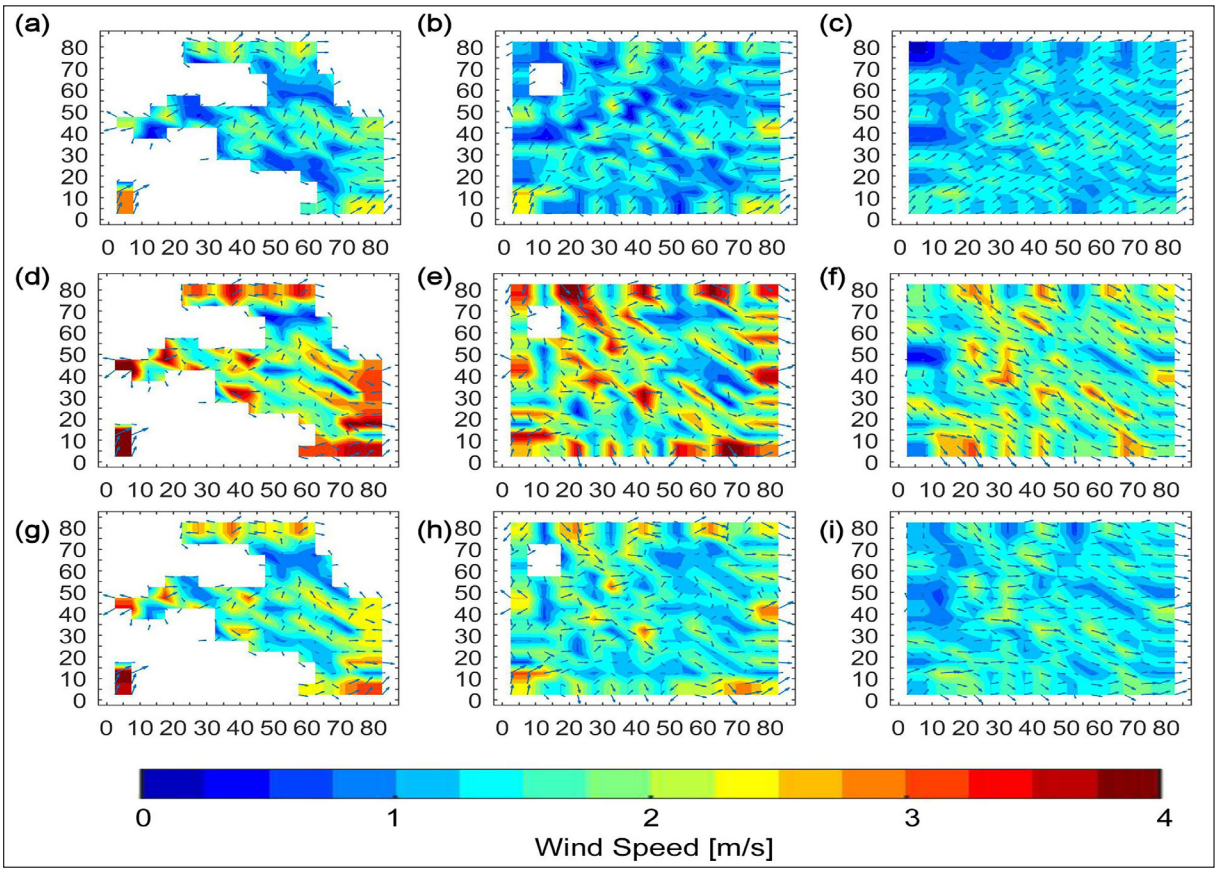

Figure 3. Wind fields simulation after 120 minutes for **(a–c)** January, **(d–f)** July, and **(g–i)** overall annual average. Each row subplots respectively show the simulation results for the model layer 8 (425–550 m asl), layer 10 (700–850 m asl), and layer 12 (1000–1150 m asl).

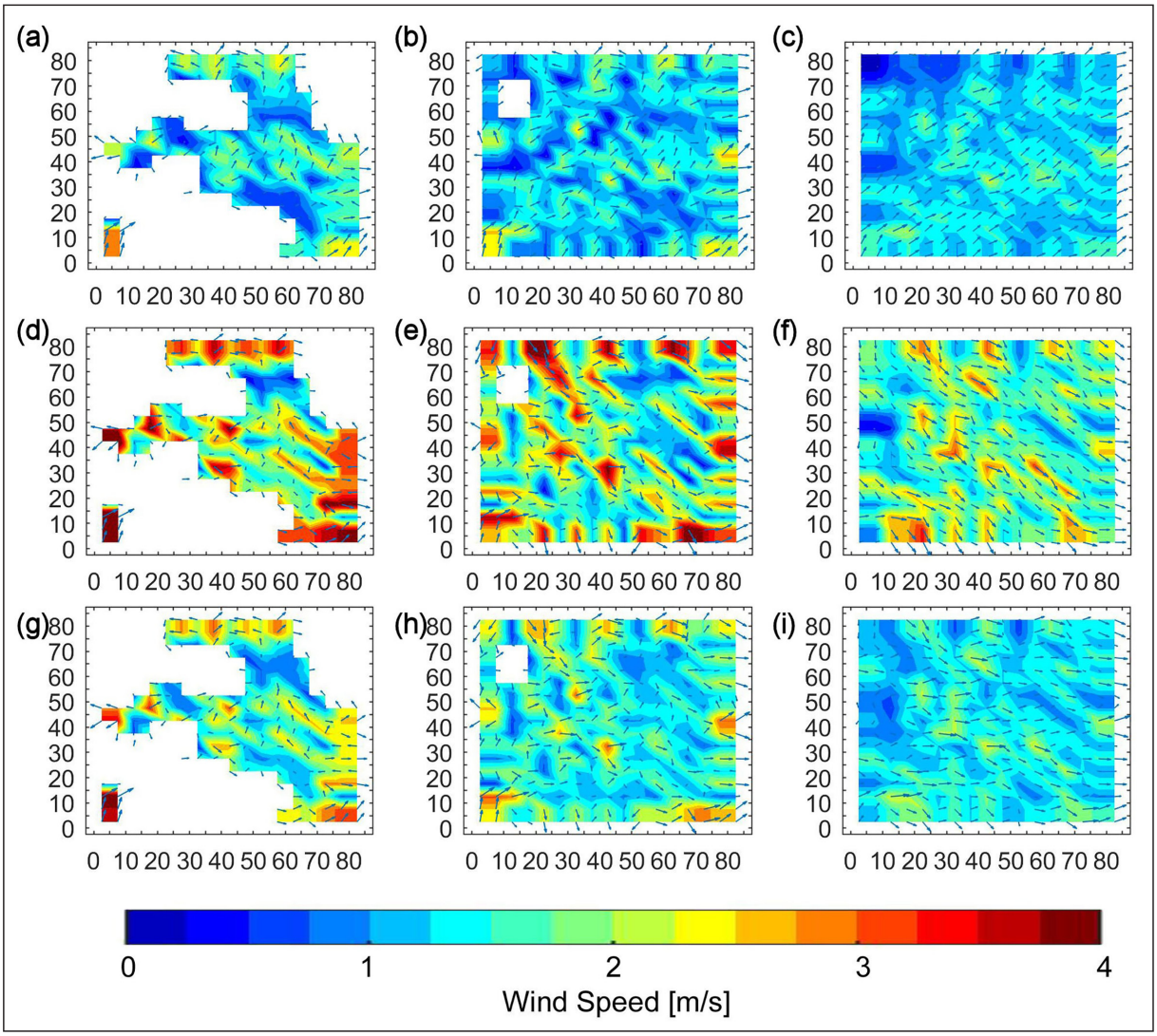

Figure 4. Wind fields simulation after 180 minutes for **(a–c)** January, **(d–f)** July, and **(g–i)** overall annual average. Each row subplots respectively show the simulation results for the model layer 8 (425–550 m.a.s.l.), layer 10 (700–850 m.a.s.l.), and layer 12 (1000–1150 m.a.s.l.).

As shown in Figure 5, the vertical component of wind velocity was the lowest (nearly zero in January and ~0.1 m/s either up or down in July) near the surface. The vertical component increased (being slightly higher than 0.1 m/s in January and higher than 0.2 m/s in July) due to turbulence with air parcels lifting up a layer-by-layer in the domain. The increasing rate of the vertical motion with a height was stronger in July than in January (Figure 5a–d).

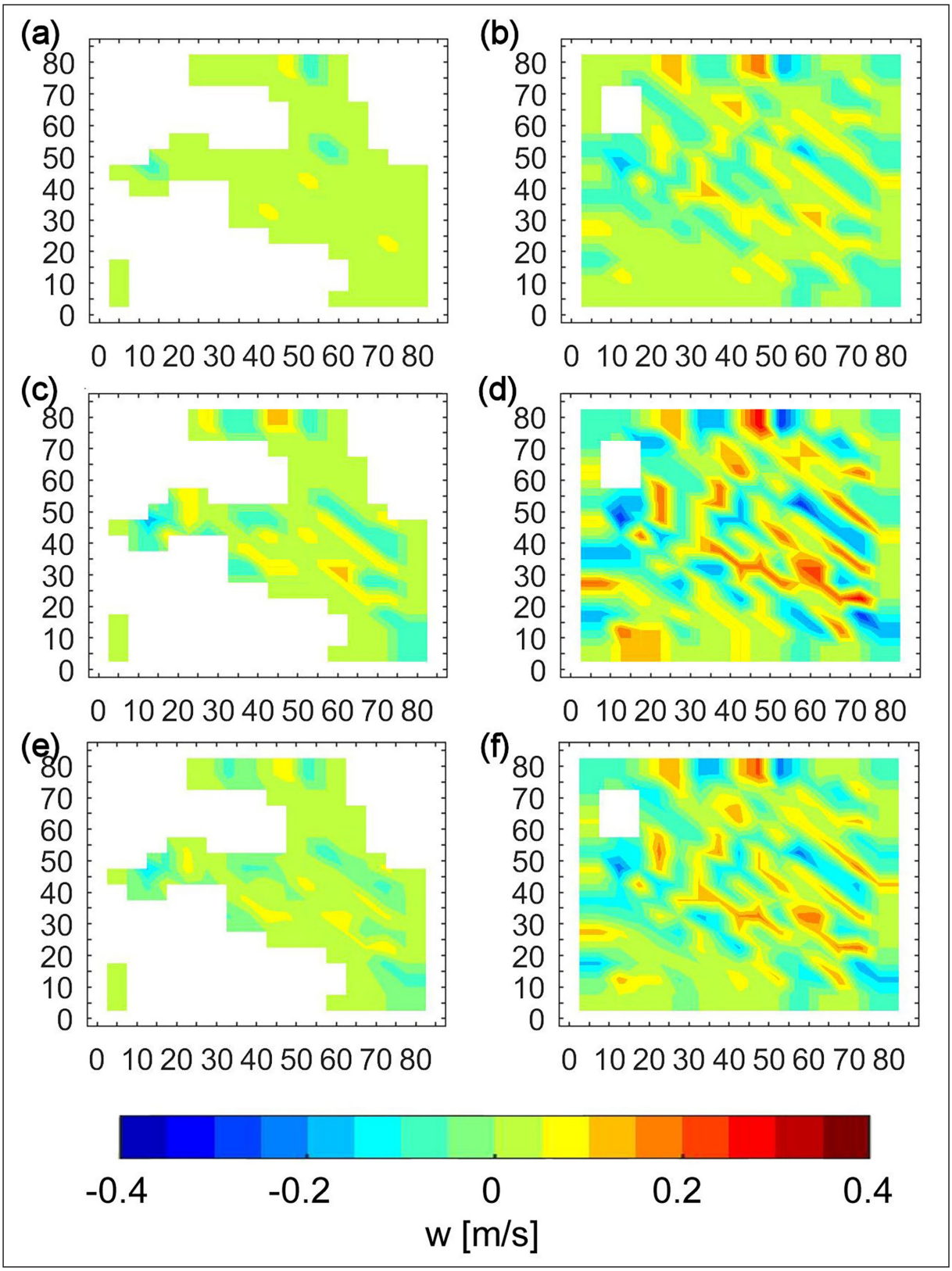

Figure 5. Vertical component of wind velocity simulated after 180 minutes for **(a–b)** January, **(c–d)** July, and **(e–f)** overall annual average. Each row subplots respectively show the simulation results for the model layer 8 (425–550 m.a.s.l.) and layer 10 (700–850 m.a.s.l.).

Conversely and as expected, the temperature differences between the surface and the atmosphere were higher near the surface than in the higher layers (Figure 6). Furthermore, the temperature differences near the surface were higher in July than in January (reaching 1.5 °C versus 0.5 °C, respectively).

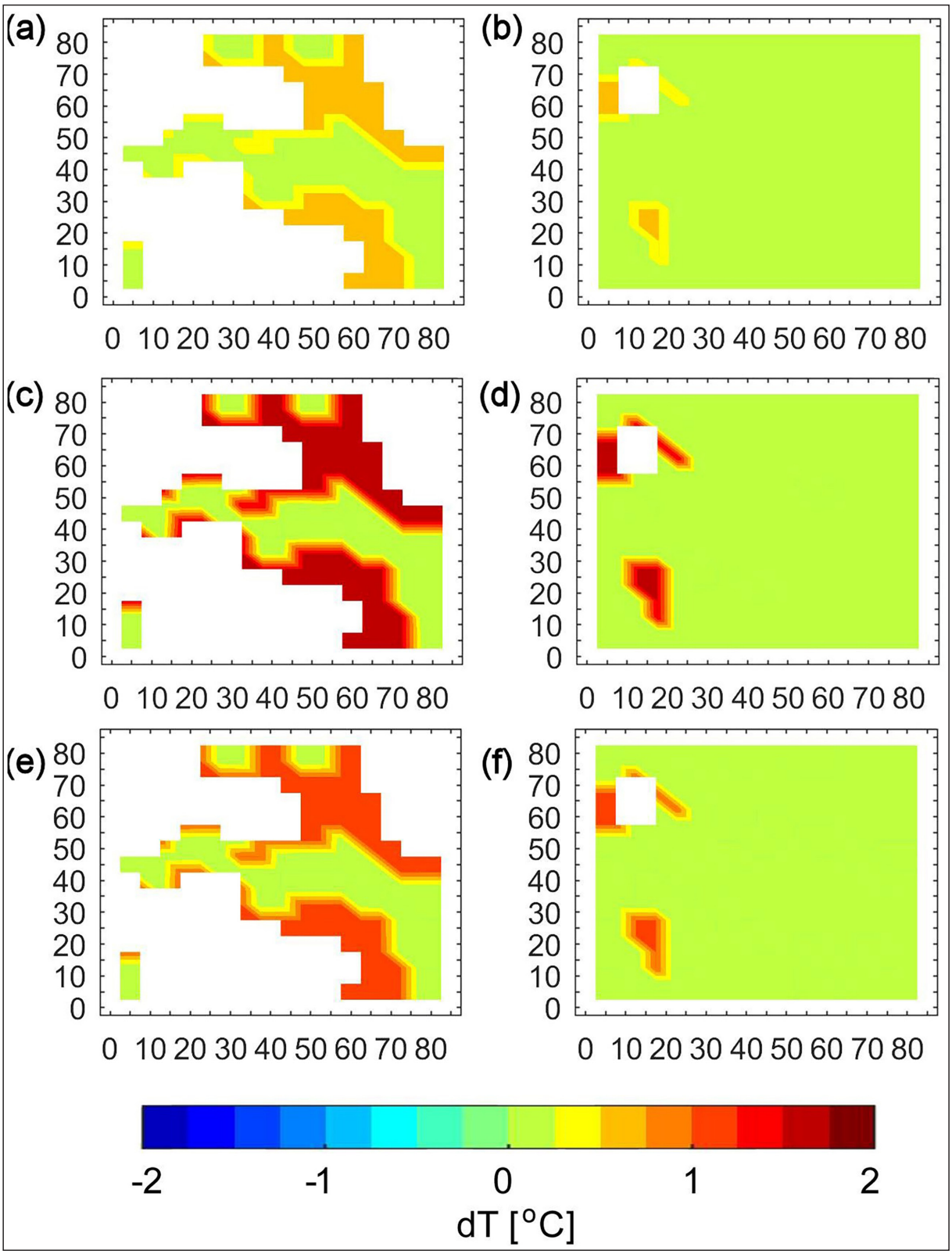

Figure 6. Temperature difference simulation after 180 minutes for **(a–b)** January, **(c–d)** July, and **(e–f)** overall annual average. Each row subplots respectively show the simulation results for the model layer 8 (425–550 m.a.s.l.) and layer 10 (700–850 m.a.s.l.).

4. Summary and conclusions

In practice, nuclear safety is very strict, so that accidents are less probable to occur at a nuclear power plant (NPP). Nevertheless, accidents were reported several times over the past eighty years. Jordan is a developing country which relys on importing more than 90% of its energy needs. As a solution for the increasing energy demand in Jordan, the energy mix was planned to utilize nuclear power, and consequently, Jordan has started planning for the construction of NPPs. However, investigations of the meteorological conditions and mass transfer have never been conducted in relation to any of the suggested sites.

This study is aimed at stimulating and investigating the meteorological conditions (horizontal wind fields, vertical wind component, and surface temperature differences) near one of originally suggested geographical locations (the site of the Samra Energy Power Plant, SEPP) to construct a NPP in Jordan. The model domain had a size of 85×85 km^2 (17×17 horizontal grid points and 13 vertical layers) centering around the SEPP site (32.1443 °N, 36.1428 °E; 560 m a.s.l.), which is located in the northeastern part of Jordan. The model simulations were performed based on monthly-averaged meteorological conditions.

The model simulations revealed that the wind direction near the surface was developed to comply with the complexity of the terrain regardless of the input values of the prevailing wind direction. For instance, they propagated along the valleys surrounded by the dominating mountains. As for the wind speed near the surface, it was proportional to the input value of the wind speed; i.e. higher in summer than in winter. The wind speed was also proportional to the slope of the surrounding terrain. Quantitatively, the developed surface wind speed near the studied location was 1.3–2.0 m/s in January compared to 1.4–2.6 m/s in July. Along the valleys, the surface wind speed was 0.5–2.1 m/s in January compared with 1.0–4.3 m/s in July.

The vertical component of wind velocity was the lowest (negligible in January versus ~0.1 m/s in July) near the surface. As a result of the turbulence processes, the vertical wind speed increased (slightly higher than 0.1 m/s in January, while it was higher than 0.2 m/s in July).

It should be noted that this kind of investigation has never been conducted or reported before regarding the Jordanian conditions. The current study presented in this manuscript will hopefully serve as a base-block for other possible applications concerning other geographical locations in Jordan and also for assessment studies of the possible consequences in case of accidental releases from other potential objects with possible nuclear, chemical, and industrial danger.

Acknowledgment

Marwan Al-Kloub would like to thank colleagues from the University of Helsinki, Institute for Atmospheric and Earth System Research (UHEL-INAR) for hosting him as a visiting researcher. He also would like to thank colleagues at INAR for useful discussions and constructive criticism. The Royal Jordanian Air Force and Prince Faisal Technical College are both acknowledged for supporting this work at the University of Jordan and for providing research mobility for Al-Kloub. This work was scientifically supported by the Pan-Eurasian EXperiment (PEEX; https://www.atm.helsinki.fi/peex) Programme, the Academy of Finland Center of Excellence Programme (CoE-ATM, grant no. 307331). The INEP's Model Package (METEO and TRANS) was initially setup, tested, and optimized at the Center for Science Computing (CSC; www.csc.fi) HPC Sisu supercomputer.

References

AGROS, https://pdc-argos.com/index.html, accessed on June 19, 2019.

Baklanov, A. (2003). Evaluation of Dose, Risk, Vulnerabilities and Consequences for Population and Environment in Euro-Arctic Region. Danish Meteorological Institute, Sci. Rep. 03–18.

Baklanov, A., and Mahura, A. (2001). Atmospheric Transport Pathways, Vulnerability and Possible Accidental Consequences from Nuclear Risk Sites: Methodology for Probabilistic Atmospheric Studies. Danish Meteorological Institute, Sci. Rep. 01–09.

Baklanov, A., Mahura, A., Jaffe, D., Thaning, L., Bergman, R., Andres, R. (2002). Atmospheric Transport Patterns and Possible Consequences for the European North after a Nuclear Accident. Environ. Radioac. 60: 1–26.

Baklanov, A., Mahura, A., Morozov, S. (1994). The Simulation of Radioactive Pollution of the Environment after a Hypothetical Accident at the Kola Nuclear Power Plant. Environ. Radioac. 25: 65–84.

Baklanov, A., Mestayer, P., Clappier, A., Zilitinkevich, S., Joffre, S., Mahura, A., Nielsen, N. (2008a). Towards improving the simulation of meteorological field in urban areas through updated / advanced surface fluxes description. Atmos. Chem. Phys. 8: 523–543.

Baklanov, A., Morozov, S., Naumov, A., Amosov, P., Mahura, A., Fedorenko, Y., Rigina, O., Koshkin, V. (2000). Assessment of Potential Risk for Kola's Population from Radiological Impact of Accident on Spent Nuclear Fuel Facilities. Res. Rep., OCB-RW Project. 98: 03–26.

Baklanov, A., Sørensen, J., Mahura, A. (2008b). Methodology for Probabilistic Atmospheric Studies using Long-Term Dispersion Modelling. Environ Model Assess. 13: 541–552.

Cao, B., Zheng, J., Chen, Y. (2016). Radiation Dose Calculations for a Hypothetical Accident in Xianning Nuclear Power Plant. Sci. Technol. Nucl. ID 3105878.

Christoudias, T., Proestos, Y., Lelieveld, J. (2014). Atmospheric Dispersion of Radioactivity from Nuclear Power Plant Accidents: Global Assessment and Case Study for the Eastern Mediterranean and Middle East. Energies 12: 8338–8354.

Davydova, G.V., Morozov, S.V., Sharowuox G.A. (1990). The Methods of Mathematical Modelling of the Distribution of Radioactive Pollution from Nuclear Power Plants. Institute of Nuclear Energy of Academy of Science of Byelorussia, Minsk, p. 20, (in Russian).

Evangeliou, N., Hamburger, T., Talerko, N., Zibtsev , S., Bondar, Y., Stohl , A., Balkanski, Y. (2016). Reconstructing the Chernobyl Nuclear Power Plant (CNPP) Accident 30 years after. A unique database of air concentration and deposition measurements over Europe. Environ. Pollut. 216: 408–418.

Glyshenko, A. N. el al. (1981). About method choice of distribution of radioactive pollution from nuclear power plants into atmosphere. In the Nuclear Power Plants 4, Atomenergoizdat, Moscow, P. 60, (in Russian).

Hussein, T., Juwhari, H., Al Kuisi, M., Alkattan, H., Lahlouh, B., Al-Hunaiti, A. (2018). Accumulation and Coarse

Modes Aerosols Concentrations and Carbonaceous Contents in the Urban Background Atmosphere in Amman – Jordan. Arab. J. Geoscie 11, 617.

INES, International Nuclear and Radiological Event Scale, https://www.iaea.org/topics/emergency- preparedness-and-response-epr/international-nuclear-radiological-event-scale-ines, accessed on June 19, 2019.

Kawamura, H., Kobayashi, T., Furuno, A., Usui, N., Kamachi, M. (2014). Numerical simulation on the long- term variation of radioactive cesium concentration in the North Pacific due to the Fukushima disaster. J. Environ. Radioact. 136: 64–75.

Lauritzen, B., Baklanov, A., Mahura, A., Mikkelsen, T., Sørensen, J. (2007). Probabilistic risk assessment for long-range atmospheric transport of radionuclides. J. Environ. Radioact. 96: 110–115.

Mahura, A., Baklanov, A., Sorensen, J., Parker, F., Novikov, V., Brown, K., Compton, K. (2005). Assessment of potential atmospheric transport and deposition patterns Russian Pacific fleet operation. Environ. Monit. Assess. 101: 261–287.

Mahura, A., Jaffe, D., Andres, R., Merrill, J. (1999). Atmospheric transport pathways from the Bilibino nuclear power plant to Alaska. Atmos. Environ. 33: 5115–5122.

Matsuda, N., Mikami, S., Sato, T. (2017). Measurements of air dose rates in and around houses in the Fukushima Prefecture in Japan after the Fukushima accident. J. Environ. Radioact. 166: 427–435.

Mazur, A., Bartnicki, J., Zwozdziak, J. (2014). Operational model for atmospheric and deposition of air pollution. Ecol Chem Eng S. 21: 385–400.

Mészáros, R., Leelőssy, A., Vincze, C., Szűcs, M., Kovács, T., Lagzi, I. (2012). Estimation of the dispersion of an accidental release of radionuclides and toxic materials based on weather type classification. Theor Appl Climatol. 107:375–387.

Mitrakos, D., Potiriadis, C., Housiadas, C. (2016). An approach for estimating the radiological significance of a hypothetical major nuclear accident over long distance transboundary scales. Nucl. Eng. Des. 300: 422–432.

Momoshima, N., and Bondietti, E. (1994). The Radial Distribution of 90Sr and 137Cs in Trees. J. Environ. Radioact. 22: 93–109.

Srinivas, C., and Venkatesan, R. (2005). A simulation study of dispersion of air borne radionuclides from a nuclear power plant under a hypothetical accidental scenario at a tropical costal site. Atmos. Environ. 39: 1497–1511.

World Climate Guide, Climates for Travel, https://www.climatestotravel.com/climate/jordan, accessed in December 2018.

JJEES

JJEES (2020) 11 (1): 38-48
ISSN 1995-6681

Jordan Journal of Earth and Environmental Sciences

Challenges to Sustainable Water Management in Jordan

Atef Al-Kharabsheh[1,2]

[1]Al-Balqa Applied University, Faculty of Agricultural Technology
[2]German Jordanian University, School of Natural Resources Engineering and Environment, Department of Civil Engineering and Environment, Jordan

Received 6 January 2019, Accepted 13 October 2019

Abstract

Water crisis in Jordan is the most critical common limitation to the country's financial development and advancement. The crisis is exacerbating with time, because of the quick increase in population that is associated with sudden refugee fluxes and because of the inefficient use of water which both have made exceptional demands on water resources. The importance of this paper lies in estimating the effectiveness of technical water management and assessing the extent of management capacity in the reduction of water scarcity in the Kingdom of Jordan.

Despite the governmental efforts to manage the country's limited water resources and the relentless search for alternative supplies, the adopted political, financial, and technical responses are still limited to maintain a balance between demand and supply. Several of the inspected adaptation measures include desalination, reuse of treated wastewater and greywater, storm water collection, rationale/efficient water use, among others. The results indicated that these measures can reduce the impact of water crisis; however, they are not enough to compensate for the kingdom's future demands and for a better financial development. Accordingly, only mega-projects are preferred which may sound the only solution to escape the bottleneck of the crisis. A multidimensional incorporation of all water related parties at all levels of the citizens, the government, and politicians is required. It is important to direct the policies of the water sector towards water resilience and governance. One of the most important actions to consider is to make proactive and contingency plans enhanced by the policies and legal frameworks at the national level to ensure a sustainable water resilience and governance.

Keywords: water, crisis, management, adaptation, wastewater, desalination, red-dead sea project, Jordan.

1. Introduction

Jordan, a country of the Middle East region, is located to the east of the Mediterranean Sea with an average area of about 89,210 km^2. The country is bordered by Syria from the north, Iraq from the northeast, Saudi Arabia from the southeast and the south and by Palestine from the west (Figure 1). Due to the dry and semi-arid climate, the sound administration of water resources has been an issue in Jordan since the establishment of the Kingdom of Jordan in 1946.

From the physiographical standpoint, the country can be divided into four districts: (1) The Ghors (marshes) in the western portion of the country, which is comprised of three zones: The Jordan Valley which begins at Lake Tiberius in the north, the swamps along the Dead Sea and the Wadi Araba which expands in a southerly heading to the northern shores of the Red Sea (total region: 5000 km^2); all of the Ghor regions are found to be below the sea level (2) The highlands, which run from the north to the south at an elevation of between 600 m and 1600 m over the sea level (total zone: 5510 km^2), (3) The plains, which extend from the north to the south along the western borders of the desert (Badiah) (total region: 10,000 km^2), and finally (4) The desert region (Badiah) in the east, which is an expansion of the Middle Eastern desert (total region: 68,700 km^2) (MoEnv, 2015).

Jordan's climate is characterized by long hot and dry summers and wet cold winters. The temperature increases towards the south, with the special case of a few southern highlands. Precipitation shifts impressively with area, primarily due to the country's topography (Al-Kharabsheh, 2013). The precipitation diminishes from 600 mm at the northwestern part of the country to less than 100 mm at the extraordinary southeastern deserts; more than 93% of the country receives a precipitation of less than 200 mm (Figure 2 and Table 1). Looking over time; and due to climatic change impacts and drought events, the annual precipitation volume is being negatively deviated from the long term mean (Table 2). Based on the third national communication report to UNFCCC, Jordan is expected to have a warmer and drier climate with a potential increase in air temperature from +2.1 °C to +4°C and a decrease in the annual rainfall from 15% up to 35% in 2100 (MoEnv, 2014).

In 2017, the yearly precipitation for the country was of 8165 MCM, from which 93.5% are lost through evaporation, while 2.1% is considered floods and 4.4% flows as groundwater recharge (MWI, 2017). The level of the Dead Sea falls each year by 85 centimeters (cm), due to broad water utilization in the Dead Sea basin. Watered soils along the Jordan Valley are showing signs of salinization since the characteristic floods are no longer accessible to flush the flooded land and filter the salts (MWI, 2017).

Jordan is among the countries with the scarcest renewable water resources per capita in the world; it ranked the second poorest in 2017, with only 100 m^3 per capita per year which appears to be diminishing each year, and is expected to reach almost 80 m^3 in the year 2020 (MoEnv, 2014; World Bank, 2007; MWI, 2017). This is far below the

* Corresponding author e-mail: atefkh9@yahoo.com

per capita water resources accessible in other countries of the Middle East, which may reach almost 1000 m^3 (FAO, 1995). Water demand surpasses the accessible renewable water supply, to the extent that the groundwater table in nearly the entire country is falling. The demand on water is rising due to populace development, higher living measures, refugee problems, the extension of inundated lands, and industrialization (UNICEF, 2006).

As a result of all of the aforementioned circumstances including the increasing demands on the water supply due to the population growth and the high needs being exacerbated and magnified by the sudden refugees' influxes into the country, in addition to the fact that Jordan's surface water resources are shared by the neighboring countries whose control has partially deprived Jordan of its fair share of water, the gap between water supply and demand is becoming bigger and wider creating a "Jordanian water resources' scarcity" which is considered the most important environmental and social challenge facing Jordan nowadays. The current use already exceeds the renewable supply, which is covered by over-drafting renewable and nonrenewable supplies especially at highland aquifers, resulting in lowered water tables and a declining water quality.

Several ideas and measures have been highlighted recently and even implemented to reduce the pressure on the water demands and supplies by all sectors including a rational use of water, water recycling, improvement of irrigation techniques, reducing water loss in distribution, water harvesting, and desalination; however, a sustainable solution to meet all demands has not been reached yet. The objective of this paper is to highlight the water needs, the designed and implemented solutions, and discuss their sustainability to overcome the national actual needs overtime.

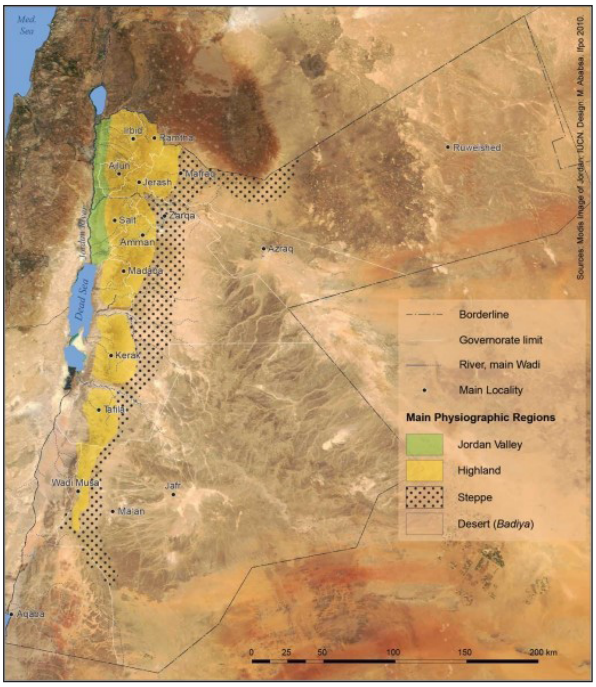

Figure 1. Location Map of Jordan. (Ababsa, 2013)

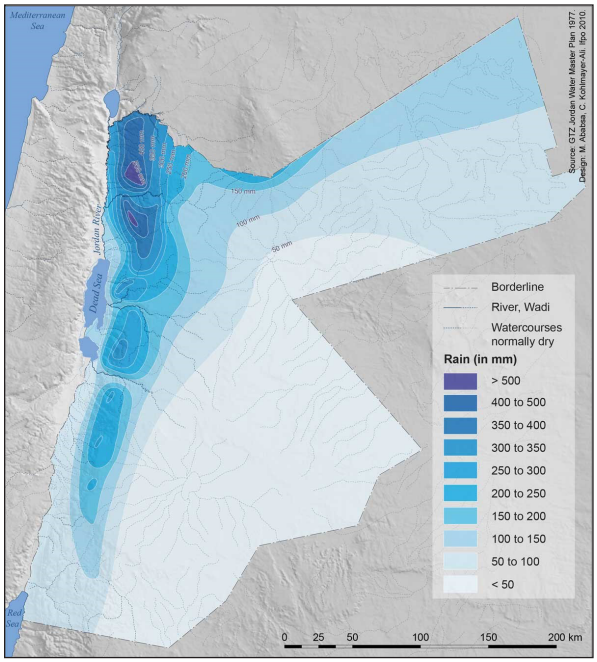

Figure 1. Location Map of Jordan. (Ababsa, 2013)

Table 1. Climatic classification agreeing to precipitation dispersion in Jordan.

Zone	Annual Rainfall (mm/year)	Area (km^2)	Area as a percentage of the total area of Jordan
Semi- humid	500-600	620	0.7 %
Semi- arid	300-500	2,950	3.3 %
Marginal	200-300	2,030	2.2 %
Arid	100-200	20,050	22.3%
Desert	< 100	64,350	71.5 %
Total		**90,000**	**100 %**

Table 2. Annual precipitation deviation from a long term rate (MWI, 2017).

Year	Rainfall Volume (MCM)	Long-term Rate (MCM)	Deviation from Long term Rate
2006/2007	7683	8313	-630
2007/2008	5194	8269	-3075
2008/2009	6379	8243	-1864
2009/2010	8728	8249	479
2010/2011	6477	8225	-1748
2011/2012	5943	8195	-2252
2012/2013	8120	8194	-74
2013/2014	7228	8181	-953
2014/2015	8884	8191	693
2015/2016	9483	8207	1276
2016/2017	8165	8206	-41

2. Population Growth

Based on the logistic modeling of the growth rate in Jordan (equation 1), it seems that the sudden refugees' influxes are considered the most unstable growth factor affecting the population growth and the related political and financial development in the country (Figure 3). The populace development is around 3.4% not counting variances caused by universal political occasions, while it exceeded 5% when counting sudden refugee influxes.

$$Population = \frac{\left(\frac{a}{b}\right) \times c}{\left(c + \left(\frac{a}{b} - c\right)\right) \times e^{-(a \times year - 1952)}} \quad \text{. . Equation 1}$$

where a and b are birth and death rates, c is the population at time zero (in this case the intial data is 1952).

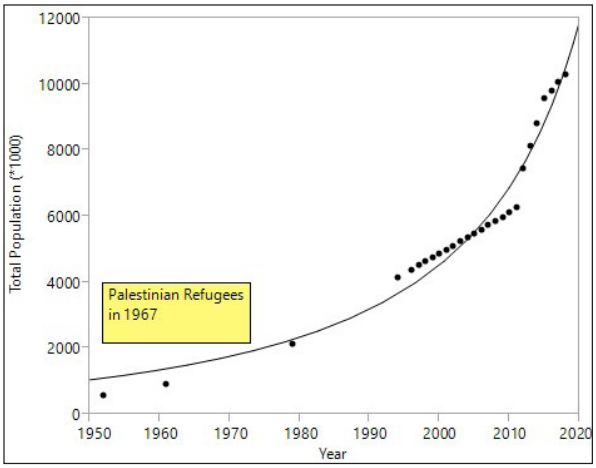

Figure 3. Population growth rate in Jordan including the sudden refugee fluxes.

These sudden fluxes are considered a threat to the water security of the kingdom of Jordan not only temporarily through managing the available resources and connection networks, but may have consequences even on the long run. According to MWI (2017), the increase in demand for domestic water in the northern governorates has increased by 40% over the last few years as a result of hosting Syrians. Each Syrian refugee costs the water sector around 440JD/year. These impacts will worsen for generations and decades to come, if solutions are not found to ensure the sustainability of the available resources. One of the most important consequences that have been explained so far is the lack of water stability, lack of extension, raising tariffs, and the environmental impact associated with the inability to maintain the available resources, the decrease of the underground level, and the ensuing increase in poverty, unemployment, and indebtedness.

Approximately 90% of the population of Jordan is concentrated in the northern and central portions of the country, where precipitation is most elevated and most of the water resources are available there. About 90% of the drinking water supplied to the capital comes from sources distanced 125 to 325 km away and elevated up to 1200m with five pumping stages, while 42 % of the drinking water supplied to the northern governorates comes from sources distanced 20 to 76 km away and elevated up to about 1200m with four pumping stages (which indicates the higher cost for the water supply).

3. Available Water Resources and their Employments

Utilized water in Jordan is derived from three main resources; 27% of the water is derived from surface water, 59% from groundwater, and 14% from treated waste water. Fresh water resources in Jordan consist mainly of groundwater and surface water. Treated wastewater and brackish water desalination are other important non-conventional resources that help bridge part of the gap between supply and demand especially in the municipal and agricultural sector. The different available water resources in Jordan are as follows:

3.1 Jordan's Surface Water Resources

Surface water is dispersed unevenly in fifteen basins (Figure 4). The biggest source by distance is the Yarmouk River, which is located to the east of the Jordan Valley Basin. This river provides nearly 50 % of Jordan's surface water resources; however, due to the Syrian crises and the huge consumption from the Syrian side, the flow rate of this river is decreasing substantially. The normal yearly base-flow of all rivers in Jordan is approximately 451.4 MCM and the normal yearly flood stream is around 255.5 MCM. Flood flows represent 3.04 % of the total yearly precipitation (Table 3).

The Yarmouk River drains into the basaltic plateaus of the Hauran in Syria, an area of fair rainfall and strong runoff. The typical monthly flows of the Yarmouk River at Adasiyia are between 4 and 5 MCM during the dry season and between 17 and 40 MCM during winter. About 110 MCM per year of the Yarmouk River, Al-Wehda dam and the Mukhieba Wells are diverted to KAC, 70 MCM of which are pumped to the Zai water treatment plant which supplies west Amman. The remaining 40 MCM are used for irrigation in the Jordan valley (MWI, 2013). The Zarqa River is the second largest tributary of the Jordan River. The mean rainfall for the watershed is 273 mm, and the median annual stream flow is 70 MCM. In the year 2013, the annual discharge was a record of 135 MCM (AFD and CMI, 2011).

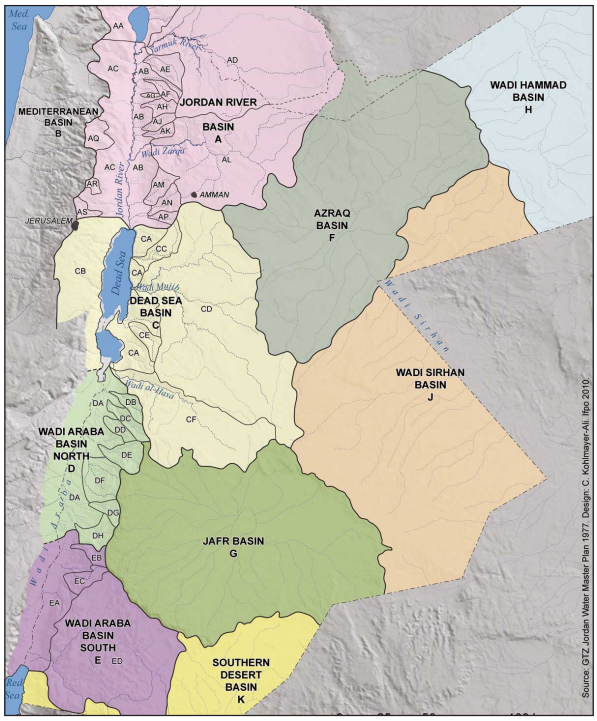

Figure 4. Surface Water Basins in Jordan (MWI Files).

Table 3. Surface Water Basins in Jordan (From GTZ Water Master Plan, 2004).

No	Surface Water Basin			Basin Name		Basin Code	Catchment Area (km2)	Average Annual Rainfall (mm/year)
	Basin/Area							
1	Dead Sea Basin	Jordan River Subbasin		Yarmouk		AD	1,426	280
2				Amman-Zarqa		AL	3,739	220
3				Jordan Valley		AB	780	270
4				Jordan Valley Rift Side Wadis	North	AE, AF, AG AH, AJ,AK	946	490
5					South	AM, AN, AP	736	370
6		Dead Sea Subbasin	Central Basins	Mujib		CD	6,727	180
7				Hasa		CF	2,603	130
8				Dead Sea Rift Side Wadis		C	1,508	240
9				North Wadi Araba		D	2,953	180
10	Eastern Desert Basin			Azraq		F	12,400	85
11				Hammad		H	18,047	85
12				Sirhan		J	15,733	45
13				Jafr		G	12,363	45
14	Southern Basins			South Wadi Araba		E	3,742	75
15				Southern Desert		K	6,296	15
Total							**90,000**	**100**

3.2 Jordan's Groundwater Resources

Groundwater is the major water resource for municipal water use. In most urban sites, water is supplied on an intermittent, rationed basis that requires household storage in cisterns and/or roof tanks. Jordan's groundwater is dispersed across twelve basins (Figure 5). The main types of aquifers in Jordan are limestones, sandstones, and basalts (GTZ, 1995). The sum of recharge in a renewable aquifer determines the safe yield, which can be withdrawn each year without imperiling groundwater supply in the future. Numerous ponders and gauges have been carried out on groundwater resources in Jordan. Based on these, it can be concluded that the safe yield of all renewable aquifers is 275 MCM per year, while the safe yield abstraction quantity from nonrenewable groundwater for fifty years is about 143 MCM (Al-Hadidi and Al-Kharabsheh, 2015).

The number of working wells in Jordan exceeds 3211 wells; however, there are many unauthorized wells that increase the non-revenue water percentage each year. The quantity of over-pumping from groundwater is estimated at about 200 MCM. It should be taken into account that 52% of the available water is used for agriculture, and 46% of which comes from groundwater sources. Recent documentations indicate that the groundwater level in the main aquifers drops at a rate of 2 meters per year, but the decline in some depleted areas reaches 5 to 20 meters.

Jordan's major non-renewable aquifer is in the Disi region in the south, where the final major recharge happened approximately 10,000 years ago, when the climate in the region was more humid. This is the fundamental non-renewable resource directly exploited in Jordan. A few studies have concluded that the safe yield of the aquifer is 125 MCM/y for 50 years and its water quality is generally less than 500 mg/l. Other nearby nonrenewable groundwater resources are found in the Jafr Basin with a yearly safe yield of 18 MCM/y.

The request to cover the needs of the diverse divisions has expanded from 639 MCM in the year 1985 to 1279 MCM recently, and is anticipated to increase to more than 1312 MCM in the year 2020 (Table 3). The source of these requests is surface water, groundwater, and treated wastewater (Table 4). Groundwater is considered a major immoderate source amid the past period, Table 5 shows that pumping from groundwater expanded from 479 MCM in the year 2006 to almost 508 MCM in the year 2012, while the safe yield of these aquifers is only 275 MCM (USAID, 2009).

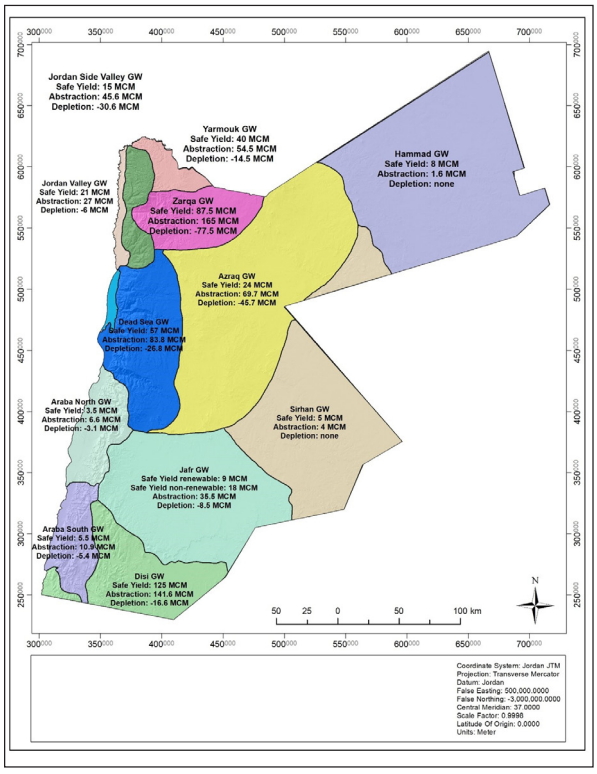

Figure 5. Groundwater Basins in Jordan.

3.3 Jordan's Wastewater Resources

The Water Authority of Jordan (WAJ) is responsible for domestic wastewater management. On the other hand, the Aqaba Water Company and the Yarmouk Water Company are responsible for the operation of the WWTP in their regional delineations. Currently, there are twenty-seven working wastewater treatment plants (WWTP) in Jordan that are designed to treat 407,930 cubic meter per day. Table 4 shows the quantities of wastewater discharged to the working WWTPs in 2017. Samra WWTP receives more than 70% of wastewater diverted to WWTPs, while the Mansourah WWTP for septic tanks receives only around 0.005% of the total wastewater discharged.

The ratio of water used in the industrial sector in relation to the total use is very small and is estimated at about 5%. In industrial states, industries usually have WWTPs or pretreatment units inside their vicinity where they work before discharging their wastewater to the central WWTPs or to other locations to be used for tree irrigation or in the nearby Wadis. Also, many industries (food processing, yoghurt, etc) are connected to the sewage network as their wastewater complies with connection requirements.

The reuse of wastewater is now regulated by several sets of standards, including ones governing the discharge of toxic materials to sewers and others that established standards for reuse of wastewater and the processing and use of sludge. Challenges facing the expansion of the re-use of reclaimed wastewater from industries include the location of these industries relative to wastewater treatment facilities, the quality of treated wastewater relative to industry standards, the cost of refining the treatment levels to higher standards, and the cost of building new conveyances from central wastewater treatment facilities to industrial sites.

Table 6. Wastewater treatment plants in Jordan (WAJ Files).

No.	Treatment plant name	Year of commissioning	Treatment technology	Design flow (m^3/day)	Actual average flow (m^3/day) 2010	Operator
1	Aqaba Natural	1987	Stabilisation ponds	9,000	6,371	AWC
2	Aqaba Mechanical	2005	Extended aeration	12,000	9,846	AWC
3	Al Baqa	1987	Trickling filter	14,900	10,209	WAJ
4	Fuheis	1997	Activated sludge	2,400	2,221	WAJ
5	Irbid Central	1987	Trickling filter & activated sludge	11,023	8,132	YWC
6	Jerash (East)	1983	Oxidation ditch	3,250	3,681	YWC
7	Al Karak	1988	Trickling filter	785	1,753	WAJ
8	Kufranja	1989	Trickling filter	1,900	2,763	YWC
9	Madaba	1989	Activated sludge	7,600	5,172	WAJ
10	Mafraq.	1988	Stabilisation ponds	1,800	2,009	YWC
11	Ma'an	1989	Extended aeration	5,772	3,171	WAJ
12	Abu Nuseir	1986	Activated sludge R, B, C	4,000	2,571	WAJ
13	Ramtha	1987	Activated sludge	7,400	3,488	YWC
14	As Salt	1981	Extended aeration	7,700	5,291	WAJ
15	Tafila	1988	Trickling filter	1,600	1,380	WAJ
16	Wadi Al Arab	1999	Extended aeration	21,000	10,264	YWC
17	Wadi Hassan	2001	Oxidation ditch	1,600	1,132	YWC
18	Wadi Musa	2000	Extended aeration	3,400	3,029	WAJ
19	Wadi as Sir	1997	Aerated lagoon	4,000	3,624	Miyahuna
20	Al Ekeder	2005	Stabilisation ponds	4,000	3,908	YWC
21	Al Lijoon	2005	Stabilisation ponds	1,000	853	YWC
22	Tall Almanta	2005	Trickling filter & activated sludge	400	300	
23	Al Jiza	2008	Activated sludge	4,000	704	
24	As Samra	1984	Activated sludge	267,000	230,606	Suez-Morganti
25	Al Merad	2010	Activated sludge	10,000	1,000	
26	Shobak	2010	Stabilisation ponds	350	100	WAJ
27	Al Mansorah	2010	Stabilisation ponds	50	15	
Total				**407,930**	**323,951**	

4. International Waterways

An International Waterway refers to a river whose streams are shared between two or more countries. Most of Jordan's water resources are shared with other countries. The Jordan River is the biggest river of the country, yet the Israelis redirect most of its water. Water allocation to riparian nations is one of the most troublesome territorial issues (GTZ, 1999). Other critical shared-water resources are the groundwater resources of North Jordan (Azraq, Yarmouk, and Amman-Zarqa basins), where a critical rate of the natural recharge likely occurs in Syria. Extra Syrian improvement of groundwater in these basins decreased the accessible safe yield to Jordan.

The Yarmouk River framework is the fundamental surface water resource. Given the extraordinary shortage of water resources in the locale, the significance of creating satisfactory water resources allocation procedures was recognized as early as the 1930s. In spite of the fact that no comprehensive agreement exists on sharing the jointly owned water resources, eleven plans for water utilization were arranged between the years 1939 and 1955. The final one was the Johnston Arrangement of 1955, which conducted a fair water-sharing plan between Jordan and Syria (World Bank, 2007).

The Peace Treaty which was signed in 1994 by Jordan and Israel guaranteed Jordan its right to an additional 215 MCM of water annually through new dams, diversion structures, pipelines, and a desalination/ purification plant. The ANNEX II of the Peace Treaty document, for Water and Related Matters contains seven articles which defined the allocation, storage, operation and maintenance, monitoring, water quality and protection, notification and agreement, and co-operation.

The agreement stipulates that during the summer period from May 15 to October 15 of each year, Israel shall receive 12 MCM, and Jordan is to keep the rest of the Yarmouk water flow. During the winter period, from October 16 to May 14 of each year, Israel is entitled to receive 13 MCM, and Jordan is to keep the rest of the flow. Furthermore, Israel is entitled to borrow an additional 20 MCM during the winter period, to be transferred back to Jordan during the next summer. With regard to excess flood waters from the Yarmouk that would otherwise flow into the Lower Jordan River, it was agreed that both Jordan and Israel are allowed to utilize this water in equal portions for their own purposes.

At the lower Jordan River, the agreement stipulates that during the summer period of each year, Jordan shall receive 20 MCM from the Lower Jordan River upstream of the Yarmouk from Israel. During the winter period, Jordan shall receive an additional 20 MCM from Israel from the LJR south of the Yarmouk. With regard to the remaining water flows in the LJR south of the Yarmouk, it was agreed that both Jordan and Israel are allowed to utilize this water in equal shares for their own purposes, provided that neither party would harm the water quality of the LJR. A Joint Jordanian – Israeli Water Committee has been established to monitor the actual water flows and water allocations.

In terms of saline springs and additional water resources, the agreement stipulates that Jordan is entitled to receive 10 MCM of desalinated water from Israel, originating from the saline springs near Lake Tiberias, provided that this is financially feasible. If so, it has been agreed not to discharge the brine into the LJR basin. Currently, this saline water is conveyed from these springs directly to the LJR through the Saline Water Carrier by Israel. The agreement confirms that Israel will explore the possibility of financing the operation and maintenance cost of supplying this desalinated water to Jordan, while Jordan will explore the possibilities to finance the required capital expenditures. Finally, the agreement includes the intension to jointly develop an additional 50 MCM of drinkable water, without yet specifying its source, for the benefit of Jordan.

Unfortunately, out of the 215 MCM, Jordan is already receiving between 55 and 60 MCM of water from across the border with Israel through a newly-built pipeline. Jordan is also entitled to build a series of dams on the Jordan and Yarmouk rivers to impound its share of flood waters. To this end, the Karama Dam in the Jordan Valley has been built to store 55 MCM of water, mainly from the Yarmouk, and its yield will be used to help irrigate some 6000 hectares in the southern Jordan Valley (Wardam, 2004; Royal Haskoning DHV, 2015).

5. Analysis of Water Demand and Supply

There is a huge gap between water demand and supply in Jordan, where the sustainable water supply is limited while the demand is rising rapidly. In 2017, the estimated water demand quantity for all sectors was 1412 MCM. Table 7 and Figure 6 show the quantities of water utilized by users from 1985 till 2017. It is apparent that most of the water is used by the agricultural sector through irrigation practices. Agriculture consumes about 53% of the total water supply; however, it accounts for 6% of Jordan's Gross Domestic Product (GDP) and 12% of this were natural products and vegetables. Around 10% of the labor force was utilized in agriculture. The Ministry of Water and Irrigation updated its strategies to hold agricultural water use at 700 MCM in the future, so a strong challenge will be to generate a greater deal of value by utilizing that amount of water

The irrigated cultivation potential in Jordan was evaluated at around 840,000 ha. Nevertheless, taking into account the possibly accessible water resources, the irrigation potential is around 85,000 ha, which also includes areas that are irrigated currently (MWI, 2008).

In spite of the fact that water system has been detailed in Jordan for an exceptionally long time, especially in the Jordan Valley, serious irrigation ventures have been executed since 1958 when the Government chose to redirect a portion of the Yarmouk River water and build the King Abdullah Canal. The Canal was 70 km long in 1961 and was expanded three times between 1969 and 1987 to reach the length of 110.5 km. The development of dams on the side channels and the redirection of the streams from other channels have permitted the advancement of irrigation over a huge region. At the same time, wells were bored in the Jordan Valley to abstract groundwater, for residential and irrigation purposes (MWI, 1997 and 1999):

Irrigation in the highlands relies on groundwater

resources. The irrigation system depends on wells which are from 100 to 5,000 m deep, which convey water to the agrarian lands (JICA, 1995). There are three types of irrigation development supporters in these regions:

- Private holders who have obtained credits from the Agriculture Credit Organization (ACC) for boring, pumps, and developing water system frameworks
- Bedouin-settlement water system ventures worked and kept up by the Service of Farming and the Water Authority
- Private companies working on large-scale ventures in the southeast of the country.

Figure 6 shows that the industrial use is almost stabilized due to low investments within the country; however, the main consumer, that is the agriculture sector, is flocculating by time depending on marketing windows. On the other hand, the municipal use is increasing tremendously indicating the urge needs to compensate for the fast population growth.

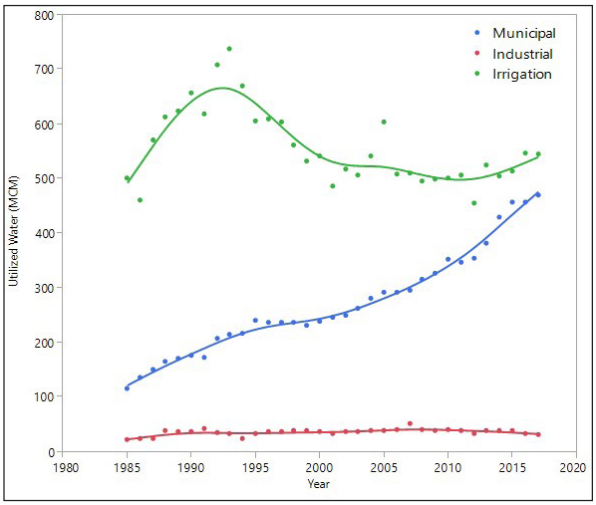

Figure 6. Quantities of water utilized by sector from 1985 till 2017.

Looking closely over the year 2016, the total water use was 1044 MCM, which went to supply the municipal, industrial, irrigation, and livestock demands by 43%, 3.1%, 52.4%, and 0.7% shares, respectively (Table 8). Most of the water supply is derived from groundwater (59%) followed by surface water (28%), while the non-conventional supply only provided 13% of the needs. This illustrates how much of the renewable groundwater is being depleted, while surface and non-conventional water supplies represent only minor gaps fillings. In addition, it is important to indicate that the estimated non-revenue water is 48% in 2017 compared to 43% in 2010; it is divided to more than 50% as administrative losses and less than 50% as physical losses from the networks.

Table 7. Recent and Anticipated water utilization in Jordan by division in MCM (MWI, 2013, 2015, and 2017).

Year	Municipal	Industrial	Irrigation	Total
1985	116	22	501	639
1986	135	23	461	619
1987	150	24	570	744
1988	165	39	613	817
1989	170	36	624	830
1990	176	37	657	870
1991	173	42	618	833
1992	207	35	709	951
1993	214	33	737	984
1994	216	24	669	909
1995	240	33	606	879
1996	236	36	610	882
1997	236	37	603	876
1998	236	38	561	835
1999	232	38	532	802
2000	239	37	541	817
2001	246	33	487	766
2002	249	37	517	803
2003	262	36	506	804
2004	281	38	541	860
2005	291	38	603	932
2006	291.4	40.5	508.6	840.5
2007	294.5	50.8	510.2	855.5
2008	315.7	40.5	495.6	851.8
2009	326.8	39.3	498.2	864.3
2010	352	41	500.8	893.8
2011	346.8	39.4	505.8	892
2012	353.8	33.9	454.8	842.5
2013	381	39.3	525	945.3
2014	429	39	504.3	972.3
2015	456.5	37.9	514.4	1008.8
2016	456.9	32.46	547.04	1036.4
2017	469.7	32.1	544.7	1046.5

Table 8. National Water Supply and Consumptive Use (MCM) by Sector for the year 2016

Row Labels	Municipal	Industrial	Irrigation	Livestock	Total Water Uses	Share%
1-Surface Water	**123.75**	**3**	**155**	**7**	**288.75**	**28%**
A. Jordan Rift Valley	101.86	3	89.16	0	194.02	
KAC	68.82	0	52.88	0	121.7	
Sothern Ghor &W. Araba	33.04	3	36.28	0	72.32	
B. Highlands	21.89	0	65.84	7	94.73	
Springs	20.41	0	21	0	41.41	
Base & Floods	1.48	0	44.84	7	53.32	
2. Treated Wastewater	**0**	**2.1**	**134.24**	**0**	**136.34**	**13%**
TW Registered in JV	0	0	101.12	0	101.12	
TW non-registered in HL	0	2.1	33.12	0	35.22	
3. Groundwater	**333.15**	**27.37**	**257.8**	**0.63**	**614.48**	**59%**
Renewable GW	211	23	231.11	0.63	465.47	
Nonrenewable GW	117.95	4.37	26.69	0	149.01	
Desalination	4.2	0	0	0	4.2	
Total Utilized Water Res.	**456.9**	**32.46**	**547.04**	**7.63**	**1044**	**100%**

6. Future Water Demands

Water strategy of Jordan (2007 and 2009) indicated that the total water use in 2015 amounted to 1400 MCM, which is probably less than the actual water use due to the partially uncontrolled abstraction of groundwater, in particular by agricultural farms in the highland areas. The recorded water use through agriculture amounted to 537 MCM in 2009, which is 61% of the total water used. Water for municipal uses was in the second largest position with about 34%, while the industry and tourism sectors consumed the remaining 5%.

Municipal water use comprises domestic water use at the household level and water for services, such as commerce, health, education, workshop, governmental offices, and communal green spaces. This sector receives water through the public water network which is managed by the WAJ and Jordan's three public utilities. The total municipal water use is expected to increase to about 730 MCM in 2020 according to Jordan's water strategy, and is expected to increase to 778 MCM in 2025 (Table 9).

Industrial water use includes both industries that do not receive their water from public water networks and industries with their own water wells. Groundwater comprises about 90% of the main sources of water used for industry. Industrial water use increased sharply over the last decade up to 50 MCM in 2015, but the annual growth rates differ considerably.

Jordan's Water Strategy estimated water requirements for oil-shale and nuclear-power industries to reach about 25 MCM in 2020. The projections by the MWI predicted industrial water use at 70 MCM in 2025.

Apparently, Jordan is directly over-exploiting its water resources by between 10% and more than 100%. Water levels are dropping, groundwater resources are being mined, salinization and salt-water interruption are watched, and the household water supply does not reach satisfactory measures.

The increasing cost of water supply is adding to the large burden of the fiscal budget in terms of new capital expenditure and subsidy needs. The gap between current tariff levels and full cost recovery is too big to be bridged by tariff increase alone. Full cost recovery is too expensive for the majority of water users, especially for low-income residents. Thus, prospects of reducing water subsidies are very likely.

Water deficits will continue to grow, and the gap between demand and supply will lead to an increase in bulk water supply costs for priority domestic use from the average current levels of 0.35 JD /cubic meters to 0.95-1.10 JD /cubic meters or even more.

Table 9. Future Water Demand over the Period 2020-2025 (MWI, 2016)

Year	2020	2021	2022	2023	2024	2025
Municipal, Industrial, Tourist demands	730	737	746	755	766	778
Irrigation demand	700	700	700	700	700	700
Oil shale and Nuclear power demand	25	48	48	48	70	70
Total Demand	**1,455**	**1,485**	**1,493**	**1,503**	**1,536**	**1,548**
Deficit in MCM/a	**(373)**	**(320)**	**(256)**	**(252)**	**(283)**	**(88)**

7. Water Management Options

Several policies, strategies and plans have been developed by the government to enhance the development, management, and use of water resources. Jordan's "Water for Life" strategy 2008–2022 highlights the future challenges to be addressed through proper policies and regulations. The following are some of the adopted and suggested options:

7.1 Water Harvesting

Rainwater is the prime source of water in Jordan. The quantities lost to evaporation from temporary open water bodies and soils represent a significant part of the water budget in Jordan. Rainwater is dispersed over a wide area and, if properly collected, could provide a significant addition to the water reserves of the country. The simple model of rooftop water harvesting shows that the average design-rainfall is about 400 millimeters per year, and the losses are about 20%. A rooftop of 100 square meters can easily harvest 32 cubic meters per year. On the other hand, flood water harvesting at macrocatchments can collect considerable amounts of water in small dams across intermittent rivers and Wadis. Furthermore, micro-catchment water harvesting is widely implemented in the study area. Example techniques include earth and stone bonds, terraces and pots. The observed storage media include soil, tanks, underground cisterns, small check dams and one large dam which is the King Talal Reservoir (KTD).

The government of Jordan has tried to harvest each drop of rain as much as possible through constructing large dams with a total capacity of 335 MCM (Table 10), and other micro water-harvesting projects such as desert dams, earth ponds, and concrete ponds (Table 11). The harvested water is being used for irrigation purposes followed by municipal use

Table 10. Water harvesting dams in Jordan up to the year 2017.

Dam	Design Capacity (MCM)	Total Inflows (MCM)	Total Outflows (MCM)	Storage End of 2017 (MCM)
Wehdeh	110	72.957	93.658	4.063
Wadi Arab	16.8	0.58	11.277	3.52
Zeqlab	4	0.488	0.361	0.371
Kufranjeh	7.8	1.158	1.165	0.857
King Talal	75	115.809	141.791	28.215
Karameh	55	1.694	6.213	13.837
wadi Shueib	1.4	6.396	7.344	0.472
Kafrain	8.5	10.134	10.913	2.443
Wala	8.2	1.57	7.938	0
Mujeb	29.8	1.357	6.328	2.917
Tanour	16.8	7.014	20.674	5.425
Karak	2	0.437	0.281	0.156
Total	**335.3**	**219.594**	**307.943**	**62.276**
Percentage of storage from design capacity	**18.6%**			

Table 11. Micro-scale water harvesting projects in Jordan up to the year 2017.

Water Harvesting type	Count	Design Capacity (MCM)
Desert Dams (Constructed)	61	88.715
Desert Dams (Under Construction)	1	0.05
Concrete Ponds	65	0.295
Earth Ponds (Constructed)	223	22.122
Earth Ponds (Under Construction)	11	0.525
Total	**361**	**111.707**

7.2 Brackish Water and Desalination

Brackish water for direct use or after desalination appears to offer the highest potential of non-conventional means for augmenting the country's water resources. Several brackish springs have been identified in various parts of the country. Tentative estimates from the MWI of stored volumes of brackish groundwater for the major aquifers suggest immense resources, but not all of these quantities will be feasible for utilization. Accordingly, when referring to the statistics of brackish water, the quality, quantity and location of this resource need to be carefully studied in order to assess its potential for utilization.

Modern desalination technologies applied to brackish water offer effective alternatives in a variety of circumstances. In 2015, there were fifty-two private desalination plants operated by farmers to desalinate brackish water for irrigation purposes desalinating about 10 MCM annually. Brackish water having salinity between 2,000 and 8,000 ppm is pumped from wells of depths between 100 and 150m. The facilities are generally in operation for 24 h/d in summertime and for 8 h/d in wintertime. The only energy source used to run the plants is electric power. Desalinated water is mixed with freshwater, whereby the mixed water has salinity of about 650 ppm. Irrigation water is applied in particular for bananas being a crop of a high market value.

Moreover, there are forty-four public desalination plants and ten other ones under construction to desalinate about 80 MCM annually. All these plants are run or will be run by

WAJ to treat saline water for the supply of drinking water. The units are all of a small size compared to the plants in the Gulf Region.

7.3 Public Investments

Huge investments from public and private sectors regarding the supply of water have been witnessed in the past decades. This has been manifested in the development of public desalination facilities for municipal use and micro and small private desalination facilities for drinking water and agricultural use including the extraction of fossil freshwater from aquifers shared with Saudi Arabia, the exploration of very deep (1,000–2,000 meters) sources of brackish water for eventual desalination,and the study of options for Red Sea- Dead-Sea conveyance to reduce the decline of the Dead Sea level and provide desalinated seawater for municipal and industrial use. The cost of new urban bulk water supply to Amman is expected to exceed US$1.35 per cubic meter as in the case of the Disi-Amman Water Conveyance Project.

The Conveyance of Disi project, completed in 2013, provides around 107 MCM annually of the drinking water to Amman and other middle and northern governorates. However, water that is being used for irrigation is reduced to start supplying the 107 MCM. This source is considered to be almost the major remaining conventional water source that can be utilized for drinking water.

Also, there are private investments in WWTPs especially for As-Samara WWTP. The plant at first utilized the stabilization-lake innovation, but was revamped utilizing the actuated slime innovation in 2008. In 2012, another development occurred that is the increment of the treatment plant to a capacity of 365,000 cubic meters. Treated water is reused basically for irrigation in the Jordan Valley and the highlands, and for restricted businesses, and will be utilized for creating vitality in the future.

7.4 Rational Water Use

The MWI issued a Water Demand Management Policy in 2016. The main objectives of the water-demand management policy, which was approved by the Cabinet in 2008,are: to maximize the utilization of the available water, minimize water losses, conserve water resources, promote effective water use efficiency, to adapt with the challenge of water scarcity in order to reduce the gap between supply and demand (i.e. increase the efficiency of water use to meet water needs of this sector in all regions of the country). This policy also includes construction, standards and specifications, reduction of non-revenue water, reducing water losses, non – conventional water resources, water conserving landscaping, substitution and re-use for irrigation, efficient use of water in irrigation, and water harvesting at the farm scale.

7.5 Red-Dead Sea Project

The Red Sea–Dead-Sea Conveyance Project, sometimes called the Two Seas' Canal, is a planned pipeline that runs from the coastal city of Aqaba by the Red Sea to the Lisan area in the Dead Sea. It will provide potable water to Jordan, Israel, and the Palestinian territories. Also, it will bring water with a high concentration of salts resulting from the desalination process (reject brine) to stabilize the Dead Sea water level, and generate electricity to support the energy needs of the project. The project is going to be carried out by Jordan, and is entirely within Jordanian territories. The project will be financed by the governments of Jordan, Israel, and a number of international donors.

The proposed conveyance would pump seawater 230 meters uphill from the Red Sea's Gulf of Aqaba through the Arabah Valley in Jordan. The water would then flow down gravitationally through multiple pipelines to the area of the Dead Sea, followed by a drop through a penstock to the level of the Dead Sea near its shore, and then through an open canal to the Sea itself, which lies about 420 meters below sea level. The project would utilize about 225 km of pipelines for seawater and brine, parallel to the Arabah Valley in Jordan. The project would also have about 178 km of freshwater pipelines to the Amman area. It also would include several water desalination plants and at least one hydroelectric plant. In its final phase, it would produce about 850 million cubic meters of freshwater per year.

The project would require electric power from the Jordanian power grid, but it would also provide some electricity through hydroelectric power. In sum, this project would probably be a large net-user of energy. The net power demand would have to be satisfied through other power projects whose costs are not included in the project costs. The Kingdom of Jordan plans to build a large nuclear power plant that might make up the difference.

After stumbling for years due to this project's complex nature and huge funding requirements, the MWI announced that Jordan is moving ahead with the first phase of the Jordanian version of the Red Sea–Dead Sea Project. The plan is to draw water from the Gulf of Aqaba at the northern tip of the Red Sea, and transfer it north to the Araba Valley where a desalination plant will be built. Another pipeline will extend from the plant to the Dead Sea. The new project is estimated to cost some $980 million, of which the government plans to secure some $400 million in grants. This project will also provide hundreds of jobs.

7.6 Institutional Environment

The ministries/institutions included in the water division in Jordan include:

1. The Ministry of Water and Irrigation (MOWI), with the Water Authority of Jordan (WAJ) and the Jordan Valley Authority (JVA) as its operational entities
2. The Ministry of Agriculture
3. The National Center for Agricultural Research and Technology Transfer
4. The Ministry of Municipal Affairs
5. The Ministry of Environment

8. Discussion and Recommendations

There is a need for the development of dams and water system projects in the Jordan Valley in order to maximize the utilization of surface water resources some time recently to prevent water from being wasted in the Dead Sea. Restricted extra-undiscovered surface water resources could be created in the Jordan Valley side channels and in the Mujib, Zarqa, Ma'an, and Zara basins.

Future patterns in irrigation are connected to water improvement conceivable outcomes. Aquifers in the Disi-Mudwara, Jafer, and Hamad regions are prime new water sources, which are capable of supplying an extra 100 MCM/year of water for a long time. Full utilization of

these resources would require satisfactory administration to maintain a strategic distance from salinization and to decrease extraction from over-utilized aquifers.

The following activities are expected to handle this urgent situation:

- Desalinization of ocean water (Read-Dead-Sea Canal).
- Reduction of water requested for irrigation

Drinking water quality in Jordan is controlled by the Jordanian Drinking Water Standards, which are based on the World Health Organization drinking water rules. For the reason of observing groundwater quality, an organizer of observation wells is introduced in each of the groundwater basins. Level water is put away in water tanks (more often than not on roofs of buildings) to be utilized until the next turn of water supply.

The limited water resources are exposed to contamination. Also, population growth is expected to increase the pressure on accessible water resources. Moreover, the problematic issue of displaced people has caused the amount and quality of the water resources framework in Jordan to deteriorate, particularly in the north.

Farming accounts for 63% of water demand, while the residential share is 32% and the use by animals and businesses are only 1% and 4%, respectively (Figure 4). The water shortages are caused by water needs in agriculture. The Jordan water procedure plans to expand water supply through three measures:

- More utilization of treated water in farming and industry,
- An increment of fossil groundwater utilization through the Disi Water Conveyance Extension
- The desalination of seawater as part of the Red-Sea-Dead-Sea Canal (500-600 MCM/year).
- The hotspots of water procedures in Jordan are:
- To ensure surface and groundwater resources by cautious management of their use.
- To make great strides in the effectiveness of the administration of both urban water and water system.
- To create an organizational capacity capable of overseeing water resources, backed by an administrative system.
- To include the private sector in the advancement of utilities for effective water utilization and great monetary administration structures.
- To present a socially satisfactory duty framework which might change the situation of depending upon the nature of water utilized (e.g. household, mechanical, water system, etc.) or the type of water (e.g. surface water, groundwater, recovered wastewater).

Jordan's momentous development accomplishments are at risk due to the devastating water shortage, which is expected to become worse by climate change. Precipitation is anticipated to decline essentially, and dissipation and transpiration of plants will increase due to hikes in temperatures.

Jordan's water resources are found to be distant from its population centers, in particular in the Greater Amman region where nearly half of the country's population lives, and which lies at around 1,000 meter over the sea level. To address this challenge, Jordan has created a broad water supply framework to provide water for both irrigation and metropolitan employments. The key components of Jordan's water resources are:

- Al Wahda Dam on the Yarmouk River
- King Abdullah Canal (KAC) in the Jordan Valley which is nourished essentially by the Yarmouk Waterway, the Mukhaibah springs close to the Yarmouk Waterway, and a number of water courses depleting into the Jordan Valley
- As-Samra wastewater treatment plant which treats most of Amman's wastewater releasing it into the Zarqa Waterway
- The King Talal Dam on the Zarqa Waterway from which water returns to the KAC downstream of Deir Alla for irrigation in the Lower Jordan Valley

The percentage of non-revenue water (NRW) - water that is produced but is not discharged to consumers- was evaluated at 44% in 2008. The fundamental reasons driving to this big loss rate are leakage, water passing through meters, illegal connections, unreliable water meters and issues concerning the perusing of those meters.

Measures to diminish the rate of NRW can in this way contribute to relieving the big pressure on water resources. In Amman, the level of non-revenue water has been decreased from an estimated 46% in 2005 to an assessed 34% in 2010. However, during the same period, the normal hours of benefit per week declined from sixty-six hours to thirty-six hours. Water and sewer administrations in Jordan are intensely subsidized. The income covers part of the operation and support costs. The tax framework is an increasing-block framework, beneath which clients pay a higher tax per cubic meter in the event that they expend more water.

Jordan is suffering from serious dry seasons, and while climate change is an issue, the political climate in the Middle East is making things worse. The Jordan River has lost 95% of its characteristic stream since its redirection. Syria and Israel and have built dams along the banks of the stream of the Jordan River and its tributaries (USAID, 2009).

The major challenges facing Jordan in the field of water resources are:

- Desalination is exceptionally vital, but is seriously and subsequently an expensive undertaking. On one side, the capital costs have to be prepared and on the other side, with the current water duties, the essential appropriation of funds will put an overwhelming burden on the national budget.
- Necessary energy generation for large-scale desalination must be available.
- Possible negative natural impacts of expansive desalination ventures need to be moderated.
- The restriction of brackish water resources.
- Lack of skill in Jordan in the field of desalination.
- Use of treated wastewater needs to be carefully checked through a comprehensive hazard-administration framework.
- Greywater and storm water collection systems and treatment frameworks at both the building level and the metropolitan level should be available.

9. Conclusions

In addition to loose water governance in the form of lax enforcement of rules and regulations, the lack of equity and transparency, has resulted in the continuous mining of renewable groundwater resources, with the current extraction rate (50 %) exceeding the safe yields, increasing water salinity, declining water table levels, and increasing pumping costs. The efficient management of scarce water resources is an existential necessity. It is critical to the livelihoods and well-being of Jordan's people and essential to the country's lasting stability. In the absence of securing its water assets, the risks for Jordan will include near-term economic slowdowns, health hazards, social disruptions, and serious conflicts over water resources.

The water sector has gone through significant phases marked by the various challenges imposed by the tremendous growth of population, as well as the rising living standards, and the economic and social development. In spite of that, more than 98% of the Jordanian people are connected to safe-water supply services, while more than 63% are covered by sanitation services. This percentage is expected to increase up to 70% in the coming years through various programs and plans implemented by the Ministry of Water and Irrigation (MWI). Interrupted pumping and the non-reliability of water supply services are common across Jordan. The connection rate does not reflect the fact that many urban and rural communities do not receive piped water for weeks.

However, despite the Government's efforts to manage the limited water resources and its relentless search for alternative supply, the available water resources per capita are falling as a result of population growth. Government's attempts to deal with the scarcity problem focused not only on supply augmentation and supply management, including rationing of water service, but also on demand-management measures, and the adoption of a public information policy. Despite all measures, the coming scarcity problem will remain a major challenge facing water managers and the country at large.

There are clear gaps related to the levels of public awareness, participation in water protection programs, the construction of a comprehensive legal framework for water management, and sectoral priorities for water conservation. Additional methodologies for sustainable water solutions are required such as a reliable data bank, proper research, funding support, and training programs.

The utilization and careful use of water resources require integrated management policies to ensure the sustainability of water and the environment. The existing water policy and by-laws seem to be well focused on the issues. However, there is a lack of enforcement and sustainability.

Among all the detected methods to overcome the water scarcity in Jordan, the Red-Dead Sea project has become the only sustainable solution for ensuring the survival of Jordan's future generations.

References

ABABSA, Myriam (ed.). Atlas of Jordan: History, Territories and Society. New edition [online]. Beyrouth: Presses de l'Ifpo, 2013 (generated 24 September 2019). Available on the Internet: <http://books.openedition.org/ifpo/4560>. ISBN: 9782351594384. DOI: 10.4000/books.ifpo.4560.

AFD and CMI (2011). Jordan water demand management study. Final report. Prepared for the Ministry of Water and Irrigation of Jordan (MWI), supported and funded by the French Development Agency (AFD / FDA).

Al-Hadidi, M., and Al-Kharabsheh, A. (2015). Effect of Overpumping on Water Quality Deterioration Deterioration in Arid Areas: A Case Study of Dead Sea Basin/Jordan, Jordan Journal of Agricultural Sciences, 11(1), University of Jordan, Amman, Jordan.

Al-Kharabsheh, A. (2013). Effect of Arab Spring on Water Crises Management in Jordan (Arabic), UNESCO, 24, Amman, Jordan.

FAO (1995). Water Resources, Development and Management Service, MENA Regional study report, 1995.

GTZ (1995). Deutsch Gesellschaft Technische Zusammenarbeit, Regional Study on Water Supply and demand Development, phase I, Ministry of Water and Irrigation, Amman, Jordan.

GTZ (1999). Deutsch Gesellschaft Technische Zusammenarbeit, Regional Study on Water Supply and demand Development, phase III, Final Report, Ministry of Water and Irrigation, Amman, Jordan.

GTZ (2004). Deutsch Gesellschaft Technische Zusammenarbeit, Water Master Plan, Ministry of Water and Irrigation, Amman, Jordan.

JICA (1995). Japan International Cooperation Agency, The Study on Brackish Groundwater Desalination in Jordan, Tokyo-Japan.

MoEnv (2014). Jordan's Third National Communication on Climate Change. Submitted to The united nations Framework Convention on Climate Change (UNFCCC), funded by GEF and UNDP," Ministry of Environment, Amman, Jordan, 2014.

MoEnv (2015). National Strategy and Action Plan to Combat Desertification 2015-2020. Ministry of Environment, Amman, Jordan.

MWI (1997). Ministry of Water and Irrigation, Jordan's Water Strategy, Amman, Jordan.

MWI. (1999). Ministry of Water and Irrigation, Annual Report 1999. Amman, Jordan

MWI (2007). Water Strategy of Jordan 2008-2022. Amman, Jordan

MWI (2008). The Plan for the Response to Water Challenges, Ministry of Water and Irrigation Archived from the original on 2008-02-29. Retrieved 2008-03-11, Jordan.

MWI (2009). Water for life: Jordan's water strategy, 2008-2022, Amman, Jordan.

MWI (2013). Structural Benchmark-Action plan to reduce water sector losses. www.mwi.gov.jo/sites/enus/Hot%20Issues/MWI%20Action%20Plan%20To%20Reduce%20Losses%20in%20Water%20Sector%20(Financial%20Effeciency%20Enhancement).pdf

MWI (2014). National Strategic Wastewater Master Plan Report, Minsitry of Water and Irrigation, Amman, Jordan.

MWI (2016). National Water Strategy 2016-2025: Water Demand Management Policy. Ministry of Water and Irrigation, Amman, Jordan.

MWI (2017). Jordan Water Sector Facts and Figures. Ministry of Water and Irrigation, Amman, Jordan.

Royal Haskoning DHV (2015). National Master Plan for the Jordan River Valley. Royal Haskoning DHV in partnership with MASAR Center Jordan for SIWI - Stockholm International Water Institute, GNF - Global Nature Fund and EU - SWIMP, April, 2015.

UNICEF (2006). Joint Monitoring Programme for Water

Supply and Sanitation, Coverage Estimates Improved Drinking Water, Archived from theWorld Health Organization; original on 2007-10-05. Retrieved 2008-03-07.

USAID (2009). USAID Telling Our Story: Jordan - Bringing Fresh Water to the People. United States Agency for International Development Retrieved 2009-03-12.

WAJ Files, Water Authority of Jordan Files, Amman, Jordan.

Wardam, B. (2004). More politics then water: Water rights in Jordan, IUCN Regional Water Programme in West Asia and North Africa, Jordan, Global Issue Papers, Heinrich Böll Foundation, 2004.

World Bank (2007). Implementation Completion and Results Report (Ibrd-44450) On A Loan in the Amount of US$55.0 Million to the Hashemite Kingdom Of Jordan for the Amman Water And Sanitation Management Project. Retrieved 2009-09-28.

JJEES

Jordan Journal of Earth and Environmental Sciences

JJEES (2020) 11 (1): 49-61
ISSN 1995-6681

A Review of Gravity and Magnetic Studies in the Jordan Dead Sea Transform Zone

Radwan El-Kelani

An-Najah National University, Faculty of Engineering and Information Technology, Department of Civil Engineering, Palestine

Received 1 July 2019, Accepted 29 October 2019

Abstract

The geodynamic evolution of the Dead Sea Transform (DST) remains one of the most contentious issues of the eastern Mediterranean tectonics. Therefore, wide-ranging geophysical surveys have been carried out over five decades to fill the gap of geological information existing in the region. The collected data sets allowed new models to be constructed, improving the knowledge of the crustal and lithospheric structure of the DST, and the reformulation of its complex tectonic history. In this context, the contribution of gravity and magnetic investigations deserves, with no doubt, a review on both large and small scales. The potential data were employed to interpret the evolution of the Dead Sea basin, delineating the crustal and upper mantle structure and modelling the density distribution of the sediments. The crystalline basement structure and magmatic intrusions were investigated, and underground structures of salt diapirs were explained and sinkhole hazards were detected along the Dead Sea coast. In order to produce the first comprehensive compilation of gravity and magnetic studies in the Jordan DST zone, all available potential field data were combined and revised. The main features of the potential fields resulting from these surveys were described, and the qualitative and quantitative interpretations proposed by several authors were abridged. The information presented by this paper will help interested geoscientists, in different geological fields, with their regional and local studies in the Jordan DST zone region. The compilation of geophysical observations presented here may also facilitate the understanding of similar transform systems elsewhere.

Keywords: Dead Sea Transform, gravity data, magnetic data, gravity and magnetic anomaly fields, interpretative models.

1. Introduction

The Dead Sea Transform, also known as the Dead Sea rift, is a major continental fracture zone that separates the Arabian plate and the Sinai- Palestine plate (Figure 1). It extends over a distance of more than 1000 km, linking the Zagros-Taurus convergence zone in the north with the Red Sea in the south, where seafloor spreading takes place (Garfunkel, 1981). The geology and tectonics of the transform fault are largely affected and controlled by the geodynamic processes acting in the Red Sea region which have resulted in its opening (Girdler, 1990 and references therein). Continental transform faults, such as the Dead Sea fault system, involve complex structural and sedimentary regimes related to the active transform displacement along fault segments (Garfunkel and Freund, 1981; Kashai and Croker, 1987; Ben-Avraham and ten Brink, 1989; Beydoun, 1999; Smit et al., 2009; Ben-Avraham and Katsman, 2015).

Integrated geophysical methods are important approaches to study the distribution of rocks, to identify their types and to determine the associated structural features. Past potential field investigations, especially gravity and magnetic methods of the Jordan DST zone, have contributed significantly to understanding the structural framework and lithologies of the region and indicate a complex tectonic history. They were important tools for giving a geological picture about the subsurface structure and the geometry of the DST pull-apart basins (Ginzburg and Ben-Avraham, 1986; Frieslander and Ben-Avraham, 1989; Batayneh, et al., 1995; Ben-Avraham et al., 1996; ten Brink et al., 1993, 1999; Ben-Avraham and Schubert, 2006; Eppelbaum et al., 2007; Segev et al., 2018) the depth of basement, the dimensions of magmatic intrusions, and volcanic centres (Folkman and Bein, 1978; Folkman and Ginzburg, 1981; El-Isa and Kharabsheh, 1983; Gvirtzman and Weinberger, 1994; El-Kelani et al., 1998; Rybakov et al., 1999b; Segev et al., 1999; Rybakov et al., 2000; Eppelbaum et al., 2004; Rybakov and Segev, 2004; Tašárová et al., 2006; Rybakov et al., 2011; Segev and Rybakov, 2011; Schattner et al., 2019).

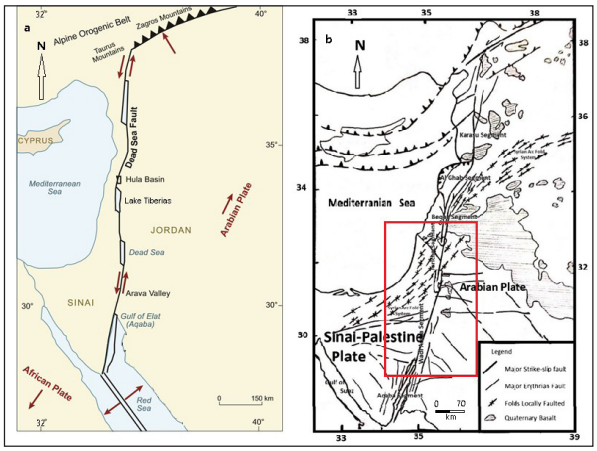

Figure 1. a. Map of the DST showing general relative plate motion from the opening of the Red Sea in the south to the Zagros-Taurus Mountains in the north (modified after Ben-Avraham et al., 2008). **b.** Regional tectonics of the Jordan Dead Sea Transform zone (modified after El-Isa, 2017), the red rectangle indicates the study area of this work.

* Corresponding author e-mail: radwan@najah.edu

Also, the potential data were employed in for modelling the crustal and upper mantle structure, and the lateral and depth density distributions in the crust (Ginzburg and Makris, 1979; Folkman, 1981; ten Brink et al., 1990; Hofstetter et al., 2000; Al-Zoubi and Ben-Avraham, 2002; Götze et al., 2002; El-Kelani, 2006; Segev et al., 2006; Al-Zoubi, 2007; Götze et al., 2007). Potential data were also employed in the investigations of the spatial distribution of salt diapirism and also in the identification of underground salt structures in the entire Dead Sea basin (Neev and Hall, 1979; Al-Zoubi and ten Brink, 2001; Choi et al., 2011). Moreover, data were used in the identification of sinkhole development and for the estimation of the dissolution karst and the detection of caves in salt formations along the Dead Sea coast (El-Isa et al., 1995; Closson et al., 2005; Rybakov et al., 2001, 2005; Eppelbaum et al., 2008; Shirman and Rybakov, 2009; Ezersky et al., 2010, 2013). On the other hand, gravity and magnetic investigations were important for delineating sedimentary basin geometry during the early stage of petroleum exploration as an indication of potential hydrocarbon bearing structural anomalies (Rybakov et al., 1995b, 2000, 2009; Hassouneh, 2003; Eppelbaum and Katz, 2011).

The literature review of the previous gravity and magnetic works, conducted throughout the years in the transform region, showed that most of them have integrated the interpretations of both potential fields, at the local and regional level, onshore and offshore. The gravity and magnetic investigations are distributed on three main sectors of the Jordan DST zone, which represents the main structural segments of the transform fault including the Gulf of Aqaba segment followed by Wadi Araba, in the south, the Dead Sea in the middle, and the Jordan valley in the north (Figure 1b). This paper reviews these earlier potential field studies, available for the Jordan DST zone, and considers the regional and local geological, structural and tectonic development of the study area and their interrelationships. Interested geoscientists may find this information useful for their future work, especially concerning the Dead Sea Transform region.

2. Regional geological setting

The development of the DST went through folding, faulting, rifting, uplifting, offset, and volcanic activity on a regional scale, where the Precambrian basement outcrop is on the surface in the southwest but is deeply buried in the northeast beneath the Dead Sea basin sediments. The Precambrian basement was shaped by the late Proterozoic Pan African orogeny (Figure 2). Afterward, the region became a stable platform on which sediments of continental and of shallow water marine origin were deposited during several periods from the Cambrian to the Early Cenozoic. Rifting was the main tectonic event in this period, shaping the Mediterranean continental margin in the Early Mesozoic (Garfunkel, 1988, and references therein). Mild folding and faulting expressing compression started from Pre-Jurassic to Oligocene-Miocene by forming the Syrian arc fold system, which extends from southern Syria to northern Sinai creating an S-shaped fold belt that is crossed by the transform fault, and followed by forming the Erythrean fault system, which consists of E-W and NW-SE trending faults (Garfunkel, 1981).

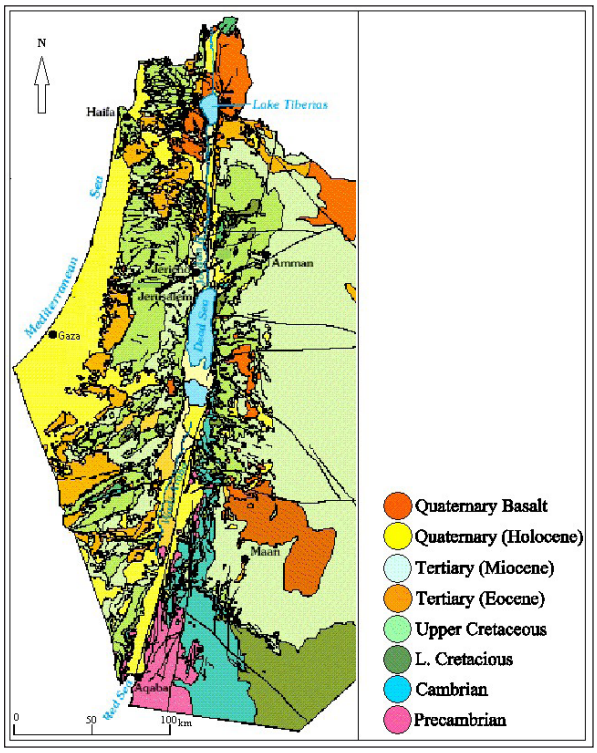

Figure 2. Geological map of the study area (USGS open report, overview of Middle East water resources, 1998).

During the Middle Cenozoic, a deformational phase resulted in the creation of N- and NNE-trending strike–slip faults forming the DST (Figure 1b). Some of these faults are arranged en-echelon, resulting in the creation of rhomb-shaped, pull-apart basins (Freund et al., 1970; Garfunkel, 1981; Aydin and Nur, 1982; Garfunkel and Ben-Avraham, 2001; Ben-Avraham et al., 2008).

The multi-stage volcanic activities and magma intrusion resulted in widespread igneous rocks along the continental transform margin. The impact of the fault systems on the volcanic activity show the relation between the spatial distribution of the igneous rocks and tectonic changes of the DST (Mimran, 1972; Sass, 1980; Gvirtzman and Sreinnitz, 1983; Dvorkin and Kohn, 1989; Garfunkel, 1989; Segev and Rybakov, 2010; Ibrahim et al., 2014; Griffin et al., 2018). Geological field observations, enhanced by geophysical evidence, show that there are matchable numerous markers between the geologies of areas facing each other across the DST which indicates a left-lateral movement of c. 107 km (Quennell, 1958, 1959, 1984; Girdler, 1990).

3. Gravity and magnetic surveys in the Jordan Dead Sea Transform zone

3.1 Gravity surveys

Significant gravity data were collected in the Dead Sea Transform region, mainly by the Natural Resources Authority (NRA) in Jordan and the Geophysical Institute (GII), at different scales in time and space. In total, approximately 100,000 gravity stations (Figure 3), covering the DST region and its eastern and western plateaus, were homogenised (Hassouneh, 2003; Götze et al., 2007, 2010b; Rosenthal et al., 2015). They are fairly and uniformly spaced

with a station spacing ranging between 0.5 and 2 km; gravity points' distribution in the study area is shown in Figs. 3a and b. Bouguer gravity values were compiled according to standard procedures, using the 1967 Geodetic Reference System and the standard density of 2670 kg/m. Sea level was taken as the reference datum and the terrain corrections were calculated up to Hayford zone O2 (167 km), using a digital terrain model with a 25 m grid. The overall accuracy of the station complete Bouguer anomaly values are estimated to be 0.1 to 0.8 mGal.

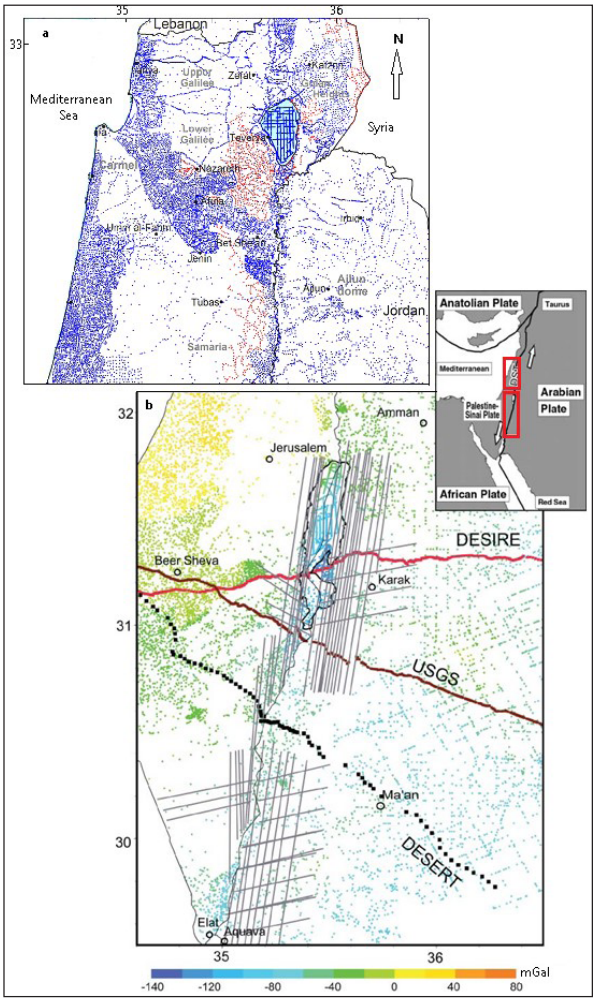

Figure 3. a. Coverage of gravity stations in the northern part of the Jordan DST zone. Red dots indicate new stations collected from 2009 to 2013 (Rosenthal et al., 2015); blue dots are previous gravity stations compiled from different sources (Ben-Avraham et al., 1996; Rybakov et al., 1997; ten Brink et al., 1999; Rybakov and Al-Zoubi, 2005). **b.** Map showing survey flight lines (grey) and the locations of terrestrial points (green, yellow, and light blue) of gravity data in the central and southern parts of the Jordan DST zone in the study area. The flights (Götze et al., 2010b) cover gaps in terrestrial gravity data (ten Brink et al., 1993; Hassouneh, 2003; Götze et al., 2007), mainly on the eastern side of the Dead Sea basin. The blue lines represent gravity profiles at the surface of the Dead Sea. Three wide-angle and refraction seismic profiles are shown: Dead Sea Integrated Research (DESIRE), line in red (Mechie et al., 2009); Dead Sea Rift Transect (DESERT), stippled line (Weber et al., 2009); and the U.S. Geological Survey (USGS) profile (ten Brink et al., 2006).

The data include regional land-based gravity point measurements (Rybakov et al., 1997; ten Brink et al., 1999; Hassouneh, 2003; Rybakov and Al-Zoubi; 2005; Rosenthal et al., 2015). Further gravity data collection has been conducted onshore at the Sea of Galilee (Ben-Avraham et al., 1996) and the Dead Sea (ten Brink et al., 1993). Other local gravity surveys were carried out in the Jericho area (El-Kelani, 2007), and in Wadi Araba (Götze et al., 2007). To provide a complete picture of the gravity field in the Dead Sea region, a high- resolution aerogravity campaign was conducted to cover gaps in terrestrial gravity data coverage, mainly on the Jordanian side (Götze et al., 2010b).

3.2 Magnetic surveys

For an integrated analysis of poetical fields and a better understanding of the geological settings in the DST region, magnetic surveys were conducted in the transform region and its shoulders. In the fall of 1979, a total of 54,185 km of aeromagnetic data were flown by Phoenix Corporation contracted by the NRA of Jordan. In total, 378,622 aeromagnetic stations have been measured to produce the total field aeromagnetic anomaly map of Jordan, which covered central parts of the transform fault zone and its eastern plateau (Phoenix Corp., 1980). Doppler navigation was employed in addition to visual navigation through the use of topographic map flight strips, airborne magnetometer (Geometrics Model G803) proton precession magnetometer with sensor mounted in a tail stinger. The magnetometer resolution was 0.5 gammas with a sampling interval of 1.0 second. Depending on the topography, the flight heights varied between 1.5-2.0 km above sea level; flight-line spacing of these surveys was in the range of 1-2 km (Hassouneh, 2003).

Aeromagnetic surveys had been also carried out in the western central parts of the DST zone and its plateau (Domzalski, 1967; Folkman, 1970; Folkman and Yuval, 1976; Rybakov et al., 1999b; ten Brink et al., 2007). A High Resolution, low altitude Aeromagnetic (HRAM) survey was carried out in 2003 in southern Wadi Araba (Al-Zoubi et al., 2004). Additionally, local scale magnetic ground surveys were carried out in specific geological areas to reliably estimate the depth and geometry of the causative magnetic bodies, and to identify their composition (Ben-Avraham et al., 1980; Ginzburg and Ben-Avraham, 1986; Frieslander and Ben-Avraham, 1989; Segev et al., 1999; Shirman, 2000; Khesin et al., 2005; Rybakov et al., 2009; Schattner et al., 2019). In 1998, the digital set of aeromagnetic data for the two divisions of the Jordan DST zone were compiled from several published surveys (Hassouneh, 2003). However, as mentioned before, the aeromagnetic data measurements over Jordan were collected at different elevations. The data, therefore, were numerically up-warded to a constant elevation of 2 km in order to avoid problems in the interpretation.

4. Features of the gravity and magnetic anomaly fields

The continuous updating of gravity and magnetic data in the DST region produced different versions of the Bouguer and magnetic anomaly maps, followed by several studies, over several years, dealing with the qualitative interpretation of the gravity and magnetic anomaly fields of the region (Woodside and Bowin, 1970; Folkman and Yuval, 1976; Folkman and Bein, 1978; Ginzburg and Makris, 1979; Folkman, 1981; Kovach and Ben-Avraham, 1986; Hassouneh, 2003; El-Kelani, 2006, 2007; Götze et al., 2007; Rybakov et al., 2011; Schattner et al., 2019). Qualitative interpretations were conducted in order to reveal the characteristic features

of the objects under investigation, their spatial location, and preliminary geological identification. To enhance the various frequency components of the magnetic and gravity fields, a variety of filtering techniques were employed. Gravity first and second derivatives for the residual Bouguer were calculated in order to highlight fault patterns bounding the Dead Sea basin and Lake Tabeires (ten Brink et al., 1993; Segev and Rybakov, 2011). Horizontal gradient analysis of the gravity field was applied for the definition of discrete border of causative bodies at depth in order to study the deep structure of the Carmel fault zone (Achmon and Ben-Avraham, 1997). An isostatic regional gravity field of the southern transform region has been calculated, enhanced by curvature analysis of the local features in the isostatic residual gravity field, which are caused by near-surface density inhomogeneities (Hassouneh, 2003; Tašárová et al., 2006; Götze et al., 2007). A wavelength filtering technique was used to separate the regional-residual gravity anomalies north of the Dead Sea basin. The residual field revealed a complex pattern of anomalies, variously shaped and extended, showing a correlation with geological structures associated with the Dead Sea origin (El-Kelani, 2007). To remove the distortion caused by the low latitude, the total magnetic intensity map of the entire transform region was processed using a reduction-to-pole (RTP) technique (Rybakov et al., 2011; Segev and Rybakov, 2011; Schattner et al., 2019), which made the map represent the geology of the study region more directly.

In regional rifting areas, the qualitative analysis of gravity and magnetic anomalies provide the initial information about basin type, geometry, crustal structure, basement depth, and mostly the regional anomalies which correlate with the major geologic features at the surface. This study adopted the most newly-compiled gravity and magnetic anomaly maps (Figs. 4 and 5), and reviewed the regional scale qualitative interpretation of the potential fields in the transform region based mainly upon previous publications.

4.1 Description of the gravity anomaly fields

The detailed Bouguer anomaly map (Figure 4) shows values ranging from +70 mGal at the Mediterranean coastline to less than -130 mGal at the southern end of the Dead Sea. It is characterized by the presence of different anomalies that differ in their amplitudes, sizes, shapes, and trends. These anomalies are caused by a combination of various sources that are located at different depths. Major gravity features, having a regional extent, are most probably associated with the crustal type. Increasing Bouguer values can be observed on the map, towards the Mediterranean, attributed to crustal thinning beneath the coastal plain (Ginzburg and Makris, 1979) that is associated with a change from continental to oceanic crust, and caused by lateral lithological variations within the upper crust material beneath the northwestern part of the transform fault (Folkman and Bein, 1978; El-Kelani, 2007). The gravity low observed from the south to the north reflects the deepening of Precambrian basement beneath a thick accumulation of low density sedimentary rocks of Tertiary age (Folkman, 1981). Within the rift zone, a series of Bouguer minima along the transform fault, with the lowest values at the southern end of the Dead Sea, represents major depressions that correspond to pull-apart basins filled with sediments (Figure 1a), that include the Gulf of Aqaba in the south, the Dead Sea, Lake Tiberias (also called Sea of Galillee or Kinneret), and the Hula basin in a successive order (Ginzburg and Makris, 1979; Folkman, 1981; Kashai and Crocker, 1987; ten Brink et al., 1993; Rybakov et al., 2003; ten Brink et al., 2007). Negative Bouguer gravity on the southeastern plateau reaches a minimum value of -80 mGal which coincides with El-Jafr depression. There is a relatively large-scale local positive Bouguer anomaly over the eastern Dead Sea high lands, with a maximum value of -20 mGal along an axial of NW-SE trend, where its general trend follows an inferred zone of intrusion along the Karak-Wadi El-Fayha fault system (El-Kelani, 2006; Götze et al., 2007).

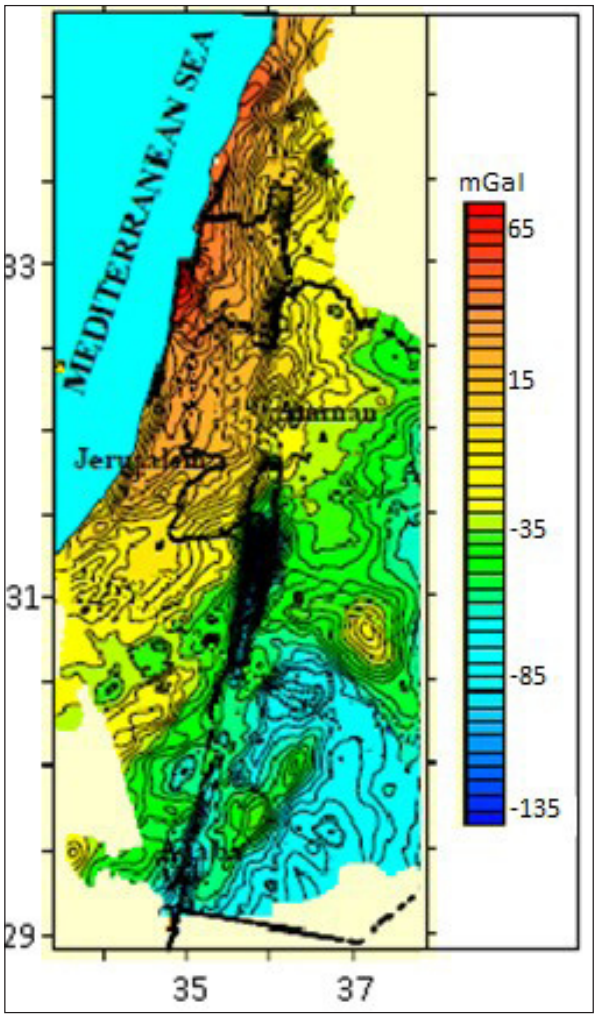

Figure 4. Bouguer anomaly map of the Jordan Dead Sea transform region, contoured at 5 mGal intervals (modified after Hassouneh, 2003).

The two opposite-facing plateaus are marked by a steep gravity gradient along the eastern and the western escarpments of the Dead Sea basin, with the lowest values at the southern end. This indicates a considerable increase of sedimentary thickness beneath the basin (Ginzburg and Makris, 1979; Folkman, 1981; ten Brink et al., 1993; Batayneh et al., 1995; Hassouneh, 2003; El-Kelani, 2006). The gradual decreasing of the Bouguer anomaly along the axis of the basin from both the northern and southern ends suggests that the basin sags toward the center, and is not bounded by

faults at its narrow ends (ten Brink et al., 1993). The positive gravity value, observed in the northern Dead Sea basin and referred to as the Ajlun dome anticline structure, could have resulted from the high density of Precambrian carbonates (Hassouneh, 2003). However, prior interpretations attributed this positive anomaly to changes of the depth of the Moho discontinuity with a relatively small elevation (Hofstetter et al., 2000).

4.2 Description of the magnetic anomaly fields

As shown in Figure 5, the magnetic anomalies in the DST region are characterized by diverse amplitudes, shapes, and wavelengths. Their values ranging from -500 to 500 nT, superimposed on the geological map, show the relationship between the deep basement features, which cause magnetic anomalies, and the shallow structures shown on the geological map.

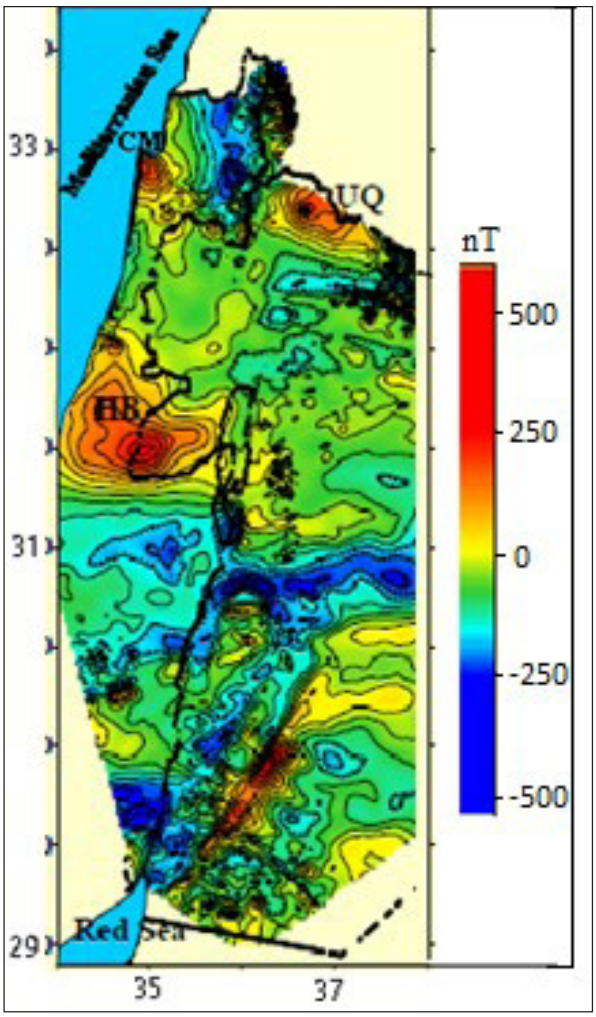

Figure 5. Aeromagnetic anomaly map of the Jordan Dead Sea Transform region, contoured at 50 nT intervals (modified after Hassouneh, 2003).

The total field aeromagnetic anomaly map is dominated by high frequency signals associated with the basalt flows north, northeast, east, and southeast of the Dead Sea basin that produce a strongly contrasting pattern of short wavelength, high frequency anomalies of low amplitude related to highly magnetic mafic rocks. The high-frequency signals are associated with surficial sources; whereas, the long-wavelength, lower-frequency signal anomalies reflect the deep basement features. In the south, a comparison of the geological and magnetic maps (Figures. 2 and 5) shows that the magnetic anomalies are directly correlative with the outcropping Precambrian crystalline rocks. Comparing the Hebron magnetic anomaly (HB) in the western plateau, with Um Qeis anomaly (UQ) in the eastern plateau (Figure 5), which are of a similar structure (Rybakov et al., 1999b; Khesin et al., 2005), correspond to the 105-107 km left-lateral movement along the DST fault (Hassouneh, 2003). This result is in agreement with the earlier magnetic investigations (Hatcher et al., 1981) which attributed the poor correlation in the magnetic anomalies facing each other across the DST fault, despite the short distance separating the two data sets, to something quite drastic geologically which has occurred in the intervening region.

On the other hand, the Hebron anomaly was suggested to be associated with a change in the composition and depth of the deep-seated basement rock (Domzalski, 1967, 1986; Folkman, 1976), or by a magmatic body related to Early Mesozoic intrusion that appears to penetrate the Triassic sedimentary strata at a depth of few kilometres (Rybakov et al., 1995a, 2011). Furthermore, the large contrast between the Hebron anomaly with the long wavelength and high amplitude and the anomaly of the very low amplitude immediately to the south, both being of a roughly east-west strike, was explained to indicate that a pre-Late Jurassic crustal boundary is present here; it was believed that this boundary could represent one between Tethyan and Arabian-African crust (Folkman and Bein, 1978).

The Carmel (CM) positive magnetic anomaly (Figure 5), corresponding to the Mount Carmel structure, was initially thought to be caused by a highly elevated crystalline basement (Ben-Avraham and Hall, 1977), or by the existence of a buried shield of Jurassic volcanoes beneath Mount Carmel (Gvirtzman et al., 1990). However, more recent studies suggested that it is high only in relation to the deep basin filled with considerable thickness of sediments in the surrounding areas, where the average densities of the Jurassic and Cretaceous volcanics, in the Mount Carmel region, are generally lower than those of the background sedimentary rocks (Rybakov et al., 2000; Segev and Rybakov, 2011), and the anomaly does not correspond to high-density magmatic rocks or the crystalline basement uplift (Rybakov et al., 2011).

5. Integrated interpretation of the gravity and magnetic anomalies

In addition to the comprehensive qualitative interpretations of the gravity and magnetic anomalies in the DST region, integrated quantitative interpretations of the two potential fields provided information about the density and magnetization models in the study area which allowed for a better delineation of the geologic structures and gave more reliable and accurate estimation of the depth, size, and composition of causative bodies. Previous quantitative interpretations of the gravity and magnetic data in the study area can be divided into two groups: large-scale, and small-scale interpretation.

5.1 Data interpretation at large-scale

The large-scale quantitative interpretation in the DST region is comprised of the studies that modelled the gravity

and magnetic anomalies as being caused by structures of lithospheric and crustal scale (Ben-Avraham and Hall, 1977; Folkman and Bein, 1978; Ginzburg and Makris, 1979; Folkman, 1981; Ginzburg and Ben-Avraham, 1986; Frieslander and Ben-Avraham, 1989; ten Brink et al., 1990, 1993; Ben-Avraham et al., 1996; Hofstetter et al., 2000; Rybakov et al., 2000; Batayneh and Al-Zoubi, 2001; Al-Zoubi and Ben-Avraham, 2002; Hassouneh, 2003; Rybakov and Segev, 2004; El-Kelani, 2006; Ben-Avraham and Schubert, 2006; Götze et al., 2007; Segev and Rybakov, 2011).

The first stages of gravity and magnetic 2-D modelling introduced initial results on the lithospheric structure beneath the western side of the DST and the central part of the Dead Sea rift (Folkman and Bien, 1978; Ginzburg and Makris, 1979; Folkman, 1981). The computed models were constrained by preliminary seismic information and the available borehole data.

The modelling results showed considerable thinning of the crust in the west along the Dead Sea- Mediterranean cross section, accompanied by lateral variations in the lithology of the upper crust, where mafic composition of the rock type increases from east to west (Folkman and Bien, 1978; Folkman, 1981). The E-W lateral lithological changes in the crustal rocks, associated with significant variations in stratigraphic thickness, have been interpreted to be caused by a transition between the Arabia-African continent and the Tethyan crust (Folkman and Bien, 1978).

On the other hand, the central portions of the transform zone were interpreted to be filled by young low-density sediments reaching about 7.5 km in depth beneath the Dead Sea basin (Folkman, 1981). Density distribution and magnetic susceptibility were also computed in the crust and upper mantle from the Gulf of Aqaba in the south towards the Mediterranean Sea in the north (Ginzburg and Makris, 1979; Folkman, 1981). The results indicated a slight thickening of the crystalized crust towards the north with an increase in the thickness of the low-density sediments. Whereas, the southern portion of the transform fault was modelled to be underlain by a low-density wedge in the upper mantle (Ginzburg and Makris, 1979; Folkman, 1981). The low-density wedge was explained to be connected with the presence of high temperature, low density upper mantle that is related to the invasion of upper mantle material into the crust beneath the southern part of the transform fault (Ginzburg and Makris, 1979), which may form an extension of the geodynamically active Read Sea rift system.

Later crustal and upper mantle models of the northern Jordan DST fault, using potential field data, were computed for both sides of the Dead Sea rift (ten Brink et al., 1990; Hofstetter et al., 2000). The transition in crustal structure across the transform fault was modelled based on gravity data with a combination of teleseismic P-wave inversion and refraction seismic investigations. The geometry of the transition showed more gradual transition in Moho depth with an abrupt transition across the transform fault where a 4-5 km offset in the depth to Moho was required to be modelled (ten Brink et al., 1990). The thickness of the crust under the western side of DST fault reaches about 24 km at the Mediterranean shore; whereas, the crust on the eastern side of the transform is about 30 km thick, and is fairly constant in thickness (ten Brink et al., 1990) with an abrupt change in crustal thickness across the Dead Sea rift (ten Brink et al., 1990; Hofstetter et al., 2000). This abrupt change was explained to be caused by the 107 km left-lateral movement along the DST fault (ten Brink et al., 1990). A comparison between the two crustal and upper mantle models under the DST fault computed by ten Brink et al. (1990) and Hofstetter et al. (2000) is shown in Figure 6.

In addition, the depth to the top of the crystalline basement has been mapped and modelled for the medium valley of the Dead Sea rift and the surrounded shoulders using magnetic and gravity data (El-Isa and Kharabsheh, 1983; Rybakov and Segev, 2004; Al-Zoubi and Ben-Avraham, 2002; Segev et al., 2006). The results of the potential field data interpretation after reviewing the available information on the study area (deep boreholes and seismic profiles) showed that the depth to the basement is variable; within the rift it is always greater than 5 km, and generally increases toward the Dead Sea and Tiberias basins at about 8-10 km depth (El-Isa and Kharabsheh, 1983; ten Brink et al., 1990; Hofstetter et al., 2000; Al-Zoubi and Ben-Avraham, 2002; El-Kelani, 2006; Götze et al., 2007). The basement in the eastern and western flanks of the rift deepens gradually northward from 3 to 7 km, while the top of the crystalline basement becomes shallow to about 1 km southward, where the Precambrian complex rocks can be seen on the surface (Al-Zoubi and Ben-Avraham, 2002; Rybakov and Segev, 2004; Segev et al., 2006).

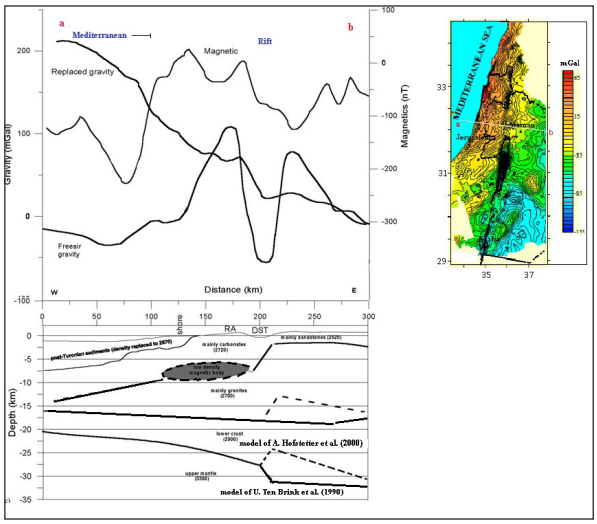

Figure 6. 2-D crustal model of the northern Jordan DST fault. Solid lines indicate the earlier gravity model of ten Brink et al. (1990), while dashed lines represent the modification made by Hofstetter et al., (2000) based on best gravity and magnetic data and teleseismic velocity anomalies.

Moreover, the string of young sedimentary basins, separating the two sides of the rift (Ginzburg and Makris, 1979, Folkman, 1981; Kashai and Crocker, 1987; ten Brink et al., 1993; Rybakov et al., 2003; ten Brink et al., 2007), has a basement step that reaches about 5 km which represents a displacement for the largest vertical faults along the DST fault zone (Hofstetter et al., 2000; Tašárová et al., 2006).

On the other hand, gravity and magnetic 2-D modelling was conducted to reveal the geometry of the large

sedimentary basins within the DST fault zone, and to compute the thickness of the basin fills, and identify their types (Frieslander and Ben-Avraham, 1989; Ben-Avraham et al., 1996; ten Brink et al., 1993; Batayneh et al., 1995; Rybakov et al., 2003; Ben-Avraham and Schubert, 2006). The analysis and modelling of gravity data for the Dead Sea basin, being the largest one, showed that the basin has two main depth levels. The northern one has a sedimentary fill of about 6 km; whereas, the southern Dead Sea basin is unusually deep, and the thickness of sediments is about 14 km (ten Brink et al., 1993; Batayneh et al., 1995; Ben-Avraham and Schubert, 2006). The density distribution of the basin sediments was also assigned by depth in the range of 2150-2620 kg/m^3, which represent light sediments (mainly evaporates), of Quaternary deposits, at the top, to Mesozoic-Palaeozoic sediments, of carbonate and sandstone rocks at the bottom. The analysis and modelling of gravity data revealed that the geometry of the Dead Sea basin is 132 km long, 17-18 km wide, and the basin becomes narrower and shallower towards the northern and southern ends. The 2-D gravity model of the second largest basin, Tiberias Lake in the northern Jordan DST fault zone, divided the basin into two distinct units (Ben-Avraham et al., 1996). The southern half represents the deepest half of about 14 km in depth; northwards, the basin becomes wider (the width varies between 8-18 km) and the thickness reaches 12 km. The assigned densities lie within the range of the Dead Sea sediments that is between 2150-2250 kg/m^3. In addition, a magnetic study model was performed across the Dead Sea basin in the E-W direction (Frieslander and Ben-Avraham, 1989), where the model showed that the basement rocks under the Dead Sea have the same magnetic characteristics similar to the rocks under the land area to the west. The model study also gave the best fits when the basement rocks east of the basin are modelled as much more elevated than the basement west of the basin with lower magnetic susceptibility. The gravity and magnetic study models of the two main basins (Dead Sea, Tiberias) agreed with a pull-apart structure, as accepted mechanism, but with no existence of diagonal faults at the northern and southern ends of the basin (Frieslander and Ben-Avraham, 1989; ten Brink et al., 1993). However, some earlier results, based on magnetic data, proposed the formation of a rhomb-shaped graben for the Tiberias basin (Ben-Avraham et al., 1980). Moreover, alternative gravity models suggested a "drop down' basin instead of a pull-apart for the deep part of the southern Dead Sea basin (Ben-Avraham and Schubert, 2006).

Afterwards, a 3-D interpretation of the newly-combined Bouguer anomaly map of the southern Jordan DST fault zone and of the Dead Sea basin (Figure 7) was conducted (Hassouneh, 2003; El-Kelani, 2006; Götze et al., 2007). A regional scale, a high resolution 3-D layered structure-density model was computed. The model was constrained with the more recent seismic results (DESERT, 2004 and references therein) using all of the available geological information and rock density log deep borehole data (Rybakov et al., 1999a). It revealed a possible crustal thickness and density distribution beneath the Jordan DST fault zone (Figure 7).

The model showed that the zone of the maximum crustal thinning (≤30 km) is attained in the western sector at the Mediterranean. The south-eastern plateau shows, by far, the largest crustal thickness in the transform region (38-42 km). The computed results of the thickness and densities of the crust, ranging between 2650-2900 kg/m^3, suggested that the DST fault is underlain by continental crust. On the other hand, the modelled deep basins (≥10 km), the relatively large nature of an intrusion, and the asymmetric topography of the Moho, led to the suggestion that a small-scale asthenospheric upwelling might be responsible for the thinning of the crust and subsequent rifting of the DST fault during the left-lateral strike-slip motion at the boundary between African and Arabia Plates (El-Kelani, 2006; Götze et al., 2007).

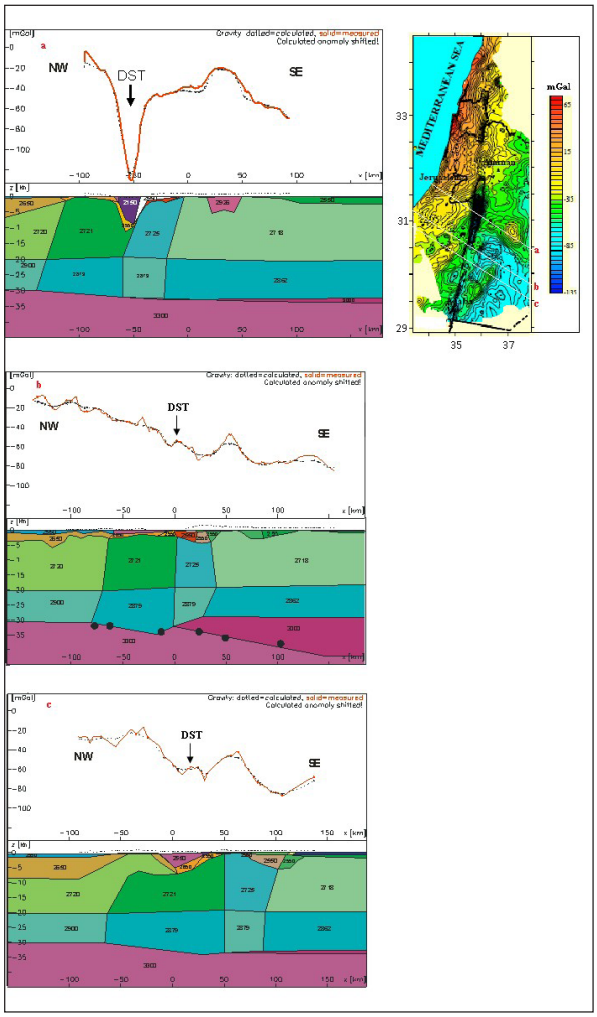

Figure 7. 3-D crustal model of the central and southern Jordan DST fault zone (modified after El-Kelani, 2006; Götze et al., 2007).

5.2 Small-scale data interpretation

Gravity and magnetic data interpretation was also carried out with regard to the investigations that are focused on smaller DST districts. Some detailed investigations studied intrusive bodies within the uppermost crustal layers to a depth of about 5 km (Ben-Avraham and Hall, 1977; Ginzburg and Ben-Avraham, 1986; Segev et al., 1999; ten Brink et al., 1999; Rybakov et al., 2000; Khesin et al., 2005; Eppelbaum et al., 2004, 2007), while other investigations focused on structures and the distribution of salt diapirs in the Dead Sea basin (Neev and Hall, 1979; Al-Zoubi and ten Brink, 2001; Choi et al., 2011). Moreover, meter-scale, high-

precision gravimetric and magnetic surveys were utilized to detect caverns and sinkholes along the coast of the Dead Sea (El-Isa et al., 1995; Rybakov et al., 2001, 2005; Closson et al., 2005; Eppelbaum et al., 2008; Ezersky et al., 2010, 2013; Shirman and Rybakov, 2009).

Model studies of the gravity and magnetic anomalies, corresponding to the Mount Carmel structure, suggested that they are caused by basic intrusive igneous bodies, ≥4km, associated with elevated crystalline basement (Ben-Avraham and Hall, 1977). While, thereafter, the idea of being related to magmatic roots of volcanics at shallow depths between 3-5 km was adopted (Rybakov et al., 2000), suggesting that average densities of the volcanics are lower than those of the background sedimentary rocks.

Also, the results of the magnetic interpretation showed that a model incorporates a gabbroic intrusion at 2-4 km within the light sediments of Tiberias basin overlaid by a basaltic layer (Ginzburg and Ben-Avraham, 1986; Eppelbaum et al., 2004, 2007).

On the other hand, magnetic characteristics were studied for a complex of metamorphosed carbonate rocks in the Hatrurium Basin, west of the Dead Sea, which is situated at the Hebron aeromagnetic anomaly (Figure 5). Magnetic measurements were used to study the Hatrurium formation, where shallow small bodies of variable magnetic susceptibility were found with marked heterogeneity and anisotropy reflecting the high-grade of metamorphism (Khesin et al., 2005). Furthermore, magnetic and gravity data were applied to investigate the Precambrian basement north of Aqaba (Segev et al., 1999). The interpretation of the potential data enabled the characterizing of the tectono-magmatic setting of the crystalline basement, where the results showed common intrusive relationships between dissimilar intrusive bodies, while the dense basic and intermediate magmatic bodies have different magnetic properties.

Among the upper crustal-scale interpretation as well, 2-D and 3-D density models, using gravity data, were constructed to present information on the underground structures associated with the generation of salt domes and diapirs in the Dead Sea basin (Al-Zoubi and ten Brink, 2001; Choi et al., 2011). 2-D gravity models constrained seismic reflection data, and a magnetic map was computed to delineate the extent and depth of two salt diapirs under Lisan Peninsula and Sedom area (Al-Zoubi and ten Brink, 2001). The Lisan diapir reaches a maximum depth of about 7 km, and extends further to the south, whereas the Sedom diapir south of the Lisan is no deeper than 5.5-6 km (Figure 8a). Moreover, 3-D density modelling led to the identification of three salt structures found beneath the Sedom area, the Lisan Peninsula, and the northern basin of the Dead Sea (Choi et al., 2011). The 3-D density models were based on a new compilation of Bouguer gravity data stemming from airborne, shipborne, and terrestrial data, and the most recent seismic investigation (Weber et al., 2009). 3-D gravity modelling enabled a detailed resolution of the upper crustal structures from the southern to the northern subbasin below the saline Dead Sea. The results suggest that a salt diaper exists at a top of about 2 km in the northern Dead Sea subbasin with a thickness of about 4 km, which has not been recognized by any other prior geophysical interpretations. However, earlier combined analysis of magnetic and seismic investigations (Neev and Hall, 1979) detected a salt diapir beneath the same location and with a similar geometry.

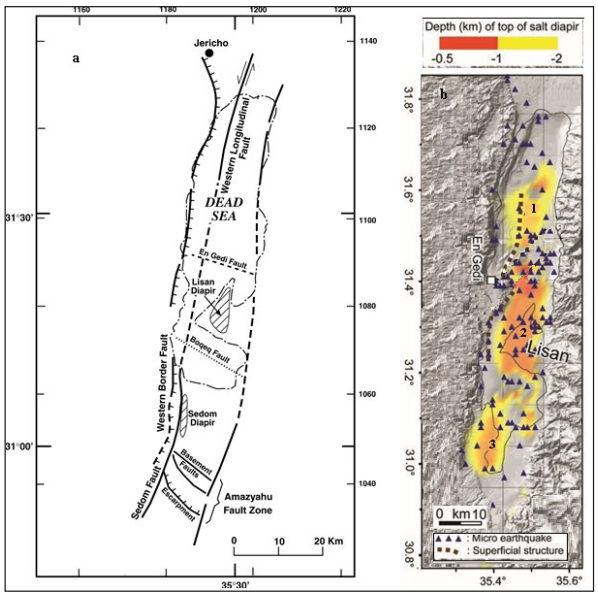

Figure 8. Location maps of the spatial distribution of the inferred salt diapirs modelled by Al-Zoubi and ten Brink (2001) in the Dead Sea basin (left) compared with the modelled salt diapirism (right) by Choi et al., (2011).

The dimensions of the salt diapirs computed by the 3-D models (Figure 8b) are about 10 km by 20 km, with an average thickness of approximately 6 km for the Lisan Peninsula and about 5 km by 10 km, with an average thickness of approximately 4 km for the Sedom salt diapir which are larger than the same ones (Lisan and Sedom) computed by the 2-D modelling. The differences were attributed to the fact that more gravity and constraining data enhanced the 3-D modelling (Choi et al., 2011). Furthermore, the 2-D gravity models assume that the diapiric rise is related to the transtension and subsidence tectonic activity during the formation of the Dead Sea pull-apart basin (Al-Zoubi and ten Brink, 2001) while the 3-D gravity model, referred the shallower micro earthquake activity in the Dead Sea basin to the movement of the salt diapirs (Choi et al., 2011).

Attempts were made, on the other hand, to understand the occurrence and development of sinkholes and other karst features in the Dead Sea coastal area using several geophysical techniques (Ezersky et al., 2017, and references therein). Among these, potential data measurements have been tested and employed to investigate and predict the occurrences of some sinkholes by carrying out, specifically, microgravity and micromagnetic surveys. Microgravity field analysis was implemented on sinkhole hazards along both the western Dead Sea shore (Rybakov et al., 2001; Ezersky et al., 2010, 2013; Eppelbaum et al., 2008), and the eastern coastline (Abou Karaki, 1995; Al-Zoubi et al., 2013), in order to detect caves and determine the sinkhole formation mechanism. This monitoring geophysical technique was chosen to investigate sinkholes based on the existence of sufficient density contrasts regardless of shape or fill material. Residual gravity maps and 3-D microgravity

modelling were applied to resolve the sinkhole problem in an attempt to estimate qualitative and quantitative parameters of buried cavities. The microgravity method was tested at different locations along the Dead Sea shorelines to detect buried karst and salt dissolution caverns, and compute their underground spatial distribution (Figure 9). It was tested in the areas of Ein Gedi-Hever (Rybakov et al., 2001), Nahal Hever South (Eppelbaum et al., 2008; Ezersky et al., 2010), Ein Gedi-Arugot (Ezersky et al., 2013), and Ghor Al-Haditha-Lisan Peninsula (Abou Karaki, 1995; Closson et al., 2005; Al-Zoubi et al., 2013). As a feasibility study, the micromagnetic technique was used as well to investigate sinkhole development and to detect caves along the western Dead Sea coast (Rybakov et al., 2005; Shirman and Rybakov, 2009).

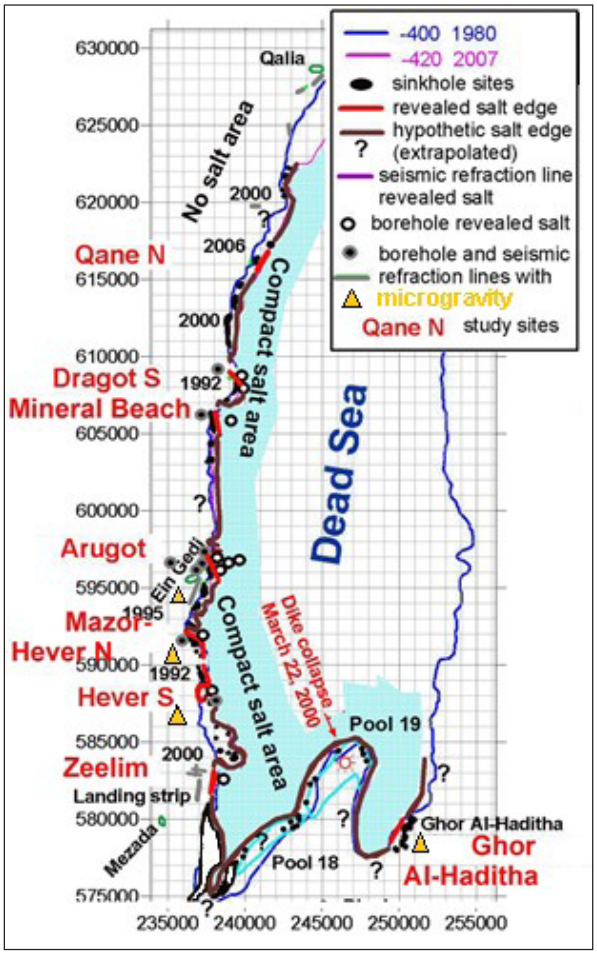

Figure 9. Sinkhole sites studied by means of the microgravity technique (modified after Ezersky et al., 2017).

The micromagnetic study was carried out to test the possibility of delineating weak magnetic anomalies related to shallow voids or caves. The feasibility studies surpassed the expectations, and enabled the delineation of buried fault zones controlling the sinkhole process (Rybakov et al., 2005) and the detection of voids that are reliable precursors of sinkhole development and ground collapse (Rybakov et al., 2005; Shirman and Rybakov, 2009).

6. Conclusions

Gravity and magnetics play a leading role among the reconnaissance geophysical methods. Advances in the collection and the extensive coverage of gravity and magnetic data that exist over the DST region enabled a detailed analysis of the two potential fields on the regional and local scales.

The analysis and interpretation of the gravity and magnetic field data provided a geological picture of the subsurface which allowed for a better understanding of the tectonic evolution in the Jordan DST zone. Major tectonic features such as volcanics, magmatic intrusive bodies, and basin-scale fault trends corresponded with the regional patterns and the abnormal shapes of the gravity and magnetic anomalies over the transform fault zone. Applying a variety of filtering techniques enhanced the qualitative interpretations of the various frequency components of the potential fields; removing the giant regional effect enabled the recognition of shallow depth-causative geological structures. The residual anomalies, on the other hand, showed a correlation with tectonic lineaments, shallow structures and small-scale volcanic intrusions within the uppermost part of the crust inferred from high amplitude of the related anomalies.

The earliest results of the 2-D quantitative interpretation of the combined gravity and magnetic field provided a significant contribution to the investigation of the deep lithospheric structures and led to the identification of Moho offset across the Jordan DST fault zone. Any geophysical interpretation is subject to a fundamental ambiguity involving the effect of a physical property and a volume. In as much as the results obtained from the potential field data were inherently not unique presented by several possible models, their reliability and accuracy were estimated by a comparison with seismic observations and the available drill-hole data. The advanced 3-D density modelling that incorporated results from additional recent geophysical investigations enabled a detailed resolution of the upper crustal structure. Deep basins, vertical offset of basement, relatively large intrusions, and a small asymmetric topography of the Moho were interpreted beneath the Jordan DST fault zone by 3-D density models.

At a shorter scale, the gravity and magnetic data in the DST region were useful for geological interpretations in specific areas. By means of new techniques, microgravity and micromagnetic models proved to be good tools for detecting buried sinkholes and karst cavities along the Dead Sea coast.

The findings of the qualitative and quantitative interpretation of the gravity and magnetic anomaly fields confirmed the contrasting nature of the structures in the eastern and western plateaus of the Jordan DST fault zone. The results correlated with the known geology at the surface, and showed good agreement with the main tectonic elements and geologic structures in the DST region such as the sediment basins, salt diapirs, volcanic activity, magmatic intrusions, thinning of the crust, and the lateral and vertical offset of the basement. The data analysis of the gravity and magnetics at the regional and local scale has been linked to the left-lateral strike-slip movement at the boundary between the Arabian-African plates and to the transition zone marking a major crustal lithological discontinuity from the eastern segment of the northern edge of the continental plate into

the oceanic zone at the Mediterranean coastline of a remnant Tethyan crust. Besides, the potential data were utilized, in the transform region, for the qualitative interpretation of regional geology and structural features in sedimentary basins, as one of the first steps in the search for petroleum.

The quantitative integration of varying gravity and magnetic datasets is one of the main challenges of potential field interpretations. These data sets differ in the type of data acquisition, equipments used, and geographical scale, elevation of measurement stations and their spacing, physical limitations in the field, borders, and different datum. These challenges can be tackled through improving the coverage of gravity and the magnetic measurement extent by conducting ground surveys in the DST region and applying the equivalent source technique for the integration of all available data sources, upon their high variability. Conducting new gravity and magnetic surveys in the DST region is also recommended for more local measurements to shed more light on small-scale structures, and to clarify their geological meaning in an attempt to increase the details of information that would represent a decisive step towards minimizing the remaining contentious issues.

Acknowledgment

This work has been accomplished during a sabbatical the author spent at the Department of Geology of Utah State University, Logan with financial support from An-Najah National University, Palestine. Professor Tony Lowry is very much thanked for inviting me and supplying me with the required facilities to complete this work. The author would like to thank Professor Joel Pederson, the department head, for facilitating logistical and administrative issues during his scientific visit.

References

Abou Karaki, N. (1995). The precise gravity survey. In: Center for consultation, Technical services and studies assessment of the hazard of subsidence and sinkholes in Ghor Al Haditha area. University of Jordan, final report Feb, 1995, Amman, P. 117–133.

Achmon, M., and Ben-Avraham, Z. (1997). The deep structure of the Carmel fault zone, northern Israel, from gravity field analysis. Tectonics 16: 563–569.

Al-Zoubi, A. (2007). The basement faults systems in the northwestern Arabian Plate, Jordan. Bulletin of the Geological Society of Greece vol. XXXX, 2007 Proceedings of the 11th International Congress, Athens 251-263.

Al-Zoubi, A., and Ben-Avraham, Z. (2002). Structure of the earth's crust in Jordan from potential field data. Tectonophysics 346: 45-59.

Al-Zoubi, A., and ten Brink, U. (2001). Salt diapirs in the Dead Sea basin and their relationship to Quaternary extensional tectonics. Marine and Petroleum Geology 18: 779-797.

Al-Zoubi, A., ten Brink, U., Rybakov, M., Rotstein Y. (2004). Using high-resolution aeromagnetic survey to map tectonic elements of plate boundaries: An example from the Dead Sea Transform. Abstract. Eos American Geophysical Union Transactions, Fall Meeting Supplement 85 (47), Abstract G44A-07.

Al-Zoubi, A., Eppelbaum, L., Abueladas, A., Ezersky, M., Akkawi, E. (2013). Removing regional trends in microgravity in complex environments: Testing on 3D model and field investigations in the eastern Dead Sea coast (Jordan). International Journal of Geophysics 2013, 341797, 13 p. https://doi.org/10.1155/2013/341797.

Aydin, A., and Nur, A. (1982). Evolution of pull-apart basins and their scale independence. Tectonics 1: 91-105.

Batayneh, A., and Al-Zoubi, A. (2001). The gravity field and crustal structure of the northwestern Arabian Platform in Jordan. Journal of African Earth Science 32: 141-148.

Batayneh, A., Al-Zoubi, A., Hassouneh, M. (1995). Magnetic and gravity investigation of the Lisan Peninsula- Dead Sea (Jordan). China University Geosciences Journal 6: 213-218.

Ben-Avraham, Z., and Hall, J. (1977). Geophysical survey of Mount Carmel structure and its extension into the eastern Mediterranean. Journal of Geophysical Research 82: 793-802.

Ben-Avraham, Z., and Katsman, R. (2015). The formation of graben morphology in the Dead Sea Fault, and its implications. Geophys. Res. Lett. 42: 6989–6996.

Ben-Avraham, Z. and Schubert, G. (2006). Deep "drop down" basin in the southern Dead Sea. Earth and Planetary Science Letters 251: 254-263.

Ben-Avraham, Z., and ten Brink, U. (1989). Transverse faults and segmentation of basins within the Dead Sea. Journal of African Earth Sciences 8: 603-616.

Ben-Avraham, Z., Garfunkel, Z., Lazar, M. (2008). Geology and evolution of the southern Dead Sea fault with emphasis on subsurface structure. Annu. Rev. Earth Planet. Sci. 36: 357–387.

Ben-Avraham, Z., ten Brink, U., Bell, R., Reznikov, M. (1996). Gravity field over the Sea of Galilee: Evidence for a composite basin along a transform fault. Journal of Geophysical Research: Solid Earth 101: 533-544.

Ben-Avraham, Z., Shoham, Y., Klein, E., Michelson, H., Serruya, C. (1980). Magnetic survey of Lake Kinneret-central Jordan Valley, Israel. Marine Geophysical Researches 4: 257-276.

Beydoun, Z. (1999). Evolution and development of the Levant (Dead Sea Rift) Transform System: A historical-chronological review of a structural controversy. Geological Society, London, Special Publications 164: 239-255.

Choi, S., Götze, H. J., Meyer, U., DESIRE Group. (2011). 3-D density modelling of underground structures and spatial distribution of salt diapirism in the Dead Sea Basin, Geophys. J. Int. 184: 1131–1146.

Closson, D., Abou Karaki, N., Klinger, Y., Hussein, M. (2005). Subsidence hazards assessment in the Southern Dead Sea area, Jordan. Pure Appl. Geophys. 162: 221–248.

DESERT Group (2004). The crustal structure of the Dead Sea Transform. Geophys. J. Int. 156: 655-681.

Domzalski, W. (1967). Aeromagnetic Survey of Israel: Interpretation. IPRG Report SMA/482/67.

Domzalski, W., (1986). Review and additional interpretation of selected magnetic data in Israel and adjoining areas. Oil Exploration (Investments) Ltd.

Dvorkin, A., and Kohn, B. (1989). The Asher volcanics, northern Israel. Isr. J. Earth Sci. 38: 105-123.

El-Kelani, R. (2006). Three-dimensional gravity model of the southern Jordan Dead Sea Transform, An-Najah Univ. J. Res., Ser. A 19: 185-207.

El-Kelani, R. (2007). Interpretation of gravity data in the Jericho area, Dead Sea Transform. The Islamic University Journal (Natural Studies and Engineering) 15: 21-39.

El-Kelani, R., El-Isa, Z., Zaid, A. (1998). Interpretation of gravity data in Zarqa Ma'in hot springs area, preliminary evaluation of the geothermal resources of Jordan. 58 Conference of the German Geophysical Association, Goettingen, GG43, 81.

El-Isa, Z. H. (2017). The instrumental seismicity of the Jordan Dead Sea transform, Arab J. Geosci. 10: 203-213.

El-Isa, Z. H., and Kharabsheh, A. (1983). Magnetic and gravity studies of the northern Dead Sea Rift. In Abed and Khaled (Eds.), proceeding the 1st Jordan geological Conference, Amman, 483-501.

El-Isa, Z. H., Rimawi, O., Jarrar, G., Abou Karaki, N., Taqieddin, S., Atallah, M., Abderahman, N., Al-Saed, A. (1995). Assessment of the hazard of subsidence and sinkholes in Ghor Al-Haditha area. Report submitted to Jordan Valley Authority. University of Jordan, Amman: 141 p.

Eppelbaum, L., and Katz, Y. (2011). Tectonic-geophysical mapping of Israel and the Eastern Mediterranean: Implications for hydrocarbon prospecting, Positioning 2: 36-54.

Eppelbaum, L., Ben-Avraham, Z., Katz, Y. (2004). Integrated analysis of magnetic, paleomagnetic and K-Ar data in a tectonic complex region: An example from the Sea of Galilee. Geophys. Res. Lett. 31, L19602, doi:10.1029/2004GL021298.

Eppelbaum, L., Ben-Avraham, Z., Katz, Y. (2007). Structure of the Sea of Galilee and Kinarot Valley derived from combined geological geophysical analysis. First Break 25: 43-50.

Eppelbaum, L., Ezersky, M., Al-Zoubi, A., Goldshmidt, V., Legchenko, A. (2008). Study of the factors affecting the karst volume assessment in the Dead Sea sinkhole problem using microgravity field analysis and 3D modeling. Advances in Geosciences 19: 97-115.

Ezersky, M., Legchenko, A., Eppelbaum L. Al-Zoubi A. (2017). Overview of the geophysical studies in the Dead Sea coastal area related to evaporite karst and recent sinkhole development. International Journal of Speleology 46: 277-302.

Ezersky, M., Eppelbaum, L., Al-Zoubi, A., Keydar, S., Abueladas, A., Akkawi, E., Medvedev, B. (2013). Geophysical prediction and following development sinkholes in two Dead Sea areas, Israel and Jordan. Environ Earth Sci. 70: 1463-1478.

Ezersky, M., Legchenko, A., Camerlynck, Ch., Al-Zoubi, A., Eppelbaum, L., Keydar, Sh., Boucher, M., Chalikakis, K. (2010). The Dead Sea sinkhole hazard- new findings based on a multidisciplinary geophysical study, Zeitschrift für Geomorphologie, Supplementary 54: 69-90.

Folkman, J. (1970). Aeromagnetic Survey in the Areas of the Golan, Shomron, Judea and Gaza Offshore. IPRG Report SMA/760/70.

Folkman, Y. (1981). Structural features in the Dead Sea-Jordan rift zone, interpreted from a combined magnetic-gravity study. Tectonophysics 80: 135-146.

Folkman, Y., and Bein, A. (1978). Geophysical evidence for a pre-Late Jurassic fossil continental margin oriented east-west under central Israel. Earth and Planetary Science Letters 39: 335-340.

Folkman, Y., and Ginzburg, A. (1981). Geophysical investigation of crystalline basement between Dead Sea Rift and Mediterranean Sea. AAPG Bulletin 65: 490-500.

Folkman, Y., and Yuval, Z. (1976). Aeromagnetic Map of Israel, Scale 1:250,000 (two sheets). Inst. Petrol. Res. Geophys.

Freund, R., Garfunkel, Z., Zak, I., Goldberg, M., Weissbrod, T., Derin, B. (1970). The shear along the Dead Sea rift. Philos. Trans. R. Soc. London, Ser. A 267: 107-130.

Frieslander, U., and Ben-Avraham, Z. (1989). Magnetic field over the Dead Sea and vicinity. Marine and Petroleum Geology 6: 148-160.

Garfunkel, Z. (1981). Internal structure of the Dead Sea leaky transform (rift) in relation to plate kinematics. Tectonophysics 80: 81–108.

Garfunkel, Z. (1988). The pre-Quaternary geology of Israel, in The Zoogeography of Israel. Y. Yom-Tov and E. Ternov (Ed) by, pp. 7–34, W. Junk, Dordrecht, Netherlands.

Garfunkel, Z. (1989). The tectonic setting of Phanerozoic magmatism in Israel. Isr. J. Earth Sci. 38: 51-74.

Garfunkel, Z., and Ben-Avraham, Z. (2001). Basins along the Dead Sea Transform. In Peri-Tethyan Rift/Wrench Basins and Passive Margins, ed. PA Ziegler, WCavazza, AHF Roberts, S Crasquin-Soleau. Memo. Mus. Natl. His. Nat. 186: 607-27.

Garfunkel, Z., and Freund, R. (1981). Active faulting in the Dead Sea rift. Tectonophysics 80: 1-26.

Ginzburg, A., and Ben-Avraham, Z. (1986). The structure of the Sea of Galilee graben from magnetic measurements. Tectonophysics 126: 153–64.

Ginzburg, A., and Makris, J. (1979). Gravity and density distribution in the Dead Sea rift and adjoining areas. Tectonophysics 54, 17-25.

Girdler, W. (1990). The Dead Sea transform fault system, Tectonophysics 180: 1-13.

Götze, H-J. El-Kelani, R., Schmidt, S., Rybakov, M., Hassouneh, M., Förster, H., Ebbing, J. (2007). Integrated 3D density modelling and segmentation of the Dead Sea Transform. International Journal of Earth Sciences 96: 289-302.

Götze, H-J., Meyer, U., Choi, S., Bartov, Y., Ben-Avraham, Z., Jasser, D., Abu Ayyash, Kh., El-Kelani, R. (2010b). Helicopter-borne gravity survey in the Dead Sea area. Eos Trans AGU Electronic supplement 91(12):109. doi: 10.1029/2010EO120002.

Götze, H-J. Ebbing, J., Hese, F., Kollersberger, T., Schmidt, S., Rybakov, M., Hassouneh, M., Hrasha, M., El-Kelani, R. (2002). Gravity field analysis and 3D density modeling of the lithosphere along the Dead Sea Transform. Eos Trans. AGU, 83(47), Fall Meet. Suppl., Abstract S61A-1105.

Griffin, W., Gain, S., Huang, J-X., Belousova, E., Toledo, V., O'Reilly, S. Y. (2018). Permian to quaternary magmatism beneath the Mt Carmel area, Israel: zircons from volcanic rocks and associated alluvial deposits. Lithos 314-315: 307-322.

Gvirtzman, G., and Steinitz, G. (1983). The Asher volcanics- an early Jurassic event in northern Israel. GSI Curr. Res. 28-33.

Gvirtzman, Z., and Weinberger, R. (1994). Interpretation of Ramon basalt magnetic anomalies: magnetic modelling and paleomagnetic study. Isr. J. Earth Sci. 43: 47-56.

Gvirtzman, G., Klang, A., Rotstein, Y. (1990). Early Jurassic shield volcano below Mount Carmel: a new interpretation of the magnetic and gravity anomalies and implications for early Jurassic rifting. Isr. J. Earth Sci. 39: 149-159.

Hassouneh, M. (2003). Interpretation of potential fields by modern data processing and 3-dimensional gravity modelling of the Dead Sea pull-apart basin/Jordan Rift Valley (JRV), p. 110, Dissertation, Uni Würzburg.

Hatcher, R., Zietz, I., Regan, R., Abu-Ajamieh, M. (1981). Sinistral strike-slip motion on the Dead Sea Rift: Confirmation from new magnetic data. Geology 9: 458-462.

Hofstetter, A., Dorbath, C., Rybakov, M., Goldshmidt, V. (2000). Crustal and upper mantle structure across the Dead Sea rift and Israel from teleseismic P wave tomography and gravity data. Tectonophysics 327: 37-59.

Ibrahim, K., Moh'd, B., Masri, A., Al-Taj, M., Musleh, S., Alzughoul, K, (2014). Volcanotectonic evolution of central Jordan: Evidence from the Shihan Volcano, Journal of African Earth Sciences 100: 541-553.

Kashai, E., and Croker, P. (1987). Structural geometry and evolution of the Dead Sea- Jordan rift system as deduced from new subsurface data. Tectonophysics 141: 33–60.

Khesin, B., Feinstein, S., Vapnik, Ye., Itkis, S., Leonhardt, R. (2005). Magnetic study of metamorphosed sedimentary rocks of the Hatrurim formation, Israel. Geophys. J. Int. 162: 49-63.

Kovach, R., and Ben-Avraham, Z. (1985). Gravity anomalies across the Dead Sea rift and comparison with other rift zones. Tectonophysics 111: 155-162.

Mechie, J., Abu-Ayyash, Kh., Ben-Avraham, Z., El-Kelani, R., Qabbani, I., Weber, M. (2009). Crustal structure of the southern Dead Sea basin derived from project DESIRE wide-angle seismic data. Geophys. J. Int. 178: 457–478.

Mimran, Y. (1972). The Tayassir volcanics and Lower Cretaceous formation in the Shomron, central Israel. GSI Bull. 58: 1-52.

Neev, D., and Hall, J. (1979). Geophysical investigations in the Dead Sea. Sedimentary Geology 23: 209-238.

Phoenix Corp. (1980). Comprehensive airborne magnetic/ radiation survey of the Hashemite Kingdom of Jordan. Final Report to Natural Resources Authority. Phoenix Corporation. McLean, Virginia.

Quennell, A. (1958). The structural and geomorphic evolution of the Dead Sea Rift. Q. J. Geol. Soc. London 114: 1-24.

Quennell, A. (1959). Tectonics of the Dead Sea Rift. Proc. 20th Intern. Geol. Congress, Mexico, 1956, ASGA: 385-403.

Quennell, A. (1984). The Western Arabia rift system. In: Dixon, J.F. and Robertson, A.H.F. (eds) The Geological Evolution of the Eastern Mediterranean, Geol. Soc. Spec. Publ. 17: 775-88.

Rosenthal, M., Segev, A., Rybakov, M., Lyakhovsky, V., Ben-Avraham, Z. (2015). The deep structure and density distribution of northern Israel and its surroundings. Geological Survey of Israel, Report GSI/12/2015, pp. 38.

Rybakov, M., and Al-Zoubi, A. (2005). Bouguer gravity map of the Levant- a new compilation. In: Geological framework of the Levant (edited by Hall, J.K., Krasheninnikov, V.A., Hirsch, F., Benjamini, C. and Flexer, A.), Vol. II: The Levantine basin and Israel, Chap. 19: 539–542. Historical Productions-Hall, Jerusalem.

Rybakov, M., and Segev, A. (2004). The top of the crystalline basement in the Levant, Geochemistry Geophysics Geosystems 5, Q09001.doi:10.1029/2004GC000690.

Rybakov, M., Fleischer, L., Goldshmidt, V. (1995a). A new look at the Hebron magnetic anomaly. Isr. J. Earth Sci. 44: 41-49.

Rybakov, M., Goldshmidt, V., Fleischer, L. (1995b). Interpretation of gravity and magnetic data from Israel and adjacent areas: investigation results. Report No. 702/42/91, Institute for Petroleum Research and Geophysics, Holon.

Rybakov, M., Goldshmidt, V., Rotstein, Y. (1997). New regional gravity and magnetic maps of the Levant. Geophysical Research Letters 24: 33-36.

Rybakov, M., Fleischer, L., ten Brink, U. (2003). The Hula Valley subsurface structure inferred from gravity data. Isr. J. of Earth Sci. 52: 113-122.

Rybakov, M., Segev, A., Lyakhovsky, V. (2009). Gravity and magnetic study of the subsurface geology in Mount Carmel and the Yizre'el Valley, ES-34-2009, pp. 37.

Rybakov, M., Goldshmidt, V., Rotstein, Y., Fleischer, L., Goldberg, I. (1999a). Petrophysical constraints on gravity/ magnetic interpretation in Israel. The Leading Edge 18: 269–272.

Rybakov, M., Goldshmidt, V., Fleischer, L., Rotstein, Y. (1999b). Crystalline basement in central Israel derived from gravity and magnetic data. Isr. J. Earth Sci. 48: 101-111.

Rybakov, M., Goldshmidt, V., Fleischer, L., Ben-Gai, Y. (2000). 3-D gravity and magnetic interpretation for the Haifa Bay area (Israel). J. Applied Geophys 44: 353-367.

Rybakov, M., Goldshmid,t V., Fleische,r L., Rotstein, Y. (2001). Cave detection and 4-d monitoring: a microgravity case history near the Dead Sea. The Leading Edge 20: 896-900.

Rybakov, M., Shirman, B., Al-Zoubi, A., Rotshtein, Y. (2005). Cave detection near the Dead Sea- a micromagnetic feasibility study. The Leading Edge 24:585-590.

Rybakov, M., Goldshmidt, V., Hall, J., Ben-Avraham, Z., Lazar, M. (2011). New insights into the sources of magnetic anomalies in the Levant, Russian Geology and Geophysics 52: 377-397.

Sass, E. (1980). Late Cretaceous volcanism in Mt. Carmel, Israel. Isr. J. Earth Sci. 29: 8-24.

Schattner, U., Segev, A., Mikhailov, V., Rybakov, M., Lyakhovsky, V. (2019). Magnetic signature of the Kinneret–Kinarot tectonic basin along the Dead Sea Transform, northern Israel. Pure Appl. Geophys. pp 1-17, doi.org/10.1007/s00024-019-02211-6.

Segev, A., and Rybakov, M. (2010). Effects of Cretaceous plume and convergence, and Early Tertiary tectonomagmatic quiescence on the central and southern Levant continental margin. Journal of the Geological Society London 167: 731-749.

Segev, A., and Rybakov, M. (2011). History of faulting and magmatism in the Galilee (Israel) and across the Levant continental margin inferred from potential field data. Journal of Geodynamics 51: 264-284.

Segev, A., Goldshmidt, V., Rybakov, M. (1999). Late Precambrian- Cambrian tectonic setting of the crystalline basement in the northern Arabian-Nubian Shield as derived from gravity and magnetic data: Basin-and-range characteristics, Isr. J. Earth Sci. 48: 159-178.

Segev, A., Sass, E., Schattner, U. (2018). Age and structure of the Levant basin, Eastern Mediterranean, Earth-Science Reviews 182: 233-250.

Segev, A., Rybakov, M., Lyakhovsky, V., Hofstetter, A., Tibor, G., Goldshmidt, V., Ben-Avraham, Z. (2006). The structure, isostasy and gravity field of the Levant continental margin and the southeast Mediterranean area. Tectonophysics 425: 137-157.

Shirman, B. (2000). Three component magnetic anomaly maps of Israel, Isr. J. Earth Sci. 49: 1-7.

Shirman, B., and Rybakov, M. (2009). Sinkholes along the Dead Sea coast and their development, FIG Working Week, Surveyors Key Role in Accelerated Development, Technical Programme, Eilat, 3-8 May.

Smit, J., Brun, J., Cloetingh, S., Ben-Avraham, Z. (2009). The rift-like structure and asymmetry of the Dead Sea Fault, Earth Planet. Sci. Lett. 290: 1-9.

Tašárová, Z., Götze, H-J., El-Kelani, R., Ebbing, J., Hassouneh, M. (2006). Small-scale gravity modeling of upper crustal structures in the Araba Valley along the Dead Sea Transform. Geochemistry, Geophysics, Geosystems 7, Q09012, doi:10.1029/2005GC001229.

ten Brink, U., Schoenberg, N., Kovach, R., Ben-Avraham, Z. (1990). Uplift and a possible moho offset across the Dead Sea transform. Tectonophysics 180: 71-85.

ten Brink, U., Rybakov, M., Al-Zoubi, A., Rotstein, Y. (2007). Magnetic character of a large continental transform: An aeromagnetic survey of the Dead Sea Fault, Geochem. Geophys. Geosyst. 8, Q07005, doi:10.1029/2007GC001582.

ten Brink, U., Ben-Avraham, Z., Bell, R., Hassouneh, M., Coleman, D., Andreasen, G., Coakley, B. (1993). Structure of the Dead Sea pull-apart basin from gravity analyses. Journal of Geophysical Research: Solid Earth 98: 21877-21894.

ten Brink, U., Rybakov, M., Al Zoubi, A., Hassouneh, M., Frieslander, U., Batayneh, A., Goldschmidt, V., Daoud, M., Rotstein, Y., John, K., Hall, J. (1999). Anatomy of the Dead Sea transform: Does it reflect continuous changes in plate motion? Geology 27:887–890.

ten Brink, U., Al- Zoubi, A., Flores, C., Rotstein, Y., Qabbani, I., Harder, S., Keller, G. (2006). Seismic imaging of deep

low- velocity zone beneath the Dead Sea basin and transform fault: Implications for strain localization and crustal rigidity, Geophys. Res. Lett., 33, L24314, doi:10.1029/ 2006GL027890.

USGS (1998). United States Geological Survey, overview of Middle East water resources, https://www.usgs.gov/about/organization/science-support/international-programs.

Weber, M., and DESERT group (2009). Anatomy of the Dead Sea Transform from lithospheric to microscopic scale, Rev. Geophys. 47, RG2002, doi:10.1029/2008RG000264.

Woodside, J., and Bowin, C. (1970). Gravity anomalies and inferred crustal structure in the Eastern Mediterranean Sea. Geol. Soc. Am. Bull. 81: 1107–1122.

JJEES

JJEES (2020) 11 (1): 62-70
ISSN 1995-6681

Jordan Journal of Earth and Environmental Sciences

Spatial and Temporal Variability Analyses of Water Quality in Jaghjagh River, Syria

Rami Kaba[1*] and Ahmad Majar[2]

[1] General Commission for Scientific Agricultural Research (GCSAR), Al-Qamishli Agricultural Research Center, Al-Qamishli, Syria.
[2] General Commission for Scientific Agricultural Research (GCSAR), Damascus, Syria.

Received 23 July 2019, Accepted 29 October 2019

Abstract

Intensively used for irrigation, the Jaghjagh River in the northeastern region of Syria is polluted by municipal and industrial wastewaters. This study is aimed at assessing the spatial and temporal changes in the water quality of the Jaghjagh River in order to evaluate the existence of any potential impact of the water of the river used for irrigation and agriculture. Monthly water samples were collected regularly during the years 2012-2013 from three locations that are 2 km apart. The samples were analyzed for physicochemical characteristics. The results of the analysis showed that water quality parameters varied spatially and temporally. The spatial variation of the parameters was clearly shown at the location from 1 to 3, and the significant difference of SS, EC, TDS, CODcr, BOD5, PO43-, Cl- and NH4+ was obvious at location 3 compared to the values at locations 1 and 2, reaching the values of 56.6 mg/l, 744.0 µS/cm, 326.5 mg/l, 111.7 mg/l, 10.57mg/l, 99.4 mg/l and 22.17 mg/l respectively, while Nitrate demonstrated decreasing values at locations 1 to 3. Depending on the seasonal stream flow in winter (high rainfall) and summer (no rainfall), the temporal variation with significant difference was clearly recognized for the following parameters EC, TDS, PO43- . NH4+ and Cl- reached the values of 670.0 µS/cm, 329.4 mg/l, 9.30 mg/l, 4.22 mg/l and 15.0 mg/l respectively. So to improve the water quality of the Jaghjagh River, basin management and treatment of municipal and industrial wastewaters are recommended. Moreover, further detailed studies of spatial and temporal modelling and prediction are required.

Keywords: Jaghjagh River, irrigation, pollution, Syria, wastewater

1. Introduction

The importance of rivers and surface water resources for communities has been recognized and stressed by several authors (Priscoli, 1998; Khadse et al., 2008). For this reason, most cities, industrial centers, and agricultural activities were established very close to streams and other surface water resources (FAO, 2011). As a result of the rapid population growth and climate change (Al-Dabbas, et al., 2018), water quality has become an important issue in recent years. The provision of drinking and irrigation water faces major challenges, including the shortage of water and the poor quality of the waters (Al-Ansari, 2013). Water pollution, whether from sewage, industrial waste, or chemicals used in agriculture such as pesticides and fertilizers, has led to a lack of adequate water for domestic, industrial, and agricultural needs (ESCWA, 2000). Due to the intense development of industry and agriculture, the water ecosystem has been perceptibly altered in several respects in recent years. Today, water resources are exposed to a variety of local disturbances across the globe (Vencatesan, 2007). Often, wastewater is drained into rivers, valleys, and agricultural land without treatment, especially in third world countries due to the high costs of processing and treatment (FAO, 2003; Hussein et al., 2004). Wastewater brings with it significant quantities of organic and inorganic pollutants to the water bodies and agricultural soils (Feizi, 2001; Wang et al., 2003; Hussain et al., 2006).

In several arid and semi-arid countries, water deficits have forced planners and decision-makers to utilize any available source of water that can be used cheaply to encourage further development. This has led to a decline in freshwater sources in most Mediterranean regions and an urgent need to preserve and protect those resources (Bahri, 2002). Population growth, climate change, drought, and the increasing demand for water resources have added greater pressure on water resources while simultaneously impairing surface water quality as a result of pollution discharge from industrial and agricultural activities (IPCC, 2007; Razzaghmanesh et al., 2005). On the whole, spatial variation in river water quality is motivated by natural catchment characteristics (e.g., climate, geology, soil type, topography, and hydrology) and also by human undertakings within catchments (e.g., Land use and management, plants cover etc.) (Lintern et al., 2018). However, the capability to manage and decrease water quality effects is disadvantaged by the variability in water quality both spatially and temporally, and the incapacity to expect this variability. (Ai et al., 2015). So, in order to develop operative management strategies for rivers' water quality, it is critical to be able to predict these spatio-temporal variabilities (Danlu el at, 2019).

According to spatial and temporal changes in the water quality of the river, the situation requires the development of an integrated program to monitor the physicochemical variables at different locations along the river in order

* Corresponding author e-mail: kaba.rami@gmail.com

to draw a clear map of the water quality (Kenneth, 2003). Therefore, water quality monitoring is critical for ensuring that water resources are managed correctly and remain within the acceptable limits for sustainable use. The agricultural lands in some villages of Al-Qamishli region are haphazardly irrigated by water from the Jaghjagh River without awareness of the impact of irrigation with this water quality on soil management, crops, and the wider social and natural environments. The aim of this research is to estimate the spatial and temporal changes in water quality of the Jaghjagh River within the Al-Qamishli region and to evaluate its potential impact on agriculture and irrigation.

2. Materials and Method

2.1 Study area

The Jaghjagh River is a small perennial in eastern North Syria, flowing from Turkey through the city of Al-Qamishli and continuing its path to the city of Al-Hasakah where it reaches its estuary at Khabur River. The sewage and solid wastes are dumped into the river from the cities of Nisibin and Al-Qamishli.

The climate in this region is semi-arid with an average annual rainfall of about 442 mm, a major part of which is received during the winter season.

2.2 River Water Sampling

Water samples were collected from three locations with a distance of 2 km between each sampling location (Figure 1), with coordinates illustrated in (Table 1), over a period of twenty-four months from January 2012 to December 2013. The monthly samples of the subsurface water were collected in triplicates during the first week of each month in the early hours of the day (7 a.m. to 9 a.m.). Iodine-treated double Stoppard polyethylene bottles were used for the collection of the water samples, which were kept in an ice bucket and brought to the laboratory for analysis. Some of the physicochemical characteristics of water, such as temperature and pH were measured using a mercury thermometer and digital pH-meter, respectively; other parameters including turbidity, electrical conductivity, total dissolved solids, nitrate-nitrogen, phosphates, biochemical oxygen demand, chemical oxygen demand, ammonia, were analyzed in the laboratory within six to eight hours using the methods of APHA (1985). Figure 2 illustrates the sampling locations selected for this study.

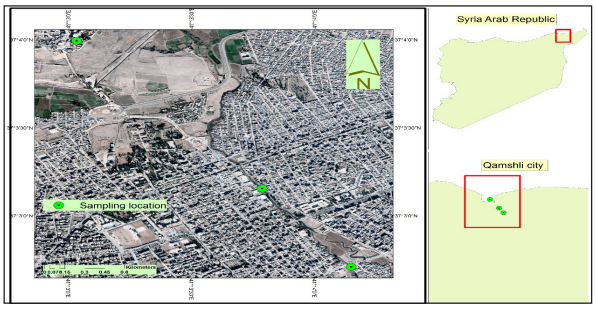

Figure 1. The sampling locations from Jaghjagh River in eastern North Syria.

Table 1. Coordinates of sampling locations

Sampling Location		Coordinates
1	river to the Syrian boundaries the beginning of entering the	Latitude: 37° 3’59.62”N
		Longitude: 41°13’32.07”E
2	2 km away from the previous location, the centre of the town, intensive sewage and industrial water is thrown into the river.	Latitude: 37° 3’9.35”N
		Longitude: 41°13’47.25”E
3	2 km away from the second location, industrial area.	Latitude: 37° 2’42.67”N
		Longitude: 41°14’8.94”E

Figure 2. Photos of some water sampling locations. (Source: Dr.Rami Kaba)

3. Results and Discussion

The range of variation and their annual mean along with a standard deviation of various physico-chemical characteristics of Jaghjagh River water are given in Table 2. Spatial variations are shown in Table 3. A seasonal variation is shown in Table 4. The monthly variations in water quality are depicted in Figures 3 to 12, while the correlation coefficients between different parameters are presented in Table 5. The high standard deviation indicates that the data are widely spread, due to the presence of temporal variations caused likely by natural and/or anthropogenic polluting sources.

Table 2. Range of variation, mean, and standard deviation of water quality parameters of the Jaghjagh River water

Parameters	2012			2013		
	Range of variation		Mean and Standard deviation	Range of variation		Mean and Standard Deviation
	Minimum	Maximum		Minimum	Maximum	
Ta	12	46	23.29±10.24	11.0	41.0	20.96±6.54
Tw	9.1	32.1	20.29±6.93	10.0	33.0	22.81±10.05
SS	7	124	26.94±26.11	8.0	129.0	33.78±30.58
pH	6.8	8.1	7.436±0.320	6.9	7.9	7.372±0.258
EC	370.0	1056.0	593.0±175.9	373.0	1022.0	594.3±178.5
TDS	171.0	500.0	282.1±79.6	220.0	509.0	292.1±59.9
COD_{cr}	4.0	290.0	71.7±75.8	14.0	367.0	60.5±70.5
BOD_5	2.00	155.00	40.36±43.51	3.00	150.00	29.94±32.94
Nitrate NO_3^-	0.00	16.90	2.856±4.535	0.100	11.00	1.978±2.382
PO_4^{-3}	0.13	29.10	5.69±6.94	0.200	22.40	6.395±6.139
Cl^-	4.0	410.0	44.7±73.9	17.0	519.0	53.0±87.7
NH_4^+	1.0	55.0	12.00±12.9	1.0	54.0	12.56±12.40

Where Ta is Air Temperature, °C , Tw is Water Temperature, °C, SS is Suspended Solids mg/l, EC is Electrical Conductivity, µS/cm, TDS is Total Dissolved Substance, mg/l, CODcr is Chemical Oxygen Demand, mg/l, BOD5 is Biological Oxygen mg/l, NO3- is Nitrate, PO4-3 is Phosphate, mg/l, Cl- is chloride, mg/l, NH4+ is Ammunium,mg/l.

Table 3. Spatial variations of water quality parameters during the study period.

Sampling Locations				
Parameters	**1 Loc.**	**2 Loc.**	**3 Loc.**	**LSD 95%**
Ta	22.42a	22.52a	23.48b	0.721
Tw	20.37a	20.13a	21.36b	0.622
SS	16.3a	18.1a	56.6b	11.34
pH	7.48a	7.4a	7.39a	0.1254
EC	506a	531a	744b	60.5
TDS	267.6a	267.2a	326.5b	26.86
COD_{cr}	56.4a	49.6a	111.7b	29.96
BOD_5	22.9a	23.1a	59.4b	14.09
Nitrate	3.15a	2.40ba	1.70cb	1.252
PO_4^{3-}	3.74a	3.82a	10.57b	2.666
CL^-	22.6a	24.5a	99.4b	42.59
NH_4^+	7.53a	7.14a	22.17b	4.31

Table 4. Seasonal variations of water quality parameters during the study period

	Seasonal variations				
Parameters	Winter	Spring	Summer	Autumn	LSD 95%
Ta	13.05a	21.50b	35.92c	20.75b	4.346
Tw	14.24a	20.62b	28.13c	19.50b	3.027
SS	35.0a	24.1a	35.3a	27.1a	14.47
pH	7.36bc	7.59a	7.23c	7.42b	0.159
EC	479a	611b	670b	632b	88.6
TDS	242.4a	270.3b	329.4c	306.2bc	38.51
COD_{cr}	64.4a	51.9a	81.9a	92.1a	45.18
BOD_5	31.0a	32.3a	37.8a	39.5a	22.11
Nitrate	0.72a	1.08a	4.22b	3.64b	2.347
PO_4^{-3}	4.91a	4.45a	9.30b	5.52a	1.467
CL^-	27.1a	77.4b	49.7a	41.1a	49.10
NH_4^+	9.9a	11.1ab	15.0cb	13.2ab	5.75

Table 5. Correlation Coefficient (r) by Pearson among physicochemical parameters of the Jaghjagh river water.

	Ta	Tw	SS	pH	EC	TDS	CODcr	BOD_5	Nitrate	PO_4^{-3}	CL^-	NH_3-N
Ta	1											
Tw	0.878**	1										
SS	0.091	0.073	1									
pH	-0.234*	-0.247*	-0.057	1								
EC	0.363**	0.482**	0.537**	-0.115	1							
TDS	0.425**	0.558**	0.554**	-0.196	0.77**	1						
COD_{cr}	0.21	0.296*	0.640**	-0.065	0.553**	0.731**	1					
BOD_5	0.198	0.271*	0.628**	-0.072	0.655**	0.64**	0.874**	1				
Nitrate	0.26*	0.38**	-0.097	-0.082	0.084	0.198	0.059	0.013	1			
PO_4^{-3}	0.287*	0.306**	0.685**	-0.126	0.641**	0.628**	0.601**	0.635**	0.119	1		
CL^-	0.176	0.115	0.485**	-0.013	0.659**	0.494**	0.421**	0.579**	-0.05	0.436**	1	
$NH4^+$	0.194	0.286*	0.724**	-0.048	0.751**	0.647**	0.707**	0.827**	0.11	0.81**	0.55**	1

** *Correlation is significant at 0.05 significance level (2-tailed).*

3.1. Suspended solids (SS)

Clay, silt, organic matter, plankton, and other microscopic organisms cause turbidity in natural waters (Kishor and Joshi, 2005). The average measured SS varied between 7-124 mg/l and 9-129 mg/l in 2012 and 2013 respectively. Spatial variation among the locations was demonstrated clearly at location 3, where the concentration of 56.6 mg/l has a significant difference compared to other locations (Table 3). No temporal variation was noticed, and the seasonal average SS increased apparently in winter and summer with values of 35.0 and 35.3 mg/l (Table 4). Additionally, its values displayed a positive correlation with the values of EC, TDS, CODcr, BOD5, PO43-, chloride, NH4+ and a negative correlation with nitrate (Table 5).

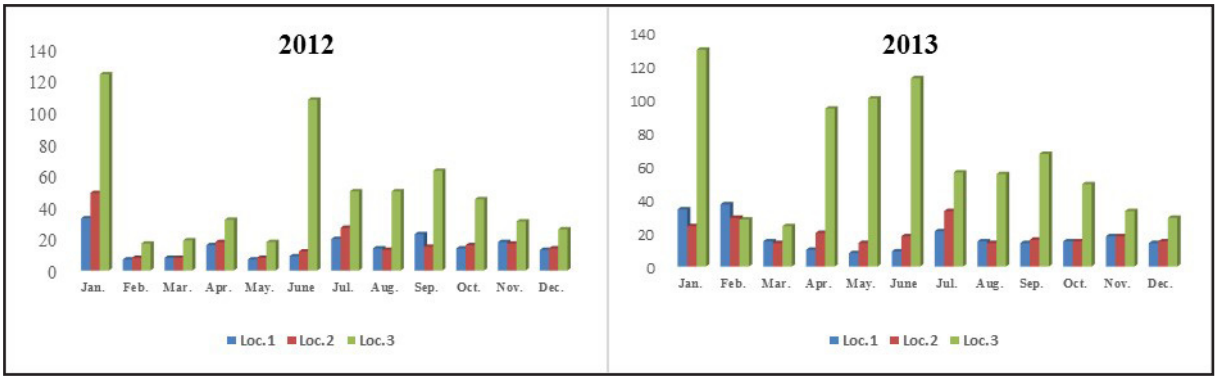

Figure 3. Monthly variations in Suspended solids (SS).

3.2. pH

pH is an important factor for realizing the nature and extent of pollution. pH values of Jaghjagh River water varied during the study period from slightly acidic to slightly alkaline levels of 6.8 and 8.1 (Table 2). Khadse et al. (2008) reported that higher pH values are often caused by bicarbonates and carbonates. The average pH values did not show a statistically significant difference among the sampling locations (Table 3). According to the seasonal variation, pH varied between 7.23 and 7.59 in summer and spring respectively; moreover, there was a significant difference among them (Table 4). In accordance with the correlation matrix, it was observed that pH was negatively related to the temperature (Table 5). The pH values ranged from 6.8 in July to 8.1 in March of 2012 and ranged between 6.9 in May and 7.9 in April of 2013 (Figure 4). The pH increase is related to rainfall runoff which brought waste with, but it did not exceed the acceptable standards of sewage water for irrigation proposes (Syrian Standards limitations, 2008).

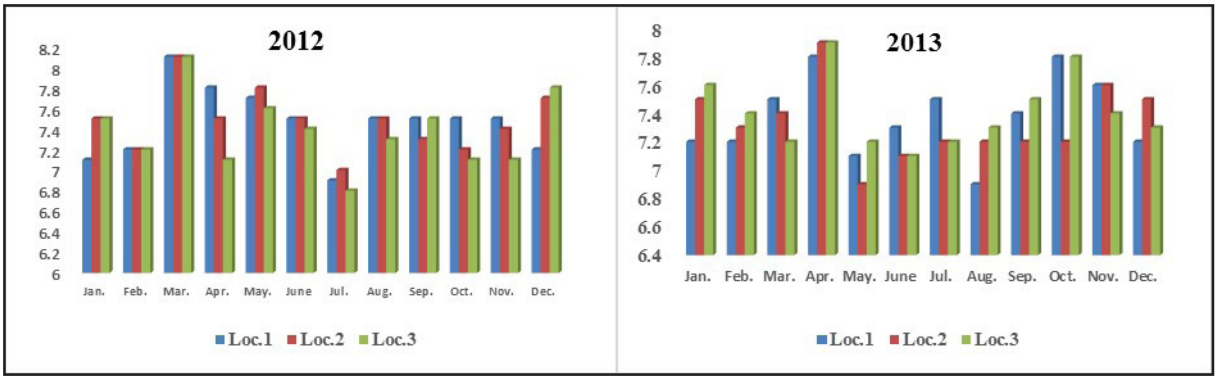

Figure 4. Monthly variations in water pH.

3.3. Electrical Conductivity

Spatial variation of EC showed a rage of values between 506 and 744 µS/cm. The values observed at location 3 varied significantly compared to the sampling locations 1 and 2 (Table 3). However, seasonal variation showed significant differences in the values in spring, summer, and autumn compared to winter with values of 611, 670, 632 and 479 µS/cm respectively (Table 4). This was because of the wide variety of inorganic salts and organic matter resulting from natural conditions and agricultural runoff (Basu and Lokesh, 2013). In accordance with the correlation matrix, EC demonstrated a positive correlation with temperature, SS, TDS, CODcr, BOD5, PO43-, chloride, and NH4+ and a negative correlation with pH. According to the Syrian Standardization, the parameter EC was within the acceptable standards for irrigation purposes.

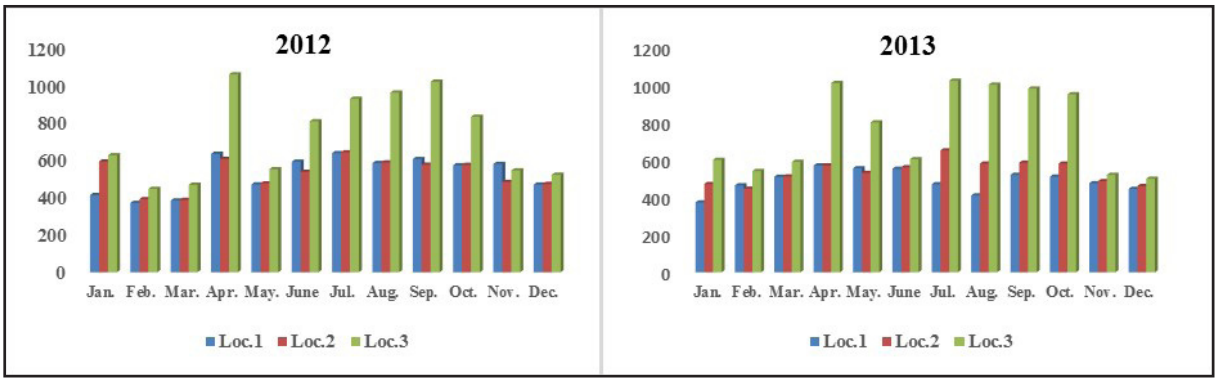

Figure 5. Monthly variations in electrical conductivity of water.

3.4. Total Dissolved Substance

The average TDS value varied between 267.6 mg/l and 326 mg/l at the sampling locations, especially location 3 which showed a significant difference compared the other sampling locations. A higher value of TDS was observed in summer (the dry season) and lower values were observed in winter (the rainy season) with values of 3 29.2 and 242.4 mg/l demonstrating a significant difference between them, because the seasonal variation in the major ion concentrations and TDS of the water are usually governed by river runoff variations (Khazheeva et al., 2007). The TDS parameters showed a positive correlation with the parameters of temperature, SS, EC, CODcr, BOD5, PO43-, chloride and NH4+, and a negative correlation with pH (Table 5).

Figure 6. Monthly variations in TDS of water.

3.5. Chemical Oxygen Demand

The Chemical Oxygen Demand (CODcr) is the measurement of oxygen required for the oxidation of organic matter in the samples, and being a reliable parameter for judging the extent of pollution in water (Amirkolaie, 2008), it is widely used for determining the waste concentration (Kazi et al., 2009). In the present study, CODcr ranged from 4 mg/l (March 2012) to 367 mg/l (January 2013) (Figure8). According to the results presented in Table 3, there was a significant spatial variation demonstrated at location 3 with values of 111.7 mg/l compared to locations 1 and 2. This reflects the observations made by Garg et al. in a reservoir in India (2010). The highest value was obtained at sampling location 3 (367 mg/l), where there were intensive discharges of domestic and industrial wastewater dumped into the river. Furthermore, the COD_{cr} values demonstrated a positive correlation with the parameters of temperature, SS, EC, TDS, BOD5, PO_4^{3-}, Chloride and NH_4^+ (Table 5), indicating that the COD^{cr} could be related to the leaching and transport of natural, domestic sewage, agricultural and industrial pollutants as observed by Barakata et al. (2016). The mean consternation of COD_{cr} was higher than the maximum limit permitted by the Syrian Standardization for the irrigation of cooked vegetables.

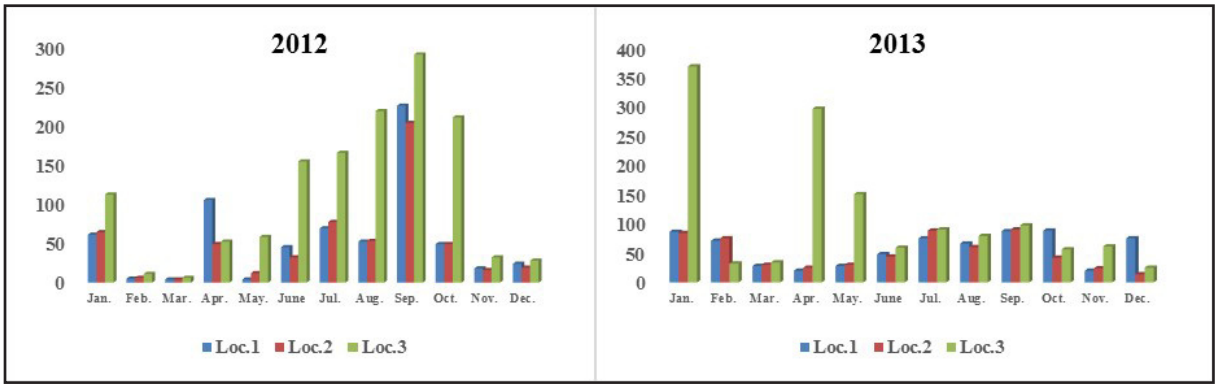

Figure 7. Monthly variations in chemical oxygen demand (CODcr)

3.6. Biochemical Oxygen Demand

The significant spatial variation was noticed at location 3 with values of 59.4 mg/l compared to values at locations 1 and 2 (Table 3). No significant temporal variation was noticed according to the results in (Table 4). The highest BOD5 was recorded during the months of January, April, July, August, and September, and the lowest values were recorded in the months of February, March, November, October, and December in all of the sampling locations (Figure 8). This may be related to the high biological activity stimulated by the rising temperature. Similar results were reported by Sreenivasulu et al. (2014) and Issa (2013). BOD5 values demonstrated a positive correlation with water temperature, SS, EC, TDS, COD, PO43-, Chloride and NH4+ (Table 4). Compared to the Syrian standards, all locations showed a moderately to highly polluted quality in more than 50% of the samples, especially at location 3.

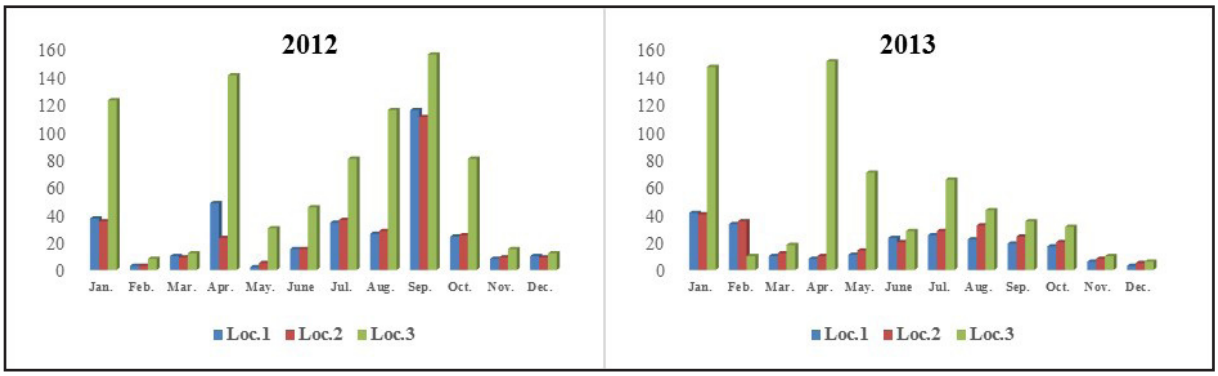

Figure 8. Monthly variations in biochemical oxygen demand (BOD5)

3.7. Nitrate

Nitrate concentrations varied at locations from 1 to 3 with a maximum value of 3.15 mg/l at location 1 which demonstrated a significant difference compared to the values at location 3 (Table 3). This is related to the intensive fertilization processes of the agricultural lands adjacent to location 1. Significant Seasonal variations in the nitrate concentration were noticed in summer and autumn with the values of 4.22 and 3.64 mg/l respectively, compared to lesser concentrations in winter and spring (Table 4). Pejman et al. (2009) stated that nitrate values should be of higher values in warm seasons, which may be justified by the relatively more agricultural and husbandry activities, as is clearly demonstrated by Figure 9. According to the Syrian Standardization, the nitrate content in all of the water samples were within the allowable concentrations for irrigation purposes.

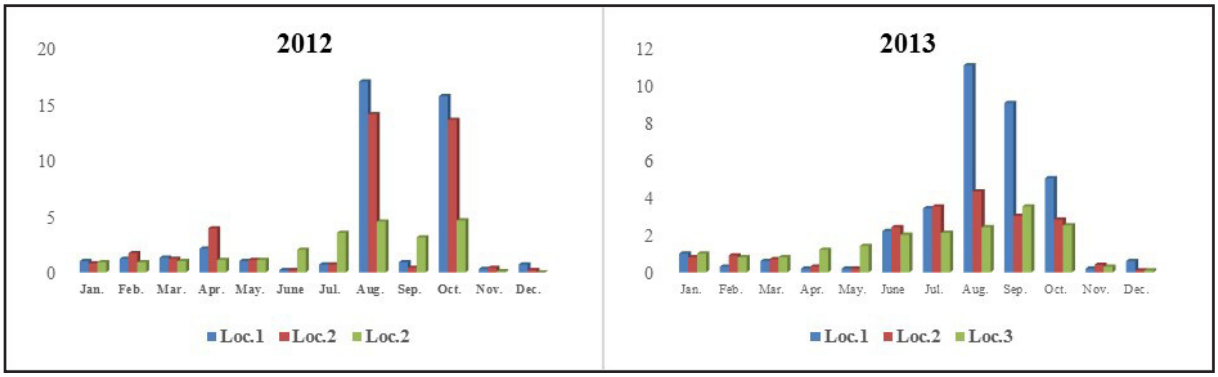

Figure 9. Monthly variations in nitrate (NO3-)

3.8. Phosphate

Phosphate concentrations ranged from 0.13 to 29.1 mg/l in 2012, and from 0.2 to 22.4 in 2013, with the highest value (10.57 mg/l) being recorded at the location 3 demonstrating a significant difference compared to locations 1 and 2 (Table 3). This is due to the mixing of domestic waste and different industries' effluents with agriculture runoff from the farmlands (Groupement ADI/CACG, 2010). From a season-based evaluation, it was noticed, that due to high evaporation, the Phosphate value of 9.30 mg/l shows a significant difference in summer compared to the values in other seasons, and this is well-matched with the findings of Garg et al. (2010). Phosphate correlated reasonably well with temperature, SS, EC, pH, TDS, CODcr, BOD5, Nitrate, Chloride and NH4+. According to the Syrian Standardization of wastewater for irrigation, the higher values of Phosphate observed at location 3 during the months of January, August, and October of 2012 and 2013 respectively (Figure 10) have exceeded the maximum limits allowed for irrigation.

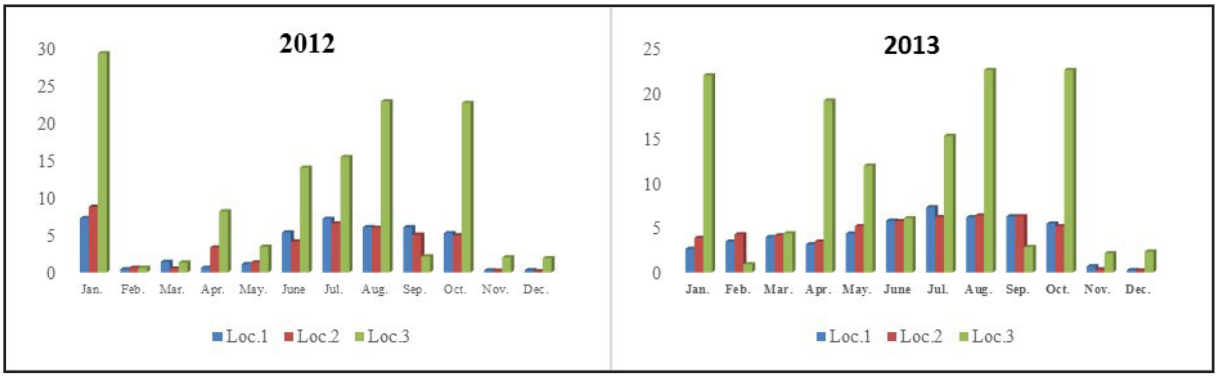

Figure 10. Monthly variations in Phosphate

3.9. Chloride

Chloride spatial variation was clearly observed among locations, where the average value of 99.4 mg/l recorded at the location 3 exhibit a significant difference in comparison to other locations. Seasonal variation, which was clearly demonstrated in spring when domestic and industrial wastewater inlets are the highest, showed a statistically significant difference with the value of 77.4 mg/l compared to the values in winter only. This can be explained in terms of the climatologic and hydrologic characteristics associated with the wet (cold or temperate) and dry (warm) seasons (Zare et al., 2011). The chloride concentration had not exceeded the maximum limit allowed by the Syrian Standards for irrigation at sampling locations 1 and 2 in 2012 and 2013. However, the concentration of chloride obtained at location 3 in April of 2013 (Figure 11) had exceeded the allowable irrigation limits of all crops, vegetables, trees and the surfaces of green types.

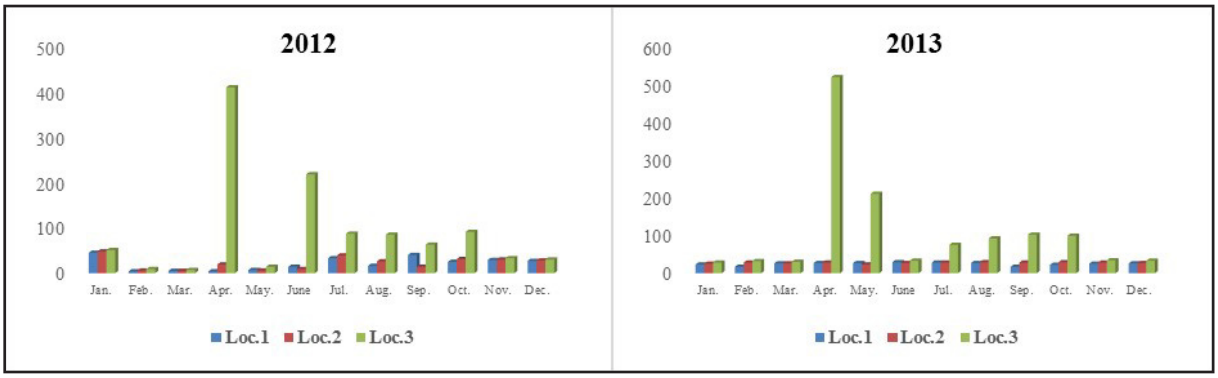

Figure 11. Monthly variations in Chloride.

3.10. Ammonium

Ammonium (NH4+) values varied spatially among locations with the highest value of 22.1 mg/l being recorded at location 3, where the downstream of Al-Qamishli region wastewater discharges are situated indicating a moderate to high pollution of the riverwater; this showed the negative impact of discharges from the city on the quality of the water of the studied river (Barakata et al., 2016), with significant differences compared to others. However, temporal variations were not observed during the study period. In accordance with the correlation matrix, ammonium displayed a positive correlation with SS, EC, TDS, CODcr, nitrate, BOD5, PO4-3, and Chloride, (Table 5). The Ammonium concentrations exceeded the allowable Syrian limits for irrigation concerning all type of crops being forest or fruit trees or cereals and forage and also cooked vegetables during the months from July to September in 2012 and 2013 respectively at location 3 (Figure 12).

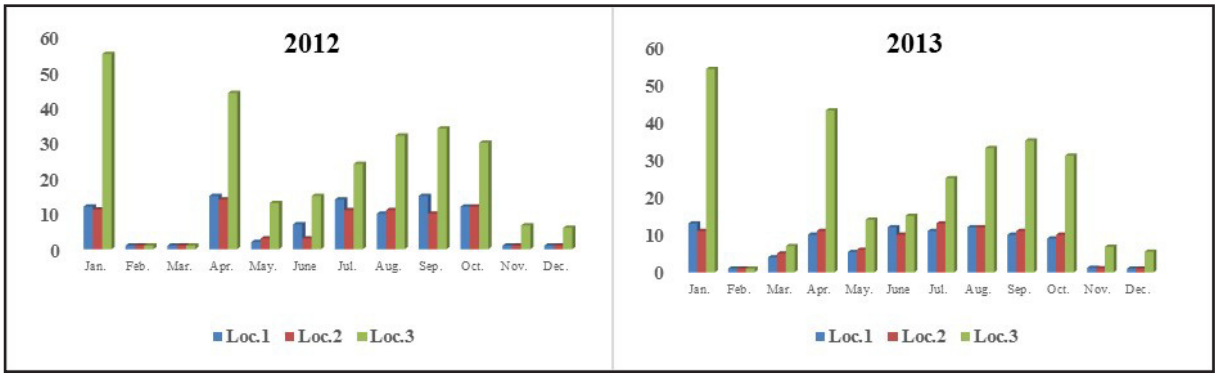

Figure 12. Monthly variations in Ammonium

4. Conclusions and Recommendations

According to the Syrian standards for pH, electrical conductivity, total salts, chloride, and nitrate, there were no restrictions on the use of water for irrigation purposes. However, there was a rise of CODcr and BOD5 values in all three locations, as a result of the industrial waste, fertilizers, and agricultural pesticides, dumped directly into the river without treatment. Due to the high values of ammonium NH4+, the water of the river at the third location in the runoff season was close to being a threatening water quality for the irrigation of cooked vegetables, fruits, fodder, and grains. Therefore, it is critical to monitor water quality and the river discharge continuously. This study recommends controlling the cultivation of vegetable crops especially freshly eaten crops, which are directly irrigated by the water of the river. This study also recommends raising environmental awareness and guiding farmers on adjacent territories to grow more fodder crops, which increase their income and strengthen the environmental cleanness. Moreover, more works on modeling and the prediction of the spatial and temporal variability of the river water quality are required.

References

Ai, L., Shi, Z. H., Yin, W., Huang, X. (2015). Spatial and seasonal patterns in stream water contamination across mountainous watersheds: Linkage with landscape characteristics. Journal of Hydrology 523: 398-408. doi.org/10.1016/j.jhydrol.2015.01.082.

Al-Ansari, N. (2013). Management of water resources in Iraq. Journal of Scientific Research, Engineering, Perspectives and prognoses, Lulea Univ. 5: 667-684.

Al-Dabbas, M.A., Al-Shamma'a, A.M., Al-Mutawki K.G. (2018). Evaluation of Gharraf River Water for different Uses, South Iraq. Iraqi Journal of Science 59(3): 1697-1709.

Amirkolaie, A.K. (2008). Environmental Impact of Nutrient Discharged by Aquaculture Waste Water on the Haraz River. J. Fish Aquat. Sci. 3: 275-279.

APHA (1985). Standard methods for the examination of water and wastewater, 16th ed., New York. aquatique. BTI Ministere de l'agriculture 224–881.

Bahri, A. (2002). Wastewater Reuse in Tunisia: Stakes and Prospects. National Institute for Research on Agricultural Engineering, Water and Forestry 2002; BP10, Ariana 2080, Tunisia.

Barakata, A., Mohamed, E.B., Jamila, R., Brahim A., Mohamed S. (2016). Assessment of spatial and seasonal water quality variation of OumErRbia River (Morocco) using multivariate statistical techniques. International Soil and Water. Conservation Research 4: 284–292.

Basu, S., and Lokesh, K.S. (2013). Spatial and temporal variations of river water quality: a case study of River Kabini at Nanjangud in Karnataka. Int. J. Water Resour. Environ. Eng. 5(10): 591-596.

Danlu Guo1, Lintern A., Webb J.A., Ryu D., Bende-Michl U., Liu S., Western A.W. (2019). A predictive model for spatio-temporal variability in stream water quality. Hydrol. Earth Syst. Sci. https://doi.org/10.5194/hess-2019-342.

ESCWA (2000). Application of Sustainable Development Indicators in ESCWA Member Countries: Analysis of Results. (E/ESCWA/ED/2000/4). P.22.

FAO (2011). The State of the World's h Land and Water Resources for Food and Agriculture (SOLAW) – Managing Systems at Risk. Food and Agriculture Organization of the United Nations, Rome and Earthscan, London.

FAO (2003). User Manual for Irrigation with Wastewater. FAO Regional Office for the Near East Cairo.

Feizi, M. (2001). Effect of Treated Wastewater on Accumulation of Heavy Metals in Plants and Soil. ICID International Workshop on Wastewater Reuse Management. Seoul. Rep. Korea. 19, 20 September.

Workshop on Wastewater Reuse and Management, Seoul, Korea. 137-146

Garg, R.K., Rao R.J., Uchchariya, D., Shukla, G., Saksena, D.N. (2010). Seasonal variations in water quality and major threats to Ramsagar reservoir, India. African Journal of Environmental Science and Technology 4(2): 61-76.

Groupement ADI/CACG (2010). Etude d′actualisation du PDAIRE de la zone d′actiondel′Agence du BassinHydraulique de l′OumErRbia.

Hussain, S.I., Ghafoor, A., Ahmad, S., Murtaza, G., Sabir, M. (2006). Irrigation of crops with raw sewage. Hazard assessment of effluent. Soil and vegetables. Pak. J Agri. Sci. 43(3-4): 97-102.

Hussein, H.F., Saber, M.S.M., Radwan, S.M.A., Abu-Seda, M. (2004). Use of Treated Domestic Sewage Effluent for Growing Summer Oil Crops in Arid Lands. International Conf. on Water Resources and Arid Environment P. 95-112.

IPCC (2007). Climate change 2007, impacts, adaptation and vulnerability. Working Group II to the Fourth Assessment Report of the IPCC.

Issa, R. (2013). DO, BOD Water Quality Modelling for al Kabeeralshemaly River Using QUAL2K. Tishreen University Journal for Research and Scientific Studies - Engineering Sciences Series 35(8): 189 - 208.

Lintern, A., Webb, J. A., Ryu, D., Liu, S., Bende-Michl, U., Waters, D., Leahy, P., Wilson, P., Western, A. W. (2018). Key factors influencing differences in stream water quality across space. WIREs Water 2018, 5:e1260. doi: 10.1002/wat2.1260.

Sreenivasulu, K., Kaizer, H., Damodharam, T. (2014). Seasonal variations in water quality and major threats to nellorecheruvu (tank), Nellore district, India. International journal of environment 3 (2): 28-53.

Kazi, T.G., Arain, M.B., Jamali, M.K., Jalbani, N., Afridi, H.I., Sarfraz, R.A., Shah, A.Q. (2009). Assessment of water quality of polluted lake using multivariate statistical techniques: A case study. Ecotoxicology and Environmental Safety 72(20): 301–309.

Kenneth, M.V. (2003). An Introduction to Water Quality and Water Pollution Control. Press edition, 2 Ed. p9.

Khadse G.K., Patni P.M., Kelker P.S., Devetta S. (2008). Qualitative evaluation of Kanhan river and its tributaries flowing over central Indian Plateau', Environmental Monitoring and Assessment 147: 83-92.

Khazheeva, Z.I., Tulokhonov, A.K., Dashibalova, L.T. (2007). Seasonal and spatial dynamics of TDS and major ions in the Selenga River. Water Res. 34(4): 444–449.

Kishor, K., and Joshi B.D.D. (2005). Physico-chemical characteristics of pond water at Khanpur village in Bareilly district (U.P.). Him. J. Environ. Zool. 19: 89-92.

Pejman, A.H., NabiBidhendi, G.R., Karbassi, A.R., Mehrdadi, N., EsmaeiliBidhendi, M. (2009). Evaluation of spatial and seasonal variations in surface water quality using multivariate statistical techniques. Int. J. Environ. Sci.Technol. 6(3): 467-476.

Priscoli, J.D. (1998). Water and civilization: using history to reframe water policy debates and to build a new ecological realism. Water Policy 1: 623–636.

Razzaghmanesh, M., Mohammadi, K., Samani, J.M.V. (2005). A river quality simulation using WASP6: case study. 9th Environmental Engineering Specialty Conference, Toronto, Ontario, Canada. 2nd–4th June.

Syrian Standards limitations (2008). Maximum permissible Limits of Syrian Standardization of Wastewater for irrigation proposes. N (2752).

Vencatesan, J. (2007). Protecting Wetlands. Current Sci. 93: 288-290.

Wang, Z., Chang, A.C., Wu, L., Crowley, D. (2003). Assessing the Soil Quality of Long-Term Reclaimed Wastewater-Irrigated Cropland. Geoderma 114: 261-278.

WHO (World Health Organization) (2008). Guidelines for drinking water quality, 3rd edition Geneva: World Health Organization. P. 1– 666.

Zare, G., Sheikh, V., Sadoddin, A. (2011). Assessment of seasonal variations of chemical characteristics in surface water using multivariate statistical methods. Int. J. Environ. Sci. tech. 8(3): 581-592.

JJEES

JJEES (2020) 11 (1): 71-76
ISSN 1995-6681

Jordan Journal of Earth and Environmental Sciences

A Microbiological and Physicochemical Assessment of Top Soils from Makeshift Open Waste Dumpsites in the Premises of some Schools in Benin City

[1*]Aimuanmwosa Eghomwanre, [1]Nosa Obayagbona, [2]Covenant Ilontumhan

1University of Benin, Faculty of Life Sciences, Department of Environmental Management and Toxicology, Nigeria
2Federal University of Agriculture, College of Environmental Resources Management Department of Environmental Management and toxicology, Nigeria

Received 28 March 2019, Accepted 2 November 2019

Abstract

A major factor which has contributed to the declining environmental and health conditions of urban communities is the indiscriminate dumping of solid waste in premises of public institutions such as public schools. The microbiological and physicochemical properties of surface soil samples obtained from twelve (12) waste dumpsites located in public schools across Benin City, Edo State were assessed using standard procedures. Sampling was conducted between the months of May and July 2018. The mean heterotrophic bacterial and fungi counts for the soil samples ranged from 2.81 ± 1.01 to 6.38 ± 1.78 ($\times 10^4$cfu/g) and 2.00 ± 0.73 to 7.03 ± 0.86 ($\times 10^3$cfu/g), respectively. Ten microbial isolates were tentatively identified as follows: Acinetobacter sp., Pseudomonas aeruginosa, Micrococcus sp., Bacillus sp., Klebsiella sp., Enterobacter sp., Aspergillus niger, Penicillium sp., Mucor sp., and Fusarium sp. Pseudomonas sp. was the most dominant (16.00%) amongst the bacterial isolates, whilst Enterobacter sp (4.00%) was the least occurring bacterial isolate. Aspergillus sp. (17.00%) was the highest occurring fungal isolate, while the Fusarium sp. (8.00%) was the least. The mean concentration of the physicochemical results showed values which ranged from 5.82 ± 1.58 to 6.72 ± 1.17, 77.22 ± 6.14 ± 2.00 to 259.67 ± 64.34 µS/cm, 2.26 ± 0.53 to 5.83 ± 1.18 mg/kg, 29.11 ± 16.11 to 60.06 ± 10.76 mg/kg, 13.99 ± 3.22 to 33.57 ± 26.57 mg/kg, 6.42 ± 0.46 to 13.91 ± 2.43 mg/kg, 1.44 ± 0.72 to 3.83 ± 2.47%, 2.28 ± 0.69 to 6.71 ± 4.05% for pH, electrical conductivity (EC), Sulphate (SO^-_4), Nitrate (NO^-_3), Phosphate (PO_4^{-3}), Ammonium (NH_4^+), Total Organic Carbon (TOC) and Total Organic Matter (TOM), respectively. There was a significant difference between the values of most of the physicochemical parameters of the soil from the dumpsites and control sites. The presence of potential pathogenic microorganisms in the soils collected from the respective dumpsites is a major public health risk.

Keywords: Public schools, dumpsites, physicochemical, microbial and Benin City

1. Introduction

Solid wastes may be regarded as any material resulting from domestic activity and industrial operations for which there is no economic value and thus must be disposed (Sridhar, 1998). Population growth, economic development and urbanization have led to the increase and complexity of waste generated by urban areas dwellers (Verge and Rowe, 2013). Solid waste pollutants are known to serve as an external force which may have an impact on the physicochemical characteristics of soil, and as such can contribute to the poor production of vegetation (Christensen et al., 2014). Improper waste disposal in public schools in Nigeria has become a matter of public health concern for stakeholders such as civil society groups. Most public schools in Nigeria generate solid waste from daily activities such as classwork, sweeping, serving of food, clearing and bush burning. Open dumpsites are common practice in public schools due to insufficient or lack of waste disposal facilities. The common types of solid wastes found in the various schools include paper, grass, nylon (for sachet water, ice cream, sweets), corn cobs, groundnut shells, organic waste, cartons, tree leaves, steel cans, plastic bottles, and chalk (Wahab, 2003). Other forms of solid wastes, which are not directly generated by the students or teachers, but from neighboring residential premises, are also dumped at these sites. The continued increase in the quantity of waste generated in schools may not be unconnected with the increase in the number of students enrolled in schools yearly, improved living standards, urbanization, and technological advancement. Poor waste handling and disposal in schools especially where sanitation facilities are poorly planned and constructed, badly maintained and not properly deployed can lead to environmental pollution. This can further encourage the breeding of insects, animal scavengers and rodents, and result in a range of diseases through different routes of exposure such as fecal-oral and soil transmitted mechanisms. (WHO, 2005). The main aim of this study is to assess the physicochemical and microbiological quality of top soils collected in the vicinity of these makeshift open waste dumpsites located within public schools across Benin City.

* Corresponding author e-mail: frank.eghomwanre@uniben.edu

2. Materials and Methods

2.1 Study Area

The study area is Benin City in Nigeria. Benin City is a humid tropical urban metropolis which comprises four Local Governmental Areas, namely Egor, Ikpoba Okha, Oredo, and Ovia North East. It is located within latitudes 6°20′N and 6°58′N, and longitudes 5°35′E and 5°41′E (Okhakhu, 2010). It broadly occupies an area of approximately 112.552 km with an estimated population of 1,086,882 people (NPC 2006). The city has over 500 schools made up of both public and private nursery, primary, and secondary educational facilities.

2.2 Sample Collection

Surface soil samples were collected from twelve open dumpsites within twelve public secondary schools sited across Ikpoba Okha, Egor, Oredo Local Government and Ovia North East area of Edo State. The samples were collected between May and July, 2018. About One-hundred grams of the surface soil samples were collected in triplicates at a depth of 2 cm - 20 cm with the aid of a soil auger. The surface debris of the soils was removed before sampling. The samples were dispensed into sterile containers and appropriately labeled. A control soil was obtained from a farmland in the University of Benin, Ugbowo, Benin City.

2.3 Enumeration and Identification of Heterotrophic Soil Microflora

The mean heterotrophic bacterial and fungal count of the soil samples were examined with the aid of serial dilution and pour plate technique as described by Harley and Prescott (2002) and Aneja (2003).

2.4 Characterization of the Soil Microbiota

The subcultured bacterial isolates were subjected to an array of relevant physiological and biochemical tests which included; catalase production, spore staining, coagulase production, sugar fermentation tests Gram staining, and oxidase test. The results were compiled and the tentative identity of the respective bacterial isolates were ascertained by the comparison of the complied results recorded for the respective isolates with descriptive identification schemes as described by Holt et al. (1989) and Cullimore (2000). The subcultured fungal isolates were identified on the basis of their morphological and microscopic features. The cultural attributes of the subcultured fungal cultures were noted, and the microscopic features of the fungal isolates were observed with the aid of the wet mount procedure as described by Sharma (2009). The mountants were stained with lactophenol cotton blue and distilled water was employed respectively as described earlier by Obayagbona and Enabulele (2013). The microscopic structures observed were recorded and compared to illustrations stated by Barnett and Hunter (1972) and Alexopolulos et al. (1996).

2.5 Physicochemical Analyses of the Soil Samples

The following physiochemical properties of the various soil samples were determined. Parameters which included pH, electrical conductivity (EC), and particle-size distribution were ascertained using the procedures described by Kalra and Maynard (1991). The soil samples were analyzed for their Nitrate (NO^-_3), Ammonium ($NH4^+$), and Phosphate (PO_4^{-3}) contents using the methods described by Onyeonwu (2000). The Total Organic Carbon (TOC) content of the respective samples was obtained according to procedure described by Bremmer and Mulvaney (1982) while TOM was determined according to the method described by Osuyi and Adesiyan (2005).

2.6 Statistical Analysis

The statistics package for social sciences (SPSS version 20) was used to generate analysis of variance (ANOVA), and the Duncan's multiple range tests were used to test significance and mean separation respectively at a 95% level of confidence. Pearson correlation was employed in the correlation analysis to examine and establish the association between and physicochemical characteristics and the microbial parameters of the waste dumpsites' samples.

3. Results and Discussion

The mean concentration of the physicochemical analysis of the soil samples collected from the waste dumpsites across public schools in Benin City is presented in Table 1. The degree of acidity or alkalinity of a soil is a very important property which affects many other physicochemical and biological properties. The mean values of pH across the sampled locations ranged from 5.82 ± 1.58 to 6.72 ± 1.17. The pH of the soils from most of the locations were significantly higher than that of the control soil (4.76 ± 0.68) at $p < 0.0.5$. (Table 1) This could be attributed to liming materials and the activities of some microorganism in the solid wastes (Ayade, 2003, Ideriah et al., 2006). The pH of the soils obtained in this study were slightly acidic, and was similar to the readings recorded by both Abdus-Salam (2009) and Ogbonna et al., (2009) who reported 5.4 to 7.7 and 5.6 to 6.0, respectively but are in contrast with the findings of Oguntimehin and Ipinmoroti, (2008); Parth et al. (2011). The moderate acidic pH values obtained in the sites under study could be attributed to the removal of basic cations or nutrients from the surface of the soils in the dumpsites as a result of the effect of anthropogenic activities such as burning which resulted in the loss of nutrients. The EC values in this study ranged from 77.22 ± 6.14 to 259.67 ± 64.34 µS/cm. These findings were lower than those of Osazee et al. (2013) who reported values from 164.00 to 540.00 µS/cm, respectively. The EC values were significantly higher than those of the control site except at Dumpsite 9 (DS9) with EC of 77.22 ± 6.14 µS/cm.

The high EC values in this study showed that the soil samples have a high concentration of soluble salts which is a good indicator of plant growth. The sulphate ranged from 2.26 ± 0.53 to 5.83 ± 1.18 mg/kg. There were significant differences in the sulphate concentration across the site and the control soil except in DS1.This finding is in agreement with an earlier study by Osazee et al. (2013) who showed a range of 2.38 to 3.44 mg/kg. The nitrate and phosphate values varied from 29.11 ± 16.11 to 60.06 ± 10.76 and 13.99 ± 3.22 to 33.57 ± 26.57 mg/kg, respectively. The Nitrate and Phosphate levels were significantly higher in the soils from the different sampled locations compared to the control sites at $P < 0.5$. This finding is consistent with the report of Akinbile and Yusoff (2012); Akinnusotu and Arawande (2016). The presence of nitrate in the soil may be attributed to the mineralization of nitrogen as a result of organic matter in the soil. Whilst the phosphate concentration could

be attributed to the presence of a high amount of organic matter and plant decomposition at the dumpsites (Ideriah et al., 2006). The percentage of TOC and TOM recorded for the respective soils ranged from 1.44 ± 0.72 to 3.83 ± 2.47% and 2.28 ± 0.69 to 6.71 ± 4.05%. These percentages were higher than those of Abdus-Salam et al. (2011) who reported 0.028-0.409 and 0.048-0.707%. The carbon content and organic matter in the various dumpsite soils were significantly higher than those of the control soil samples which were 0.60 ± 0.31 and 1.16 ± 0.97%, respectively. The higher percentage of the concentration of organic matter in the examined soils could be attributed to the presence of organic waste residues which add more organic matter when decomposed. Munoz et al. (1994) also reported that the elevated amount of organic carbon in various soil samples in the vicinity of dumpsites could be suggestive of possible degradation or the presence of degradable and compostable wastes. Biyogue (2016) reported a positive correlation between organic carbon, organic matter, and the available phosphorous across forest soils which means that the high organic matter content increased the availability of soil phosphorous concentrations. This is, however, consistent with the findings of this study. Omar (2015) stated that the soil texture is known to play a critical role in the improvement of the cation exchange capacity (CEC) of the soil and therefore its capacity to hold major and minor nutrients. The percentage proportion of clay, silt, and sand in the soils from waste dumpsite are presented in Table 1. The soil samples from the various sampling points were silty, and this is in agreement with a report by Ogbonna et al. (2009) who observed that top soil samples collected from most waste dumpsites in Port Harcourt, Rivers State, Nigeria were silty in nature. However, this trend is inconsistent with the reports of Eneje and Lemoha (2013), Oyedele et al. (2008) and Ideriah et al., (2010), who observed that the top soils sourced from several municipal dumpsites in Owerri, Eastern Nigeria were sandy. The role of the soil forming materials in determining the textural class of a particular soil could be the reason for the differences in soil texture (Oyedele et al., 2008).

Table 1. Mean concentrations of physicochemical properties of open dumpsites

Locations	pH	EC	SO^-_4	NO^-_3	PO^+_4	NH^+_4	TOC	TOM	Clay	Silt	Sand
		(µS/cm)	(mg/kg)	(mg/kg)	(mg/kg)	(mg/kg)	(%)	(%)	(%)	(%)	(%)
DS1	6.21 ± 1.04b	116.22 ± 4.49ab	5.83 ± 1.18d	31.68 ± 16.69ab	13.99 ± 3.22ab	6.42 ± 0.46a	2.84 ± 0.68cde	4.53 ± 1.04cd	8.36 ± 0.51a	24.29 ± 0.78bcd	6.62 ±0.81cd
DS2	6.64 ± 1.20b	137.44 ± 11.16b	3.11 ± 0.57bc	41.26 ± 14.20ab	17.24 ± 5.44ab	10.13 ± 3.41ab	3.19 ± 1.25de	4.31 ± 1.37cd	6.96 ± 1.43a	16.11 ± 0.46abc	3.56 ±0.95ab
DS3	5.91 ± 1.84ab	134.89 ± 2.80b	1.93 ± 0.66a	30.86 ± 22.34ab	33.57 ± 26.57b	8.51 ± 6.01ab	2.20 ± 0.47bdc	3.69 ± 0.46bcd	4.66 ± 0.41a	17.89 ± 1.30abc	3.04 ± 0.55a
DS4	5.96 ± 1.43ab	137.33 ± 38.30b	3.50 ± 0.60c	43.44 ± 16.36abc	14.30 ± 1.12ab	10.97 ± 4.46ab	3.09 ± 1.43de	4.36 ± 1.89cd	9.11 ± 0.51a	20.37 ± 3.02abc	8.14 ± 0.59f
DS5	5.82 ± 1.58ab	185.89 ± 4.94c	3.39 ± 1.10c	45.52 ± 5.99bc	32.07 ± 22.81b	12.23 ± 4.77ab	3.22 ± 1.88de	5.52 ± 3.16de	7.20 ± 0.55a	14.80 ± 0.60ab	7.71 ± 1.10ef
DS6	6.28 ± 0.93b	95.22 ± 4.24ab	4.46 ± 0.65c	35.02 ± 19.54ab	33.38 ± 37.02b	8.16 ± 5.45ab	1.76 ± 0.84abc	3.10 ± 1.43bc	8.84 ± 0.62a	22.17 ± 0.50abcd	6.38 ± 0.61c
DS7	6.70 ± 1.31b	259.67 ± 64.34d	4.27 ± 0.67c	60.06 ± 10.76c	33.46 ± 16.27b	13.91 ± 2.43b	3.83 ± 2.47e	6.71 ± 4.05e	10.92 ± 23.66a	30.92 ± 32.85d	7.24 ± 0.39de
DS8	6.11 ± 1.12b	120.00 ± 6.95ab	2.30 ± 0.78a	37.40 ± 17.62ab	32.43 ± 32.63b	10.53 ± 7.82ab	2.59 ± 1.06bcde	3.87 ± 1.16bcd	8.45 ± 0.58a	13.72 ± 1.08a	6.64 ± 0.25cd
DS9	6.47 ± 1.49b	77.22 ± 6.14a	2.26 ± 0.53a	24.39 ± 13.69a	18.80 ± 18.48ab	8.54 ± 6.36ab	1.63 ± 0.85abc	2.28 ± 0.69ab	4.34 ± 0.22a	16.87 ± 1.21abc	4.00 ± 0.48b
DS10	6.72 ± 1.17b	131.89 ± 2.37b	2.61 ± 0.55ab	29.11 ± 16.11ab	28.86 ± 32.59ab	6.90 ± 3.53a	2.16 ± 0.88bcd	3.03 ± 0.49bc	6.58 ± 1.23a	16.21 ± 1.89abc	6.44 ± 0.20c
DS11	6.60 ± 1.44^{b}	136.00 ± 9.34^{b}	2.28 ± 0.55^{a}	31.62 ± 22.40^{ab}	18.98 ± 17.30^{ab}	7.07 ± 4.99^{a}	1.44 ± 0.72^{ab}	2.66 ± 1.12^{abc}	9.39 ± 1.34^{a}	20.62 ± 0.96^{abc}	9.07 ± 0.90^{g}
DS12	6.49 ± 1.26b	90.33 ± 14.32ab	4.28 ± 0.50c	40.39 ± 24.90ab	17.78 ± 13.88ab	9.14 ± 6.10ab	2.01 ± 0.98bcd	3.19 ± 1.61bc	7.68 ± 0.16a	16.93 ± 0.58abc	6.40 ± 0.70c
Control	**4.76 ± 0.68a**	**74.78 ± 147.53a**	**5.56 ± 0.48d**	**23.64 ± 24.26a**	**7.96 ± 6.65a**	**7.92 ± 9.13ab**	**0.60 ± 0.31a**	**1.16 ± 0.97a**	**9.80 ± 0.76a**	**25.17 ± 2.54cd**	**6.92 ± 0.42cd**

Values are Mean ± SD of three replicates. Different superscripts in the same column indicate significant differences at $p < 0.05$ according to Duncan Multiple Range Test (DMRT). EC= electrical conductivity, EC electrical conductivity, SO^-_4 sulphate, NO^-_3: nitrate; PO^+_4 Phosphate, NH^+_4 Ammonium, TOC total organic content, TOM total organic matter, DS= Dumpsites.

The results of the microbial count in waste dump on soils are shown in Table 2.

Table 2. Total Bacterial and Fungal counts of the surface soil samples from the dumpsites

Location	THBC (×10⁴cfu/g)	THFC (×10³cfu/g)
DS1	2.81 ± 1.01a	3.38 ± 0.86abc
DS2	3.22 ± 1.52ab	5.39 ± 1.27de
DS3	6.38 ± 1.78g	4.14 ± 2.88bcd
DS4	5.22 ± 0.63defg	3.07 ± 1.18ab
DS5	3.33 ± 0.99ab	4.03 ± 0.86cd
DS6	3.93 ± 1.87abcd	3.22 ± 1.42abc
DS7	2.67 ± 1.34a	4.61 ± 2.20cd
DS8	5.64 ± 0.65efg	3.02 ± 1.63ab
DS9	5.96 ± 0.72fg	3.39 ± 1.08ab
DS10	4.74 ± 2.41cdef	2.00 ± 0.73a
DS11	4.50 ± 0.69bcde	3.80 ± 0.94bc
DS12	3.86 ± 0.58abc	3.97 ± 0.65bcd
Control	**2.71 ± 0.61a**	**3.03 ± 0.46ab**

Values are Mean ± SD of three replicates. Different superscripts in the same column indicates significant differences at p < 0.05 according to Duncan Multiple Range Test (DMRT). THBC and THFC Total Bacterial and Fungal counts, respectively.

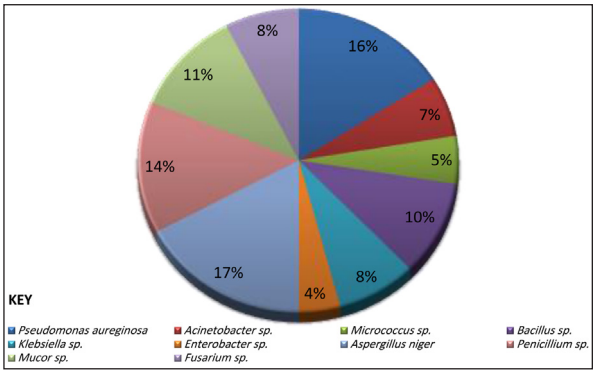

Figure 1. Percentage frequency of occurrence of the microbial isolates

The mean heterotrophic bacterial counts ranged from 2.81 ± 1.01 to 6.38 ± 1.78 (×10⁴cfu/g), while the THFC ranged from 2.00 ± 0.73 to 7.03 ± 0.86 (×10³cfu/g). The bacterial counts in soils from the dumpsites were significantly higher than those of the control soil ($P < 0.05$) except at sites DS1 and DS7. This trend is supported by the higher organic carbon and nitrogen content of the dumpsite soils in comparison to the control soil (Table 2). This phenomenon might be the result of the increased availability of biodegradable organic and inorganic substrates from the variety of municipal wastes being continuously dumped at these sites. There was no significant difference between the total heterotrophic fungal count of the dumpsite soils and the control soil samples.

The isolation of Acinetobacter sp., Pseudomonas sp., Micrococcus sp. Bacillus sp., Klebsiella sp., Enterobacter sp. Aspergillus sp., Penicillium sp., Mucor sp. and Fusarium sp. was similar to a report by Osazee et al. (2013) who isolated similar microorganisms from a municipal waste dumpsite in Benin City. All the microbial isolates identified from the soil samples have been reported to be associated with wastes and waste biodegradation (Obire et al. 2002).

The frequency of the bacterial isolates from the waste dumpsite soils were: Acinetobacter sp. (7.00%) Pseudomonas aeruginosa (16.00%), Micrococcus sp. (5.00%), Bacillus sp. (10.00%) Klebsiella sp. (8.00%) and Enterobacter sp. (4.00%), while those of fungi were Aspergillus niger (17.00%), Penicillium sp. (14.00%), Mucor sp. (11.00%) and Fusarium sp. (8.00%) (Figure 1). The bacterial cultures isolated in this study, with the exception of Arthrobacter, are known to occur more commonly in the air and soil environments, and have been described as opportunistic human pathogens (Cheesebrough, 2006). Pavoni et al. (1975) reported that truly pathogenic forms of fungi may survive in waste. The open dumping of garbage around the schools could also function as a breeding ground for disease vectors such as flies, mosquitoes, cockroaches, rats, and other pests. These dumpsites could pose public health risks to the students, teachers, and populations living around the school premises whose food and water supplies may, perhaps, become contaminated as a result of either waste dumping or leakage from dumpsites during rains. This could lead to an increased risk of the spread of infectious diseases such as food and waterborne diseases (Aboagye-Larbi et al., 2004).

Table 4. Correlation between physicochemical and microbiological parameters of the top soil samples at the dumpsites

	pH	EC (µS/cm)	SO^-_4 (mg/kg)	NO^-_3 (mg/kg)	PO^+_4 (mg/kg)	NH^+_4 (mg/kg)	TOC (%)	TOM (%)	Clay (%)	Silt (%)	Sand (%)
THBC (×10⁴cfu/g)	-0.064	-0.354**	-0.466**	-0.241**	0.170	-0.140	-0.059	-0.144	-0.036	-0.126	-0.162
THFC (×10³cfu/g)	0.234*	0.163	-0.321**	0.265**	0.153	0.307**	0.026	0.005	0.056	-0.081	-0.174

***. Correlation is significant at the 0.01 level (2-tailed). *. Correlation is significant at the 0.05 level (2-tailed).*

Table 4 revealed that EC, SO^-_4, NO^-_3 correlated negatively but weakly with the total bacterial count ($r = -0.354$), ($r = -0.466$) and ($r = -0.241$), respectively at a $p < 0.01$ significant level. This inverse relationship may be attributed to the high level of EC, sulphate, and nitrates which may become toxic to the bacterial populations. pH correlated positively but weakly with the total fungal count ($r = 0.234$; at $p < 0.05$). The weak positive association could be attributed to the moderate acidic pH level of the soil due to human activities such as burning. Nitrate and ammonium correlated positively with THFC ($r = 0.265$), ($r = 0.307$) at $p < 0.01$. Tangjang et al., (2009) reported that the higher soil fungal counts were due to the greater availability of nitrate and ammonium nutrients which could be a result of the increased accumulation of biodegradable wastes at the dumpsites.

4. Conclusions

The current study reveals a significant difference in most of the physicochemical parameters of the soils in the vicinity of the waste dumpsites and the control sites. This is an indication of the improvement of the soil quality by the waste, which is being dumped constantly at the sites within the school vicinities. However, this study also shows the presence of a high microbial load which could be linked to the increased nitrate, phosphate, organic carbon, and organic matter levels reported in the examined dumpsite soils. The provision of adequate waste collection facilities and the mainstreaming of hygiene education and sanitation into the schools' systems can improve the collection and management of municipal solid waste (MSW).

References

Aneja, K.R. (2003). Experiments in Microbiology, Plant Pathology and Biotechnology. 4thEdn.New Age Pub. Ltd. New Delhi P. 606.

Abdus-Salam N. (2009). Assessment of heavy metal pollution in dump sites in Ilorin metropolis. Ethiopian Journal of Environmental Studies and Management 2(2): 92-99.

Abdus-Salam, N., Ibrahim, M.S., Fatoyinbo, F.T. (2011). Dumpsites in Lokoja, Nigeria: A silent pollution zone for underground water. Waste Management and. Bioresource Technology Journal 1:21-30.

Aboagye-Larbi, H., Acheampong, M.A., Sampson, K.K (2014). The potential health hazards associated with waste scavenging in Ghana: A case study of three selected dumpsites in Tema metropolis. International Journal of Environmental Science and Toxicology Research 2(10):199-209.

Akinbile, C.O. and Yusoff, M.S. (2012). Solid waste generation and decomposition using compost bin technique in Pulau Pinang, Malaysia, Waste Management and Research 3(5): 498-505.

Akinnusotu, A. and Arawande, J. O. (2016). Physicochemical Characteristics and Heavy Metals Concentration in Sub Surface Soil at Different Dumpsites in Rufus Giwa Polytechnic, Owo, Ondo State, Nigeria. Journal of Environmental and Agricultural Sciences 8:21-28.

Alexopoulos, C.J., Mims, C.W., Blackwell, M. (1996). Introductory Mycology. Fourth Edition. John Wiley and Sons Inc., New York.

Ayade, B.B. (2003). Indigenous biological treatment of hydrocarbon contaminated soil in the tropics. Journal of Nigerian Environmental Society 1(1): 87-94.

Barnett, H.L. and Hunter, B.B. (1972). Illustrated Genera of Imperfect Fungi. Third edition. New York: Burgess. P. 225.

Biyogue, D.N. (2016). Impacts of anthropogenic activities on physical and selected chemical properties of soils in the natural forest savanna of Northern Ghana. Journal of Soil Science and Environmental Management 7(5): 53-63.

Bremmer, I.M.and Mulvaney, C.S. (1982). Total Nitrogen. In: American Society of Agronomy and Soil Science (Eds.). Methods of soil analysis. Agronomy Monograph 9. Madison: American Society of Agronomy and Soil Science P. 595-627.

Cheesebrough, M. (2006). District Laboratory Practice in Tropical Countries. Cambridge University Press, Cambridge P.434.

Christensen, D., Drysdale, D., Hansen, K., Vanhille, J., Wolf, A. (2014). Partnerships for development: Municipal solid waste management in Kasese, Uganda. Waste Management and Research 32(11): 1063-1072.

Cullimore, D.R. (2000). Practical Atlas for Bacterial Identification. CRC Press P. 209.

Eneje, R.C. and Lemoha, K.T. (2012). Heavy metal content and physicochemical properties of municipal solid waste dump soils in Owerri, Imo State. International Journal of Modern Engineering Research 2(5): 3795-3799.

Harley, J.P.and Prescott, L.M. (2002). Laboratory Exercises in Microbiology. Fifth edition. New York: Mac Graw Hill. 449 p.

Holt, J.G., Krieg, N.R., Sneath, P.H.A. (1989). Bergey's Manual of Determinative Bacteriology 4. London: Cambridge University Press P. 2493.

Ideriah, T. J. K., Omuaru, V. O. T, Adiukwu, P. U. (2006). Soil quality around a solid waste dumpsite in Port Harcourt. African Journal of Ecology, 44(3):388-394.

Kalra Y.P. and Maynard, D.G. (1991). Methods Manual for Forest soil and Plant Analysis. Edmonton, Canada: Minster of supply and services. 125 pp.

Munoz M., Pena L, Halloroms J.O. (1994). Use of an industrial by- product as a liming source. Journal of Agriculture of the University of Puerto Rilo 78(3-4): 73-86.

National Population Census. (2006). Population Census Reports. Benin City: NPC Headquarters.

Obayagbona, O.N., and Enabulele, O.I. (2013). Biodegradation potentials of mycoflora isolated from auto mobile workshop soils on flow station crude oil sludge with an extra carbon source. Journal of Microbiology, Biotechnology and Food Sciences, 3(1): 19-25.

Obire, O., Nwabueta O., Adue S.B.N. (2002). Microbial community of a waste dump site. Journal of Applied Science and Environmental Management, 6(1): 78-83.

Ogbonna D.N., Kii, B.C., Youdeowei, P.O. (2009). Some physicochemical and heavy metal levels in soils of waste dump sites in Port Harcourt municipality and environs. Journal of Applied Science and Environmental Management 13(14): 65-70.

Oguntimehin, I.O. and Ipinmoroti, E.K. (2008). Profile of heavy metals from Automobile workshops in Akure, Nigeria. J. Environ. Sci. Tech. 1: 19-26.

Okhakhu, P.A. (2010). The significance of climatic elements in planning the urban environment of Benin City, Nigeria. Unpublished PhD thesis. Ekpoma-Nigeria: Department of Geography and Regional Planning, Ambrose Alli University P. 47.

Omar, A.A. (2015). Determination of macro and micronutrients levels in organic manure soils and irrigation water. Journal of Natural Sciences Resource 3(2): 41-49.

Onyeonwu R.O. (2000). Manual for Waste/Wastewater, Soil/ Sediment, Plant and Fish analysis. Benin City: MacGill Environmental Research Laboratory Manual. P. 81.

Osazee, O.J., Obayagbona, O.N., Daniel, E.O. (2013). Microbiological and physicochemical analyses of top soils obtained from four municipal waste dumpsites in Benin City, Nigeria. International Journal of Microbiology and Mycology 1(1): 23-30.

Osuyi, L.C. and Adesiyan, S.O. 2005. The Isiokpo oil pipeline leakage. Total organic carbon/organic matter contents of affected soils. Chemistry and Biodiversity 2:1097-1085.

Oyedele, D.J., Gasu, M.B., Awotoye, O.O. (2008). Changes in soil properties and plant uptake of heavy metals on selected municipal solid waste dump sites in Ile-Ife, Nigeria. African Journal of Environmental Science and Technology 3(5): 107-115.

Partha, V., Murthya, N., Saxena, P. R. (2011). Assessment of heavy metal contamination in soil around hazardous waste disposal sites in Hyderabad city (India): natural and anthropogenic implications. E3 Journal of Environmental

Research and Management 2(2): 027-034

Pavoni, J.L., Heer, Jr. J.E., Hagerty, D.L. (1975). Handbook of solid waste disposal, materials and energy recovery. New York: Van Nostrand Reinhold Company.

Sharma, P. (2009). Manual of Microbiology, tools and techniques. New Delhi: Ane books. Pvt. Ltd. P. 405.

Sridhar, M.K.C. (1998). Wastes-Their nature and impact on environment. Paper presented at a training workshop on planning and management of waste systems and environmental care, Ibadan, Nigeria. November, pp. 18-19.

Tangjang, S., Arunachalam, K., Arunachalam, A., Shukla, A.K. (2009). Research microbial population dynamics of soil under traditional agroforestry systems in Northeast. India Journal of Soil Biology 1(1): 1-7.

Verge, A., and Rowe, R.K. (2013). A framework for a decision support system for municipal solid waste landfill design. Waste management and Research 31(12): 1217-1227.

Wahab, B. (2003). Towards an effective waste management system in primary schools. Paper presented at a three-day training workshop for public primary school teachers and supervisors on waste disposal, composting, horticulture and school/home gardening, organized and sponsored by the sustainable Ibadan project (ISP) in collaboration with UNICEF B Zone. Ibadan, Nigeria

World Health Organization (2005). The World Health Report 2002: reducing risks, promoting healthy life. Geneva, World Health Organization.

المملكة الأردنية الهاشمية

صندوق دعم البحث العلمي

الجامعة الهاشمية

المجلة الأردنية
لعلوم الأرض والبيئة

JJEES

مجلة علمية عالمية محكمة

المجلد (١١) العدد (١)

http:// jjees.hu.edu.jo/

ISSN 1995-6681

المجلة الأردنية لعلوم الأرض والبيئة

مجلة علمية عالمية محكمة

المجلة الأردنية لعلوم الأرض والبيئة: مجلة علمية عالمية محكمة ومفهرسة ومصنفة، تصدر عن عمادة البحث العلمي في الجامعة الهاشمية وبدعم من صندوق البحث العلمي - وزارة التعليم العالي والبحث العلمي، الأردن.

ترسل البحوث إلكترونيا إلى البريد الإلكتروني التالي:

رئيس تحرير المجلة الأردنية لعلوم الأرض والبيئة

jjees@hu.edu.jo

لمزيد من المعلومات والأعداد السابقة يرجى زيارة موقع المجلة على شبكة الانترنت على الرابط التالي:

www.jjees.hu.edu.jo

المملكة الأردنية الهاشمية صندوق دعم البحث العلمي الجامعة الهاشمية

JJEES

المجلة الأردنية لعلوم الأرض والبيئة

المجلد (١١) العدد (١)

مجلة علمية عالمية محكمة تصدر بدعم من صندوق دعم البحث العلمي

ISSN 1995-6681 jjees.hu.edu.jo آذار ٢٠٢٠